Colloidal suspensions under external control

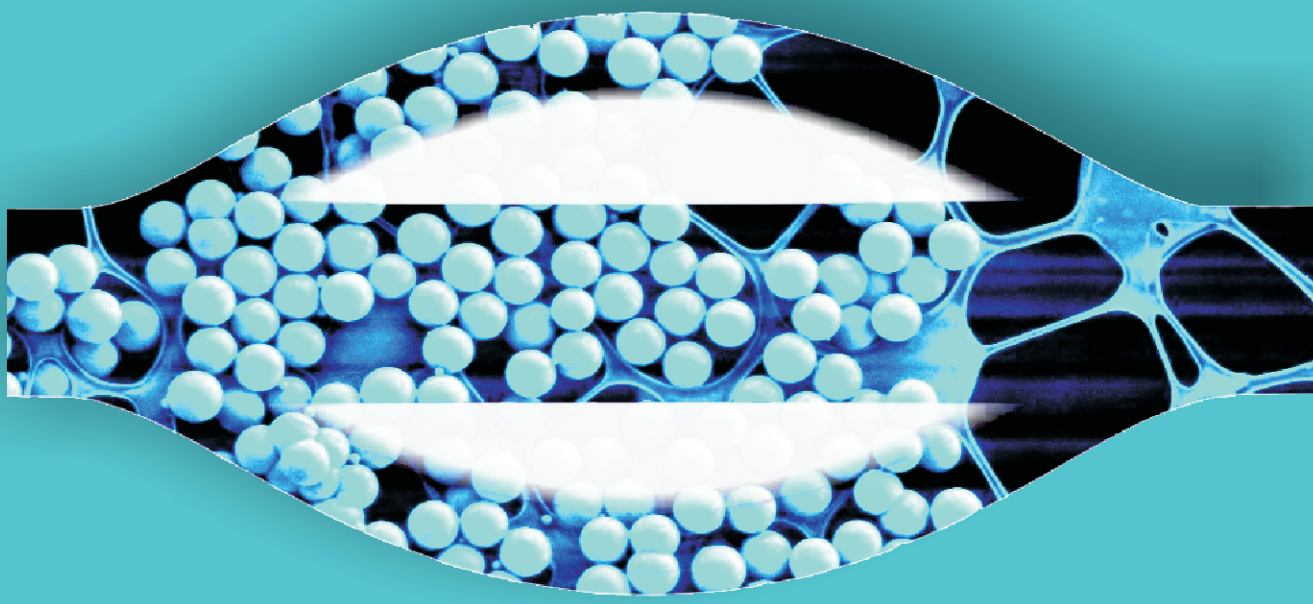

H.BURAK ERAL

COLLOIDAL SUSPENSIONS UNDER EXTERNAL CONTROL

The work described in this thesis has been carried out in the group of Physics of Complex Fluids at University of Twente. The work described in the thesis is supported by Chemical Sciences division of the Netherlands Organization for Scientific Research (NWO-CW) for financial support (ECHO grant). Physics of Complex Fluids group is a part of the research program of the Institute for Mechanics, Processes and Control (IMPACT), MESA+ and the J.M. Burgerscentrum.

ISBN: 978-90-365-3167-2

Printing: Gildeprint Drukkerijen, Enschede

COLLOIDAL SUSPENSIONS

UNDER EXTERNAL CONTROL

PROEFSCHRIFT

ter verkrijging van

de graad van doctor aan de Universiteit Twente,

op gezag van de rector magnificus,

prof. dr. H. Brinksma

volgens het besluit van het College voor Promoties

in het openbaar te verdedigen

op Vrijdag 4 maart 2011 om 12.45 uur

door

HÜSEYİN BURAK ERAL

geboren op 07 april 1980

İZMİR, TÜRKİYE

Dit proefschrift is goedgekeurd
door de promotor

prof. dr. F. Mugele

en de assistent-promotor

dr. M.H.G. Duits

Contents

1 Introduction

Abstract In this introductory chapter, colloidal suspensions are described not only in terms of their importance as model systems in revealing the principles of equilibrium many-body transitions but also as building blocks in the engineering of complex materials and material science. Colloidal suspensions consist of mesoscopic particles called colloids with typical sizes ranging from 1 nm to 10 μm embedded in a liquid. Colloids play a crucial role in unraveling the underlying physics at molecular level as model atoms not only for systems that are in equilibrium and in static non-equilibrium but also systems brought out of equilibrium with external control. In this chapter, an outline of experimental work on confinement effects and flow fields on colloidal suspensions is presented while placing it in broader context and making connections to the engineering of complex materials. A more specific background and introduction is given in each separate chapter.

1.1 General Background

It is hard to ignore colloids as we are surrounded by them in our daily routines, starting from the very essence of life. Our blood, the pool of all physiological activities is a colloidal suspension made of various cells dispersed in water rich in salt, proteins and globular constructs. The paint that protects our house, the milk we drink, the toothpaste we the pour on our toothbrush, the butter and mayonnaise we spread on our bread are made of nothing but colloids.

Apparently colloids surround us in daily life and beyond. Colloidal systems appear in various sizes and constitutions obviously but what properties exactly defines a colloid? When is a system colloidal? Beyond doubt the first common feature that comes to mind is the existence of a small constituent of one substance dispersed in another. The dispersed substance is called the dispersed phase and surrounding medium is called the continuous phase. Both continuous phase and dispersed phase can be gas-,liquid- or solid like. There is a vast spectrum of colloidal systems that include aerosols (liquid droplets or solid particles in gas), emulsions (liquid droplets in liquid) , foams (gas bubbles in a liquid) and suspensions (solid particle in a liquid). Throughout this thesis only suspensions with solid particles suspended in liquid are considered.

As described above, a colloid can be almost in any shape and phase imaginable yet there are limitations on the size of colloidal particles forming the system. Colloidal systems should exhibit Brownian motion in other words the energy of a colloidal particle has to be bigger than the gravitational energy. This criterion dictates the size of systems which we call colloidal. Practically particles in the size range 10 nm to 10 micrometer are called colloidal.

The word colloid was introduced by Thomas Graham (1805-1869). In his experiments he observed particles that can be distinguished from molecules by their slow diffusion and inability to penetrate through membranes with pore sizes smaller then 10 nm [1]. Nowadays; colloids are classified under the *Soft Condensed Matter* or *Complex Fluids* along with foams, gels, liquid crystals and polymers. *Soft Condensed Matter* defines a broad class of materials including but not limited to colloidal suspensions, liquid crystals, polymers that are

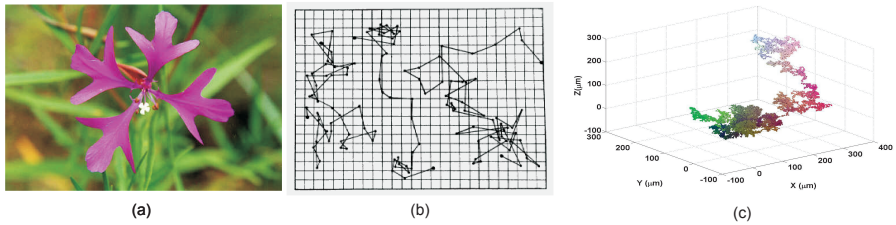

Figure 1.1: Panel (a) provides an image of the Clarkia Pulchella flower used in early experiments of R.Brown. Panel (b) shows the original recordings of Brownian motion used in Perrin's studies. Panel (c) shows the simulated Brownian motion of of one μm particle in water over 10s

characterized by weak interactions between polyatomic constituents, by important thermal fluctuations effects, by mechanical softness and rich phase behavior. The nomenclature acquired its popularity when Pierre-Gilles de Gennes chose it as the title of his 1991 Nobel lecture.

Brownian motion is perhaps the most important property of colloidal suspensions as it maintains the particles in dispersed state, fighting against gravity that pulls particles towards earth and attractive interactions that tend to bring particles together. Furthermore, it modifies the macroscopic flow properties of colloidal systems, the materials response to stress and its ability of the system to probe the different configurations hence self assemble to minimum free energy configurations. The response of suspensions to applied stress are dramatically altered by Brownian motion. A dilute suspension behaves like a viscous liquid and flows upon application of shear. The energy injected to the suspension can be easily dissipated if the system can exhibit Brownian motion. If the particles are arrested i.e.Brownian motion is hindered such as in gels or glassy systems only a fraction of the energy can be dissipated immediately leading to viscoelastic behavior.

1.2 Brownian Motion

Our understanding of colloidal suspensions and soft matter originates from the discovery of Brownian motion. The Brownian motion (i.e. thermal fluctuations) are most observable at the scale of colloidal suspensions is the reason why colloids provided the original key to the establishment of statistical thermodynamics. Furthermore it is the underlying reason *Soft Matter* studies today are so important in modern mesotechnologies, such as engineering/material science of complex materials including high-precision filters, controlled-porosity substrates, and photonic devices and more common materials such as foods, cosmetics, detergents, even extending into biomaterials in biophysics. In this section, we briefly discuss how the discovery of Brownian motion lead to our current understanding of *Soft Matter* under four chronological periods: discovery of Brownian motion, theoretical indications, quantitative confirmation of Brownian motion and eventually to our current understanding of *Soft Matter*.

1.2.1 Discovery and Confirmation of Brownian Motion

Brownian motion is a defining property of colloids and soft matter. It was first discovered in 1827 by Scottish botanist Robert Brown (1773-1858). During his studies of plant life and their reproduction [2], Brown first observed the phenomenon while working with plant seed of micron size. He tracked the path of cytoplasmic pollen particles on their way to the reproduction organ of the Clarkia Pulchella, a species native to Pacific Northern Western America (Fig. 1.1). He used these pollen granules because they contain oblong particles, which he observed were 6 to 8 μm in length. He was intrigued by the motion of pollen particles as he mentions in his article in the following direct quote " These motions were such as to satisfy me, after frequently repeated observations,that they arose neither from currents in fluid, nor from its gradual evaporation, but belonged to the particle itself ". This observation was the milestone for the systematic investigation of the thermal noise phenomena or in more common terms the Brownian motion.

In reality Brown was not the first to observe the random motion of colloidal particles. Many other naturalists such as W.F.Gleichen, J.T.Needham, G-L.Leclerc, A-T.Brogniart, and L.Spallanzani had observed Brownian motion but their ability for correct interpretation of the observations were clouded by the ongoing debate on vitalism and spontaneous generation [3]. R.Brown is credited with the first observation of the phenomena as his findings were the first systematic experimental analysis convincingly demonstrating that the motion was not due to thermal flows, bubbles, release of material or interaction between particles. It is important to note that J.Ingen-Housz in 1784 and J.Bywater in 1819 independently concluded that the motion exists for inorganic particles prior to Brown's observations. Brown's first conclusion was also inspired by spontaneous generation but he patiently repeated the experiments first with other plants, and later with small particles prepared by grinding various plant parts such as root, ovula and leaves. An astonishing development occurred when Brown repeated the experiments with particles made of dead plants and fossilized wood acquired from a museum. Later, Brown extended his experiments systematically with all kinds of organic and inorganic material extracted from animals and plants furthermore he pulverized various minerals and rocks that he could find. Relying on his experiments he concluded that when the particles are sufficiently small ($\cong$ 1 μm) they will spontaneously move in fluid. It is noteworthy to mention that Brown supported his initial findings with a follow up paper where he designed experiments to silence the critics of the initial experiments [4].

After years of discussion where several critics attributed the Brownian motion to air currents, magnetism, mechanical vibrations , temperature differences and particle interactions. In late 1880s Leon Gouy designed a set of experiments to establish a solid basis of Brown's observations, from which scientists could begin to consider the fundamental implications of Brownian motion. In a series of comprehensive experiments [5, 6, 7], Gouy demonstrated convincingly that the irregular motion of suspended particles was not a result of aforementioned effects in other words that Brownian motion is indeed a fundamental physical property of fluid matter. Furthermore, he verified qualitative trends, such as the decreasing amplitude

of the observed motion with increasing particle size and increasing solvent viscosity. Gouy interpreted these results in the context of kinetic theory of gases introduced by James Clerk Maxwell and Ludwig Boltzmann to explain the properties of gas as the macroscopic implications of thermal motion of gas molecules. According to kinetic theory, temperature is a measure of mean kinetic energy of molecules in other words the heat we sense in summer months is nothing but the increased mean velocity of surrounding molecules.

Perhaps most importantly, Gouy also pointed out [6] the significance of Brownian motion in thermodynamics. Gouy proposed a thought experiment in which a 'paddle' attached to a tiny thread would be driven back and forth continually due to the impacts of suspended Brownian particles. When the Brownian particles impact the paddle the thread will move which in return can be used to drive a wheel. The perpetual motion would contradict the second law of thermodynamics. Actually what Gouy pointed out was nothing but the thermodynamic limit as pointed out by Clausius, Boltzmann and Maxwell in kinetic theory. In other words, Gouy was proposing that the second law could not be considered absolute at microscopic scales and thermodynamics required a statistical interpretation in which its absolute character only became visible in what we would now call the 'thermodynamic limit' of large numbers.

With experimental observations of Brown, Gouy and many others the following main points emerged certain [8, 9].

1. The motion of colloidal particle is composed of translations and rotations with a very irregular nature.

2. The motion of two particles are independent provided that the distance between two particles is greater than a diameter.

3. The motion of particles is more violent for smaller particles.

4. The material the particle is made of, composition and density of the particles have no effect.

5. The motion is more violent with less viscous fluids.

6. The motion gets more violent with increasing fluid temperature.

7. The motion never ceases.

The Brownian motion of microscopic particles could be explained by the bombardment of the molecules of the fluid in the context of kinetic theory. Yet, the kinetic theory was still not confirmed with experiments. The application of kinetic theory to Brownian motion provided a simple test: the law of equipartition of energy in statistical mechanics implied that the kinetic energy of translation of a colloidal particle and of a molecule should be equal. In other words, the key to proving kinetic theory hence the existence of atoms could be reached by measuring the mass and the mean velocity of colloidal particles($< V >$) to prove the equality $3/2kT = 1/2m < V^2 >$ where k is the Boltzmann constant, T is the temperature ,m is the mass of colloidal particle. The Boltzmann constant ($k = \frac{R}{N_{av}}$) hence the Avogadro number (N_{av}) can be calculated by experimentally measuring the $< V >$. As easy as it sounds, Measuring $< V >$ has been proven rather difficult experimentally. At this time, experimentalists started looking for easily measurable quantities supported by solid theoretical understanding.

In the period following the discovery and confirmation of Brownian motion, the scientist and the philosophers were divided into two groups: supporters of the continuous description and discontinuous description. Supporters of discontinuous description believed that Brownian motion was essential in proving the discontinuous nature of the matter but at early stages the lack of theoretical description rendered the identification of critical measurable parameters of the experiment difficult.

Einstein was interested in proving the existence of atoms since his early days in science. He formulated a theory describing the Brownian motion on theoretical grounds unaware of the existence of the phenomenon [8]. Einstein's argument was two fold. First part of argument is as follows, Let $\rho = \rho(x,t)$ be the probability density that a Brownian particle is at x at time t. Then, making certain probabilistic assumptions Einstein derived the diffusion equation.

$$\frac{\partial \rho}{\partial t} = D\Delta\rho \tag{1.1}$$

where D is a positive constant, called the coeffcient of diffusion. If the particle is at position 0 at time 0 so that $\rho(x,0) = \delta(x)$ then

$$\rho(x,t) = \frac{1}{(4\pi Dt)^{\frac{3}{2}}} e^{-\frac{|x|}{4Dt}} \tag{1.2}$$

where $|x|$ is the Euclidean distance of x from the origin.

In the second part of the argument Einstein connected the D to other physical measurable quantities [10, 11]. Einstein considered a colloidal particle in dynamic equilibrium where on the one hand the colloidal osmotic pressure balances the applied force (K) on the particle (Eq. 1.3). In Eq. 1.3, the number of particles per volume is given by υ. Assuming K as the graviational force on the particle and integrating Eq. 1.3 Einstein obtained the sedimentation equilibrium connecting the number of particles at a given height.

$$K = kT\frac{\Delta\upsilon}{\upsilon} \tag{1.3}$$

On the other hand, a flux balance is required to explain the phenomena. The Stokesian particle flux produced by the gravitational force is canceled by a diffusive flux of particles. Considering that the Brownian particles moving in the fluid experience a resistance due to friction, the force (K) imparts to each particle a velocity of the form $\frac{K}{m\beta}$ where β is a constant with the dimension of frequency (inverse time) and m is the mass of the particle. Therefore, the particles pass a unit area per unit of time due to the action of the force K is given by $\frac{\upsilon K}{m\beta}$. This Stokian flux is balanced flux induced by random fluctuations i.e. $\frac{\upsilon K}{m\beta} = D\Delta\upsilon$.

Einstein thus obtained an expression for the 'diffusion coefficient' assuming a Stokesian form [11] for the particle velocities imposed by the gravitational force(Eq. 1.4) containing Avogadro's number (N_{av}), molar gas constant (R), the absolute temperature (T), the particle radius(a), and the solvent viscosity (η).

$$D = \frac{RT}{6N_{av}\pi a\eta} \tag{1.4}$$

To predict the time dependence of Brownian motion, Einstein

turned to a probabilistic consideration of the diffusive motion, in particular to obtain the mean squared displacement of a particle(Eq. 1.5).

$$< r^2 >= 6Dt \tag{1.5}$$

Furthermore, assuming a gravitational force i.e.$(K = mg)$ and integrating Eq. 1.3, Einstein obtained the sedimentation equilibrium relation (Eq. 1.6) connecting the number of particles at a given height (N) to thermal energy (kT). In Eq. 1.6, the number of particles (N) at height h above a reference height h_0 is given by Eq. 1.6 where N_0 is the number of particles at height h_0 and $\breve{m}$ is the mass of the fluid displaced by a particle of mass m.

$$N = N_0 e^{\frac{(-m-\breve{m})g(h-h_0)}{kT}} \tag{1.6}$$

The theoretical derivation of mean square displacement and sedimentation equilibrium was a key step to prove the discontinuous nature of matter. As mentioned before, attempts to measure velocities of Brownian particles in experiments had failed due to the nonlinearity of displacement with time. Einstein's now-familiar expressions provided measurable quantities that can be directly compared to theory.

Due the popularity of Einstein's other contributions William Sutherland's independent derivation of the same quantities has been overlooked [12, 13, 14]. Sutherland had not only derived the same equation independently but also supported his work with experimentation on human albumin. He published his results in a 1904 paper, one year earlier than Einstein, which he presented at an Australian and New Zealand Association for the Advancement of Science (ANZAAS) conference. Hence the diffusion equation given in Eq 1.4 should rightfully referred as Stokes-Einstein-Sutherland relation [15, 14, 13].

Marian Smoluchowski obtained an expression that directly predicted an exponential 'sedimentation equilibrium' equivalent to the aerostatic law describing the variation of atmospheric pressure with height: the same sedimentation equilibrium measured later in the first experiments of Jean Perrin [16]. Two years after Smoluchowski's first publication, Paul Langevin demonstrated another derivation [17]. Langevin's derivation, however, was spectacularly simple and direct

compared to the others. Langevin simply equated forces on the colloidal particle, directly introducing a fluctuating random force to represent the impulses of colliding molecules, and using, as Einstein and Smoluchowski had done, a Stokesian description of the 'opposing' frictional force due to the motion of the particle through the liquid. Langevin concluded his paper with a remark that emphasizes the importance of more accurate measurements, pointing out the importance of determining the exact size of colloids used in experiments. In other words, monodisperse well characterized colloids were required for the exact derivation of the Avogadro number.

1.2.2 Quantitative confirmation

The theoretical description clarified which parameters had to be measured to prove the discontinuous nature of matter by experimental studies of Brownian motion. Theodor Svenberg published the "first results" in 1906 claiming thar his experimental observations were in agreement with Einstein's results [18]. Yet the experiments by Victor Henri 1908 dented the Einsteins work [19]. Henri utilized the pioneering idea of combining microscopy and film camera. Henri's results were in partial agreement with Einsteins work . His work confirmed to a reasonable degree Einstein's prediction of the scaling of the mean square displacement with time, however he found no quantitative agreement with Einstein's formula for the diffusion coefficient. The reason for this inconsistency had been attributed to experimental problems such as intense lighting. Perrin recognized the need for quantitative confirmation. In a set of papers, Perrin and his students in Sorbonne Paris provided precise and patient measurement which finally confirmed the theorists' predictions and settled the molecular kinetic theory on a firm observational basis [20]. To avoid the problems associated with accuracy of particle sizes and velocity measurements that Svenberg faced before, Perrin developed and documented very precise measurement techniques that require optimum patience. In his measurements, Perrin centrifuged gamboge particles, a resin derived from the sap of the tree Garcinia xanthochymus to reach monodisperse micron size particles [21]. What makes Perrin's experiments so valuable that he received the Nobel Prize for his work

in 1921 was the great precision in measurements of particle size, the monodispersity of the colloids he utilized and the high level of statistical accuracy. By designing and executing unprecedented accuracy measurements of Brownian particles, he provided quantitative confirmation of Einstein-Smoluchowski-Langevin's theoretical prediction.

Perrin recognized the experimental difficulties associated with precise measurements of velocity via displacement versus time . Instead he turned to measurements of the sedimentation equilibrium in a colloidal suspension. Sedimentation equilibrium does not directly confirm the diffusion relation, such a measurement could give an estimate of the mean energy of a colloidal particle. Furthermore, measurement of sedimentation equilibrium could also provide an estimate of Avogadro's number,which, when compared with estimates from studies of gases, would further indicate whether Brownian motion might indeed be explained by molecular motion consistent with kinetic theory. Perrin's first experimental paper in 1908 provides a clear description of his first sedimentation experiments, and their analysis which explained the observed exponential distribution of particle concentration with height in the suspension.

Perrin and his students also perfected direct measurements of displacements to confirm Einstein's diffusion theory. Experiments with various of solvent viscosities, with a range of different colloidal materials, and under various external conditions were performed. All the results agreed and hence converted the molecular kinetic theory from a hypothesis to a description of matter. Through Perrin's and his students' efforts, the colloidal suspension had demonstrated the molecular nature of reality and opened up a new field where the various aspects of physical phenomena could be tested using colloids.

1.2.3 From Brownian Motion to our current understanding of Soft Matter

In recent years, predominantly in the last three decades, colloids have been exploited to understand the principles of equilibrium many-body transitions such as fluid-fluid phase separation and hard sphere freezing. The reason behind the popular use of colloidal suspensions for

studying physical phenomena lies in the fact that they can be studied in real-space, that their interactions can be tuned, and that they can be brought into equilibrium with the surrounding molecular solvent. Due to the separation of length scales and times associated with size difference of the colloidal suspensions constituents (i.e. on one hand the colloidal particles on the other hand the solvent molecules), fluctuations of the solvent molecules can be averaged, resulting in a simplification of the system with less degrees of freedom. Furthermore, the interactions between colloidal particles can be tuned to realize a variety of physical systems [22].

As mentioned earlier, colloids can be classified in a large family of materials characterized by so called *Soft Matter*. The materials classified as *Soft Matter* are classified by the consequences of 'thermal forces' (i.e. Brownian motion) on macroscopic properties of matter such as response to external stress and external fields.

The equilibrium states of colloidal suspensions were the first to be addressed both with simulations and experiments [23, 24, 25]. Development of the optical methods such as Light Scattering [26, 27, 28, 28, 29, 24] and Confocal microscopy [30, 31, 32, 33, 34] combined with novel colloidal systems to study phase behavior, first the simple case of Hard sphere like interactions between colloids [35, 24] and later attractive systems have been addressed [36, 37, 38].

Hard sphere systems are the conceptually the simplest many body system. Their phase behavior can be fully described by a single parameter: the density or volume fraction (ϕ). At low volume fractions the equilibrium phase is the fluid phase whereas at high volume fractions the equilibrium phase is the face-centered cubic crystal. The stable fluid and solid phases are separated by a two-phase region with the volume fractions between ϕ = 0.494 and ϕ = 0.545 where two phase coexist provided that the polydispersity is less then 5%. The equilibrium behavior of this hard-sphere system is well understood and reproduced by both simulation and experiment, however, the non-equilibrium behavior is far from settled. It is well established that there exists a glassy regime if the system is densified quickly (no time left to crystallize) above 0.58 volume fraction up to random close packing ϕ =0.64 [39, 40]. There is also experimental evidence that there exists an onset of a glass transition in the su-

percooled regime ($0.494 < \phi < 0.58$) where dynamic heterogeneities are observed [41, 42, 43]. This scenario is both experimentally and theoretically verified [44, 45, 46].

An external field or a carefully chosen boundary condition provides a natural way to control colloidal suspensions [47, 48, 49]. Both the dynamics and structure of colloidal suspensions can be controlled by external fields such as light and shear fields or manipulating the boundary conditions as in confinement and directed colloidal epitaxy. An external field or a boundary condition can be imposed on a colloidal suspension and the response of the suspension can be studied. This idea is rather useful when studying the colloidal suspension out of equilibrium. The non-equilibrium states of colloidal suspensions can be classified in two fractions: static non-equilibrium such as a hard sphere suspension in the glassy state and dynamic non-equilibrium such as sheared hard sphere suspensions. To create a system in dynamic non-equilibrium, the system is constantly brought out of equilibrium in a controlled manner with an external field or dynamically altered boundary condition and upon the dismissal of the external field the system goes back to equilibrium [47, 48].

1.3 Colloidal suspensions under external control

Non equilibrium phases of matter such as glass and gel have been studied using colloidal suspensions as model for a long time [38]. These studies played a crucial role in unraveling the physics behind non-equilibrium phenomena not only for systems that are in static non-equilibrium but also systems brought out of equilibrium with controlled external fields or boundary conditions such as light, shear and confinement [38, 48]. In this thesis, we focus on confinement and hydrodynamic shear, observe how the dynamics and structure is influenced by effects.

1.3.1 Confinement

Confinement is in simplest terms limiting the phase space that colloidal particles can explore. Both the dynamics and structure of colloidal suspensions are altered upon confinement. Furthermore, all kinds of phenomena such as layering, wetting, pre-freezing, capillary condensation are introduced with confining a bulk suspension. One may consider confinement as an external field as confinement modifies the thermodynamic behavior just like other external fields yet in this thesis we consider confinement as a boundary condition. Confinement can be achieved by geometric confinement, light or magnetic fields. In this thesis, only geometric confinement is considered where the colloidal suspensions are placed in tight spaces evoking simple solid geometries. Geometric confinement can be thought of as controlling the boundary conditions or manipulating the dimensions of colloidal suspensions.

Colloidal systems under confinement have been studied early on in the context of manipulating the crystalline order. Pieranski looked at colloidal crystals confined in wedge geometry. Varying the confinement gap with respect to position in the wedge, he observed change in ordering of colloidal crystals [50, 51]. The wedge geometry was later evoked for charged colloids. The crystallization behavior and dynamics of charged colloidal particles in a charged wedge of very low opening angles was examined by experiments [51, 52, 53, 54], theory and simulations [55, 56, 57, 58]. These studies with charged colloidal particles led to the observation of exotic crystalline structures.

Wedge geometry and other parallel confinement schemes were utilized to study dynamics and structure of bidisperse and polydisperse colloidal suspensions [59, 60, 61, 62, 63]. In these measurements, the characteristic confinement length is gradually decreased, upon which the dynamics of the suspension is found to slow down with no major change in structure. Recently, studies suggest that the slowing down of dynamics is connected to glass transition and dynamic heteregeneities [46, 64, 59, 43, 65, 66]. These studies also point out the similarities between the molecular glass transition [67, 68, 69, 70, 71] and the colloidal glass transition [72, 38, 45]. This suggests that intuitions obtained from colloidal suspensions can be transfered to

glass transition at molecular level. Recently, mode coupling theory is also adapted for confined systems and confirm the trends observed in experiments. Yet the dynamics and the morphology of dynamic heterogeneities as a function of the characteristic confinement length are still not well understood.

The geometry of confinement is also an important parameter that is recently exploited for realizing exotic crystal structures in infinitely long cylinders in theoretical studies [73, 74, 75]. Tuning the interactions and the confining geometry leads to new crystalline superstructures which can be exploited as nano-sieves and filtering devices [76]. Experimental systems to realize such systems have not been realized due to difficulty in manufacturing well defined three dimensional confinement geometries. Influence of roughness on dynamics of concentrated colloidal suspensions under confinement is rather under explored field on study, there have been very few simulation studies [77, 58, 78] for molecular systems. Only recently, experimental studies describing roughness as a parameter influencing the dynamics in the vicinity of the surface emerged [61].

1.3.2 Shear fields

A shear stress fields are often used to probe the response of materials in rheology yet they can as well be utilized to bring colloidal suspensions out of equilibrium. Crystals and out of equilibrium phases such as glasses or gels studied under shear produced qualitatively different results from the bulk fluids [79, 80]. Oscillatory shear is found to induce crystallization for monodisperse hard sphere suspensions [81, 82] whereas for polydisperse suspensions irreversible particle rearrangements are encountered [83]. When shear fields are combined with geometric confinement the shear-induced configurations of dense monodisperse colloidal suspensions are altered and a new structure emerges, where layers of particles buckle to stack in a more efficient packing [84].For out of equilibrium phases such as hard spheres in glassy state, the arrangements of colloids under shear occurred in localized irreversible shear transformation zones [85]. Furthermore, a recent study focused on nucleation and growth of charged suspensions, showed that the crystal growth rate and the induction

time for crystallization at a fixed concentration exhibits a maximum as a function of the shear rate [86].

1.4 Outline of the thesis

This thesis is presented in seven chapters. In **Chapter 1** and **Chapter 2**, the underlying physical principles are reiterated, placed into context and the experimental methods utilized are introduced. In **Chapters 3 to 5**, the structure and the dynamics of colloidal suspensions under confinement is studied. In **Chapter 6**, we discuss a novel methodology to inhibit Coffee Stain phenomena. This phenomena' in which an evaporating droplet of a suspension on a substrate leaves behind a ring shaped deposit, occurs due to two underlying effects": contact line pinning and jamming of colloidal particles at triple contact line. An external shear field namely flow fields induced by contact angle manipulation inhibits both underlying effects. In the last two chapters, that is **Chapter 7** & **8**, we study the equilibrium morphologies of liquid droplets on fibers and spheres which are defined by wetting parameters.

Chapter 1 presents a brief introduction to colloidal suspension in broader terms soft matter or complex fluids. We go all the back to initial experiments and scientific discussions that lead to our current understanding of physics of colloidal suspensions. We explain how the ideas conducted in this thesis emerged from the very basic concepts of soft condensed matter physics. **Chapter 2** describes the experimental methods that we utilized and developed to study dynamics and structure of colloidal suspensions in external flow fields such as confinement and hydrodynamic flow fields. Two and three dimensional particle localization and tracking method, development of confinement apparatus and the development of a microfluidic chip for confinement are presented in this chapter.

Chapter 3 presents how the dynamics and structures of colloidal suspensions are influenced by the interplay between confinement, gravity and boundary roughness. This chapter focuses on hard sphere like concentrated suspensions with volume fractions ranging between $\phi = 0.30$ and 0.45. The implications of these effects are discussed as

the suspension is confined between a smooth and a rough wall in a quasi-parallel geometry. In this study, we concluded that confinement is indeed slowing down the dynamics of concentrated suspension yet the effects of gravity and roughness also play a role. **Chapter 4** focuses on dilute suspensions in well defined cylindrical three dimensional cavities where the colloidal suspension can be accessed through microfluidic channels. The influence of the geometry on the spatial dependence of diffusion for dilute colloidal suspensions is studied and a novel experimental method to study diffusion in under arbitrary and well defined confinement geometries is presented. As a continuation of work presented in **Chapter 3**, the effect of a rough substrate on the dynamics and structure of a colloidal suspension is investigated as a function of the volume fraction in **Chapter 5**. In this study, a index matched but not density matched colloidal suspension is slowly sedimented on a well defined rough and a smooth wall as both the dynamics and structure is monitored. Roughness is imposed by sintering colloidal particles to a flat wall.

Typically when a drop of a suspension evaporates on a solid surface, a residue so called "coffee stain" characterized by high density of particles in the circumference relative to center emerges. Due to capillary flow induced by diverging evaporation rates at the contact line, colloidal particles are carried towards the contact line. The particles are jammed [87] and confined due to the intrinsic geometry of the drop on the surface. In **Chapter 6**, by manipulating the contact angle via Electrowetting hence mobilizing the contact line, we introduced shearing flow fields that counteract the aforementioned capillary flow and unjam the particles that are jammed in the vicinity contact line. Here, the morphology and the strength of the hydrodynamic flow fields can be controlled. Ideas presented in this chapter promise immense impact on various relevant analytical and industrial applications such as manufacturing of $\mu Arrays$, inkjet printing of polymer displays.

In a crude definition, wettability is a measure of how much one phase likes the other. Recently, wettability is utilized to explore new synthesis methods to create novel colloidal systems mimicking non-symmetric molecular systems [88]. The idea is so far applied to collection of two and more spheres. In **Chapter 7** & **8**, we investi-

gated first the classic wetting problem of a drop on a fiber and later wetting of a drop on sphere geometry. For the fiber geometry, our investigation revealed a previously unexplored metastability regime and revealed the complete nature of transition between two possible morphologies namely *barrel* and *clam-shell* for a drop on a fiber. For the sphere on a drop geometry, we confirmed the predictions from free energy calculations with experimental results and determined under which conditions the drop will wet the sphere. We believe that our results may open up possibilities to further extend the notion of utilizing wettability to synthesize complex colloidal systems.

Bibliography

[1] T. Graham. Liquid diffusion applied to analysis. *Phil.Roy.Soc.*, 151:183–224, 1861.

[2] R. Brown. A brief account of microscopic observations made in the months of of june, july and august 1827' on the particles contained in the pollen of plants and on the general existence of active molecules in organic and inorganic bodies. *Edinburgh Phil. Journal*, 1:314–319, 1828.

[3] M.D. Haw. Colloidal suspensions, brownian motion, molecular reality: a short history. *J. Phys.: Cond. Matt*, 14(33):7769, 2002.

[4] R.A. Brown. Additional remarks on active molecules. *Edinburgh Journal of Science*, 1:314–319, 1829.

[5] G. Gouy. Notes on brownian motion (translated from french). *J. Physique*, 7:561, 1888.

[6] G. Gouy. On the osmotic balance and concentration of solutions by gravity (translated from french). *C. R. Acad. Sci*, 109:102, 1889.

[7] G. Gouy. Notes on brownian motion (translated from french). *Rev. Gen. Sci*, 6:1, 1895.

[8] E. Nelson. *Dynamical theories of Brownian Motion*. Princeton University Press., 1967.

[9] M.J. Nye. *Molecular reality:A perspective on the scientific work of Perrin*. Elsevier, 1972.

[10] A. Einstein. *Investigations on the Theory of the Brownian movement*. Dover, New York, 1956.

[11] G. Stokes. On the effect of the internal friction of fluids on the pendulums. *Proc. Cambridge Phil. Soc.*, 118:8–106, 1863.

[12] W. B. Russel. Brownian motion of small particles suspended in liquids. *Ann. Rev. Fl. Mech.*, 13(12):425–455, 1983.

[13] P. Hanggi and F. Marchesoni. Introduction: 100 years of brownian motion. *Chaos: An Interdisciplinary Journal of Nonlinear Science*, 15(2):026101, 2005.

[14] T. M. Squires and J. F. Brady. A simple paradigm for active and nonlinear microrheology. *Physics of Fluids*, 17(7):073101, 2005.

[15] W. Sutherland. A dynamical theory of diffusion for non-electrolytes and the molecular mass of albumin. *Philosophical Magazine*, 9:781–785, 1905.

[16] M. Smoluchowski. The kinetic theory of brownian molecular motion and suspensions (translated from french). *Ann. Phys., Paris*, 21:772, 1906.

[17] P. Langevin. The theory of brownian movement (translated from french). *C. R. Acad. Sci., Paris*, 146:530, 1908.

[18] T. Svedberg. Svedberg's early studies in colloid chemistry reprinted by blackwell science inc,1987(translated from german). *Z.Elektrochem*, 12:853, 1906.

[19] V. Henri. Investigations of brownian motion (translated from french). *C. R. Acad. Sci., Paris*, 146:1024, 1908.

[20] J. Perrin. Brownian motion and molecular reality (translated from french). *Ann. Chim. Phys.*, 18:1, 1909.

[21] J. Perrin. *Atoms*. Constable,New York, 1916.

[22] A. Yethiraj and A. van Blaaderen. A colloidal model system with an interaction tunable from hard sphere to soft and dipolar. *Nature*, 421(6922):513–517, 2005.

[23] P. N. Pusey and W. van Megen. Phase behaviour of concentrated suspensions of nearly hard colloidal spheres. *Nature*, 320(27):340–342, 1986.

[24] W. van Megen, S. M. Underwood, and P. N. Pusey. Nonergodicity parameters of colloidal glasses. *Phys. Rev. Lett.*, 67(12):1586–1589, Sep 1991.

[25] K. E. Davis, W. B. Russel, and W. J. Glantschnig. Disorder-to-Order Transition in Settling Suspensions of Colloidal Silica: X-ray Measurements. *Science*, 245(4917):507–510, 1989.

[26] A. Vrij. Mixtures of hard spheres in the percus–yevick approximation. light scattering at finite angles. *J. Chem. Phys.*, 71(8):3267–3270, 1979.

[27] P. N. Pusey, H. M. Fijnaut, and A. Vrij. Mode amplitudes in dynamic light scattering by concentrated liquid suspensions of polydisperse hard spheres. *J. Chem. Phys.*, 77(9):4270–4281, 1982.

[28] A. P. Philipse and A. Vrij. Determination of static and dynamic interactions between monodisperse, charged silica spheres in an optically matching, organic solvent. *J. Chem. Phys.*, 88(10):6459–6470, 1988.

[29] A. P. Philipse and A. Vrij. Preparation and properties of nonaqueous model dispersions of chemically modified, charged silica spheres. *J. Coll. Int. Sci.*, 128(1):121 – 136, 1989.

[30] A. Van Blaaderen, A. Imhof, W. Hage, and A. Vrij. Three-dimensional imaging of submicrometer colloidal particles in concentrated suspensions using confocal scanning laser microscopy. *Langmuir*, 8(6):1514–1517, 1992.

[31] A. van Blaaderen and P. Wiltzius. Real-Space Structure of Colloidal Hard-Sphere Glasses. *Science*, 270:1177–1179, November 1995.

[32] J. C. Crocker and D. G. Grier. Methods of Digital Video Microscopy for Colloidal Studies. *J. Coll. Int. Sci.*, 179(1):298–310, April 1996.

[33] A. D. Dinsmore, E. R. Weeks, V. Prasad, A. C. Levitt, and D. A. Weitz. Three-Dimensional Confocal Microscopy of Colloids. *Applied Optics*, 40(24):4152–4159, 2001.

[34] V. Prasad, D. Semwogerere, and E. R. Weeks. Confocal microscopy of colloids. *J. Phys.: Cond. Matt*, 19(11):113102, March 2007.

[35] A. P. Philipse and A. Vrij. Polydispersity probed by light scattering of secondary particles in controlled growth experiments of silica spheres. *J. Chem. Phys.*, 87(10):5634–5643, 1987.

[36] C. G. De Kruif, P. W. Rouw, W. J. Briels, M. H. G. Duits, A. Vrij, and R. P. May. Adhesive hard-sphere colloidal dispersions. a small-angle neutron-scattering study of stickiness and the structure factor. *Langmuir*, 5(2):422–428, 1989.

[37] P. W. Rouw and C. G. de Kruif. Adhesive hard-sphere colloidal dispersions: Fractal structures and fractal growth in silica dispersions. *Phys. Rev. A*, 39(10):5399–5408, May 1989.

[38] P. N. Pusey. Colloidal glasses. *J.Phys.:Cond.Matt.*, 20(49):0953–8984, 2008.

[39] E. Zaccarelli, G. Foffi, K. A. Dawson, S. V. Buldyrev, F. Sciortino, and P. Tartaglia. Confirmation of anomalous dynamical arrest in attractive colloids: A molecular dynamics study. *Phys. Rev. E*, 66(4):041402, Oct 2002.

[40] E. Zaccarelli, C. Valeriani, E. Sanz, W. C. K. Poon, M. E. Cates, and P. N. Pusey. Crystallization of Hard-Sphere Glasses. *Phys. Rev. Lett.*, 103(13):135704, Sep 2009.

[41] G. Adam and J. H. Gibbs. *The J.Chem. Phys.*, 43(1):139–146, 1965.

[42] W. K. Kegel and A. van Blaaderen. Direct Observation of Dynamical Heterogeneities in Colloidal Hard-Sphere Suspensions. *Science*, 287(5451):290–293, 2000.

[43] E. R. Weeks, J. C. Crocker, A. C. Levitt, A. Schofield, and D. A. Weitz. Three-Dimensional Direct Imaging of Structural Relaxation Near the Colloidal Glass Transition. *Science*, 287(5453):627–631, 2000.

[44] W. G. Hoover and F. H. Ree. Melting transition and communal entropy for hard spheres. *J.Chem.Phys.*, 49(8):3609–3617, 1967.

[45] W. Van Megen. Freezing, melting and the glass transition in a suspension of hard spheres. *J. Phys.: Cond. Matt*, 14(33):7699+, August 2002.

[46] A. H. Marcus and S. A. Schofield, J.and Rice. Experimental observations of non-Gaussian behavior and stringlike cooperative dynamics in concentrated quasi-two-dimensional colloidal liquids. *Phys. Rev. E*, 60(5):5725–5736, Nov 1999.

[47] H. Löwen. Colloidal soft matter under external control. *J. Phys.: Cond. Matt*, 13(24):R415+, June 2001.

[48] H Löwen. Colloidal dispersions in external fields: recent developments. *J. Phys.: Cond. Matt*, 20(40):404201, 2008.

[49] D. Vollmer. Time- and space-resolved recording in studies of soft matter dynamics. *Soft Matter*, 2:445–447, 2006.

[50] P. Pieranski, L. Strzelecki, and B. Pansu. Thin colloidal crystals. *Phys. Rev. Lett.*, 50(12):900–903, 1983.

[51] C. Murray. Phases of thin colloidal layers. *MRS Bulletin*, 23(10):33–38, OCT 1998.

[52] A. B. Fontecha, H. J. Schope, H. Konig, T. Palberg, R. Messina, and H. Lowen. A comparative study on the phase behaviour of highly charged colloidal spheres in a confining wedge geometry. *J. Phys.: Cond. Matt*, 17(31):S2779–S2786, 2005.

[53] P. Wette, H. J. Schope, and T. Palberg. Crystallization in charged two-component suspensions. *J. Chem. Phys.*, 122(14):144901, 2005.

[54] H. J. Wette, P.and Schope and T. Palberg. Microscopic investigations of homogeneous nucleation in charged sphere suspensions. *J. Chem. Phys.*, 123(17):174902, 2005.

[55] Z. T. Németh and H. Löwen. Freezing and glass transition of hard spheres in cavities. *Phys. Rev. E*, 59(6):6824–6829, 1999.

[56] T. Fehr and H. Löwen. Glass transition in confined geometry. *Phys. Rev. E*, 52(4):4016–4025, 1995.

[57] W. Kob P. Scheidler and K. Binder. The relaxation dynamics of a simple glass former confined in a pore. *EPL*, 52(3):0295–5075, 2000.

[58] W. Kob P. Scheidler and K. Binder. Cooperative motion and growing length scales in supercooled confined liquids. *EPL*, 59(5):701–707, 2002.

[59] C.R. Nugent, K. V. Edmond, H. N. Patel, and E. R. Weeks. Colloidal glass transition observed in confinement. *Phys. Rev. Lett.*, 99(2), 2007.

[60] Prasad S. Sarangapani and Yingxi Zhu. Impeded structural relaxation of a hard-sphere colloidal suspension under confinement. *Phys. Rev. E*, 77(1), 2008.

[61] K. V. Edmond, C. R. Nugent, and E. R. Weeks. Influence of Confinement on Dynamical Heterogeneities in Dense Colloidal Samples. *arXiv:1003.0856*, Mar 2010.

[62] K. W. Desmond and E. R. Weeks. Random close packing of disks and spheres in confined geometries. *Phys. Rev. E*, 80(5):051305, 2009.

[63] M. Hermes and M. Dijkstra. Jamming of polydisperse hard spheres: The effect of kinetic arrest. *EPL (Europhysics Letters)*, 89(3):38005, February 2010.

[64] S. C. Glotzer. Spatially heterogeneous dynamics in liquids: insights from simulation. *Journal of Non-Crystalline Solids*, 274(1-3):342–355, September 2000.

[65] E. R. Weeks and D. A. Weitz. Properties of cage rearrangements observed near the colloidal glass transition. *Phys. Rev. Lett.*, 89(9):095704, 2002.

[66] E. R. Weeks and D. A. Weitz. Subdiffusion and the cage effect studied near the colloidal glass transition. *Chem. Phys.*, 284(1-2):361 – 367, 2002.

[67] C. A. Angell. Formation of Glasses from Liquids and Biopolymers. *Science*, 267(5206):1924–1935, 1995.

[68] M. D. Ediger. Spatially heterogeneous dynamics in supercooled liquids. *Ann. Rev. Phys. Chem.*, 51(1):99–128, 2000.

[69] C. A. Angell, K. L. Ngai, G. B. McKenna, P. F. McMillan, and S. W. Martin. Relaxation in glass forming liquids and amorphous solids. *J.Appl. Phys.*, 88(6):3113–3157, 2000.

[70] M. Alcoutlabi and G. B. McKenna. Effects of confinement on material behaviour at the nanometre size scale. *J. Phys.: Cond. Matt.*, 17(15):R461–R524, 2005.

[71] C. Alba-Simionesco, B. Coasne, G. Dosseh, G. Dudziak, K. E. Gubbins, R. Radhakrishnan, and M. Sliwinska-Bartkowiak. Effects of confinement on freezing and melting. *J. Phys.: Cond. Matt*, 18(6):R15–R68, 2006.

[72] P. N. Pusey and W. van Megen. Observation of a glass transition in suspensions of spherical colloidal particles. *Phys. Rev. Lett.*, 59(18):2083–2086, Nov 1987.

[73] E. C. Oguz, R. Messina, and H. Löwen. Crystalline multilayers of the confined yukawa system. *EPL (Europhysics Letters)*, 86(2):28002, 2009.

[74] E. C. Oguz, R. Messina, and H. Löwen. Multilayered crystals of macroions under slit confinement. *J. Phys.: Cond. Matt*, 21(42):424110, 2009.

[75] E. Allahyarov, I. D'Amico, and H. Löwen. Effect of geometrical confinement on the interaction between charged colloidal suspensions. *Phys. Rev. E*, 60(3):3199–3210, Sep 1999.

[76] F. Li, Z. Wang, N. S. Ergang, C.A. Fyfe, and A. Stein. Controlling the shape and alignment of mesopores by confinement in colloidal crystals: Designer pathways to silica monoliths with hierarchical porosity. *Langmuir*, 23(7):3996–4004, 2007.

[77] Z. T. Németh and H. Löwen. Freezing and glass transition of hard spheres in cavities. *Phys. Rev. E*, 59(6):6824–6829, June 1999.

[78] P. Scheidler, W. Kob, and K. Binder. The Relaxation Dynamics of a Supercooled Liquid Confined by Rough Walls. *J. Phys. Chem. B*, 108(21):6673–6686, May 2004.

[79] R. Blaak, S. Auer, D. Frenkel, and H. Löwen. Crystal nucleation of colloidal suspensions under shear. *Phys. Rev. Lett.*, 93(6):068303, Aug 2004.

[80] Y.L Wu, D. Derks, A van Blaaderen, and A Imhof. Melting and crystallization of colloidal hard-sphere suspensions under shear. *Proceedings of the National Academy of Sciences*, 106(26):10564–10569, 2009.

[81] W. Xue and G. S. Grest. Shear-induced alignment of colloidal particles in the presence of a shear flow. *Phys. Rev. Lett.*, 64(4):419–422, Jan 1990.

[82] M. D. Haw, W. C. K. Poon, and P. N. Pusey. Direct observation of oscillatory-shear-induced order in colloidal suspensions. *Phys. Rev. E*, 57(6):6859–6864, Jun 1998.

[83] G. Petekidis, A. Moussaïd, and P. N. Pusey. Rearrangements in hard-sphere glasses under oscillatory shear strain. *Phys. Rev. E*, 66(5):051402, Nov 2002.

[84] I. Cohen, T. G. Mason, and D. A. Weitz. Shear-induced configurations of confined colloidal suspensions. *Phys. Rev. Lett.*, 93(4):046001, Jul 2004.

[85] P. Schall, D. A. Weitz, and F. Spaepen. Structural Rearrangements That Govern Flow in Colloidal Glasses. *Science*, 318(5858):1895–1899, 2007.

[86] P. Holmqvist, M. P. Lettinga, J. Buitenhuis, and J. K. G. Dhont. Crystallization kinetics of colloidal spheres under stationary shear flow. *Langmuir*, 21(24):10976–10982, 2005.

[87] A. J. Liu and S. R. Nagel. Jamming is not just cool any more. *Nature*, 396(6706):21–22, November 1998.

[88] D. J. Kraft, J. Groenewold, and W. K. Kegel. Colloidal molecules with well-controlled bond angles. *Soft Matter*, 5:3823–3826, 2009.

2 Instrumental Methods

Abstract In the introductory chapter, we reiterated the idea that external fields and boundary conditions can be evoked to manipulate dynamics of colloidal suspension. In this chapter, the instruments and the experimental methods utilized to manipulate the boundary conditions, create external fields and probe dynamics and structure are described. The methods to manipulate the boundary conditions and external fields utilized throughout the thesis are confinement, roughness, gravity, and hydrodynamic flow fields induced by Electrowetting. The instruments discussed are Confocal Microscope, confinement apparatus, the microfluidic confinement chip and the electrowetting setup to create shear flow fields. Furthermore, the methodology to probe structure and dynamics of colloidal suspensions are discussed.

2.1 Introduction

The experimental methods evoked in the course of the thesis are described in this chapter. Starting from the instrumentation, the experimental techniques probing the dynamics and the structure of colloidal suspensions under control of carefully manipulated boundary conditions and external fields such as confinement, roughness, gravity and hydrodynamic flows are iterated. Confocal microscopy and particle tracking techniques utilized to probe the dynamic and structure, confinement apparatus utilized to confine colloidal suspensions in a quasi-parallel geometry, Force measurements with strain gauges integrated to confinement apparatus, microfluidic confinement chip developed to confine colloidal suspensions in well defined confining geometries and electrowetting setup evoke to beat coffee stain effect i.e. jamming of colloidal particle at the contact line in an evaporating droplet are discussed respectively.

2.2 Confocal Microscopy

Confocal scanning laser microscopy (CSLM) is an optical imaging technique that increases the resolution and the contrast by eliminating out of focus light. The principle of CSLM was patented by Marvin Minsky [1] to overcome the limitations of traditional fluorescence microscopy. In traditional fluorescence microscopy, each volume element of the sample is illuminated simultaneously and the resulting fluorescence light both in and out of focus from the whole volume is detected. This method brings our considerable background noise. Whereas CSLM uses certain optical methods to eliminate out-of-focus light (Fig. 2.1a). These optical methods can be either point by point illumination or a series of rotating disks and a pinhole in an optically conjugate focal plane in front of the detector. As only light produced by volume elements close to the focal plane can be detected, the optical resolution, particularly in the sample depth direction, is much better than that of wide-field microscopes. The superior optical resolution comes at a cost, as the image is built point by point only a small fraction of the fluorescent light is used so higher exposure

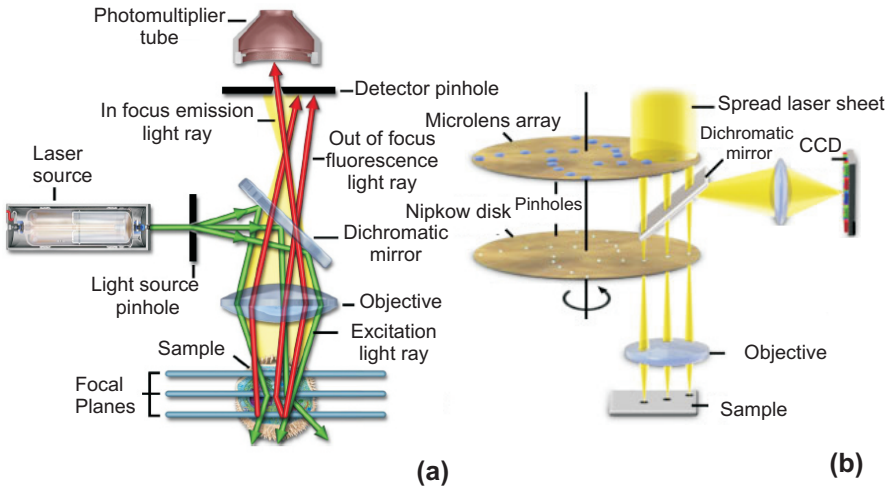

Figure 2.1: Panel (a) is the illustration of the Confocal Scanning Laser Microscope and Panel (b) illustrates the Nipkow disk. Images are adapted from manufacturers webpage http://www.olympusfluoview.com/theory/

times are required. The achievable width of the focal plane is defined mostly by the wavelength of the used light divided by the numerical aperture of the objective lens, but also by the optical properties of the specimen. The thin optical sectioning possible make these types of microscopes particularly suitable for at 3D imaging and surface profiling of samples.

There are several types of CSLMs depending on the details of the optical system used. Three most commonly used types are point or line scanning, spinning-(Nipkow) disk (Fig. 2.1b) and programmable array microscopes. Each of these classes of confocal microscope have particular advantages and disadvantages; most systems are either optimized for resolution or high recording speed (i.e. video capture). CSLM image the sample point by point or line by line. Imaging frame rates are typically very slow for laser scanning systems (e.g. less than 3 frames/second). Commercial spinning-disk Nipkow confocal microscopes achieve frame rates of over 50 per second - a desirable feature for dynamic observations such as colloidal suspensions

and live cell imaging. Cutting edge development in CSLM now allows better than video rate (up to 200 frames/second) imaging by using multiple microelectromechanical systems based scanning mirrors. Due to its high resolution and versatility, confocal has been used in soft matter physics to study particle dynamics in colloidal glasses [2, 3], living cells [4] and actin networks [5].

2.2.1 Particle tracking

Methods to track particles have evolved since the early measurements of Perrin where he used pencil and graph paper. Currently dynamics of up to several thousands colloidal particles can be studied by tracking the position of the particles over time with open source algorithms. A fluorescent particle imaged by CSLM with 100X objective appear like a airy disks as seen in Figure 2.2 extending over typically 5 to 7 pixels for a particle of one micron diameter. By fitting the intensity profile with a 2D Gaussian profile, the center position of the particle can be determined with subpixel accuracy up to 0.05 pixel accuracy: for a micron size particle, the center of mass can be determined up to 6 nm accuracy. The trajectory tracer particles is determined by connecting the center of mass position in consecutive frames. From the ensemble averaging of trajectories statistical indicators such as the mean square displacement (MSD) or the probability distribution function are calculated from spatial and temporal averaging over trajectories of contributing particles with Eq. 2.1.

$$\langle x^2(\tau)\rangle = \left\langle [x(t+\tau) - x(t)]^2 \right\rangle \tag{2.1}$$

where x(t) are the X-position of a particle at real time t, τ is the lag time, the $\langle\rangle$ brackets indicate an averaging over all times t and all particles.

The MSD measured using Eq. 2.1 is in the case of an Newtonian fluid related to the diffusion cefficent (D) by the Stokes-Einstein-Sutherland relation $\langle r^2(\tau)\rangle = 2dD\tau$ and $D = \frac{kT}{6\pi a\eta}$ where Boltzmann constant (k), molar gas constant (R), the absolute temperature (T), the dimension (d) i.e. d=1 for 1D, the particle radius (a), and the solvent viscosity (η).

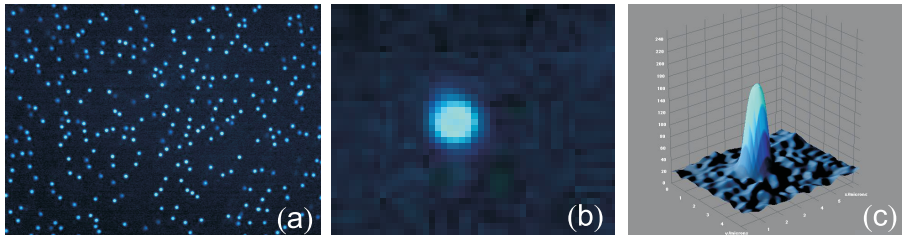

Figure 2.2: Illustration of particle detection and tracking. Panel (a) provides a characteristic image from CSLM where the 1.1 μm particles in water-DMSO exhibit Brownian motion. Panel (b) is a close up on one individual particle and panel (c) demonstrates the intensity profile of the the particle in panel (b)

Provided that the particles are moving slow enough, as in glassy samples, they can be localized and tracked in three dimensions (Fig. 2.3). This is achieved by moving the confocal plane along the sample which results in a stack of 2D images. Later this stack of 2D images are subjected to a 3D reconstruction operation. This 3D imaging capability combined with the pinhole that filters out background fluorescence and careful index matching makes CSLM an important tool to study concentrated suspensions and in broader terms soft matter.

Displacement resolution

In confined colloidal systems, the particle displacements can be surprisingly small hence one should know exactly the resolution of CSLM to quantify reliability of measuring such motion.

This quantity is determined by tracking particles glued to the surface. The glued particles are prepared by evaporating a drop of dilute suspension of $1.1\mu m$ carboxylated polystyrene particles on a glass slide and subsequently sintering the particles at $50°C$. The center of mass positions of the particles are recorded over 2400 s with one frame per second frame rate using CSLM at 100x magnification. The recorded images are processed by openware particle tracking codes written in IDL and MSD is calculated both by spatial and temporal

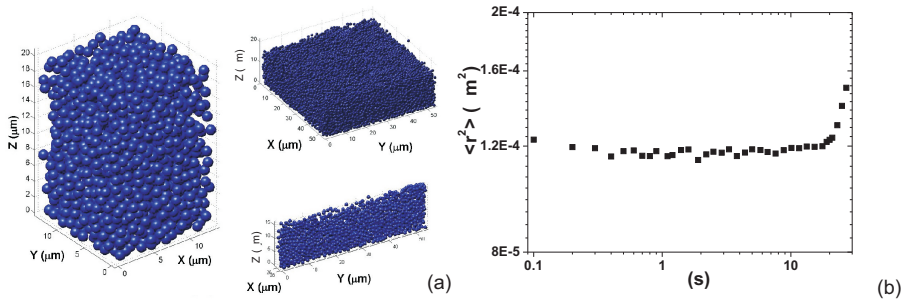

Figure 2.3: 3D localization of a dense suspension of colloidal particles.Panel (a) provides images of 3D localized colloidal particles with different perspectives. The images are reconstructed from z scanning through a dense suspension of 1.1 μm core shell silica particles dispersed in a reflective index matching Water-DMSO mixture. Panel (b) provides the MSD of sintered particles.

averaging [6].

The Figure 2.3b shows the MSD of the sintered particles where at short times MSD flattens out at $\approx 1.1 * 10^{-4} \mu m^2$. In displacement terms this is equal to 10 nms. At long times the apparent MSD increases which is an indication of mechanical drift. From this measurement, we conclude that the displacement resolution at short times has is approximately 10 nms.

2.2.2 Confinement apparatus

In concentrated suspensions several length scales are important depending on the particle size, volume fraction and interaction potential. Probing the effect of confinement on dynamics and structure with requires development of specific instrument capable of accessing the relevant dimensions. This instrument should not only provide access to relevant length scales but also provide low drift and stability.

In this part of the thesis, we describe an apparatus capable of confining concentrated suspensions to dimensions ranging all the way down to single particle diameter. The apparatus which we call *confinement apparatus* utilizes a quasiparallel geometry to confine col-

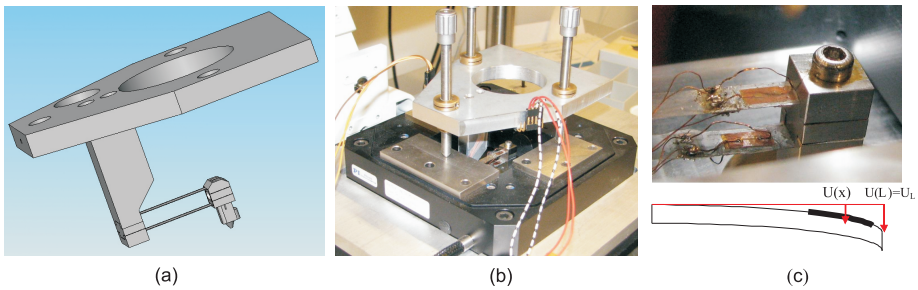

Figure 2.4: Panel (A) provides the 3D detailed illustration *confinement apparatus* and Panel (B) is a photograph of the *confinement apparatus* resting on a piezo stage. Panel (C) provides a close up photograph of the strain gauges glued onto cantilevers.

loidal suspensions between two boundary walls separated at a well defined, adjustable distance. The quasiparallel geometry is realized by holding a sphere with double cantilevers at a given distance from a flat surface. Adding strain gauges to cantilevers also allow for force measurements. Provided the spheres size much bigger then the size of colloidal particles the quasiparallel approximation holds. The *confinement apparatus* is integrated with a Nipkow disk confocal laser microscopy (CSLM) for simultaneous detection of dynamics and structure of colloidal suspensions under confinement.

Our home-made *confinement apparatus* (CA) is sketched in Figure 2.4, consists of a glass sphere which can be positioned a well difined distance above a flat glass substrate. The sphere (D_{sphere} = 2 mm, Duke Scientific) is glued onto a holder, which is connected to the CA tripod via stiff double cantilevers. The tripod rests on a piezo stage via 3 micro screws. Coarse control over the gap height (H) is achieved via the screws, and guided by a visualization using fluorescent liquid. Fine control is achieved using a computer driven piezo stage (Physik Instrumente) with a vertical range of 20 μm, and an accuracy of 0.01 μm. In typical measurements, $D_{sphere} >> H$, which means that an effective plane-plane geometry is obtained, independent of the precise alignment.

2.2.3 Force measurements with confinement apparatus

In this section, we discuss the design and modeling of the strain gauge based Force sensor integrated into the *confinement apparatus* and CSLM. This additional feature combines the visualization capabilities of CSLM with complementary force measurements. Although the force measurement feature is not used in studies reported in Chapter 3 as the resulting forces during confinement turned out to be much smaller then the detection limit, we still present the complete design including the force sensor. The setup consists of three units namely: (a) approach/retraction system, (b) deflection detection, (c) data collection and experimental control unit (See Fig. 2.5).

The approach/retraction unit is responsible for adjusting the confinement gap. It consists of a piezo stage and micro-screws to move the cantilevers. The coarse approach is done by micro-screws and fine approach by piezo stage. This part of the system is the most vulnerable to drift. Special care has to be taken to minimize drift such as utilizing microscrews with ball bearings sitting on slits and heavy metal tripod.

The force required to confine colloidal suspension is measured with the deflection detection system consisting of a Wheatstone bridge of four strain gauges (Fig. 2.4c) glued on cantilevers , a Lock in amplifier to supply the bridge with a well defined amplitude and frequency and to eliminate noise in the detected signal. Change in resistance due to bending is registered as change in voltage (V_{bridge}). In order to increase sensitivity extra resistors are added to compensate for the offset of the bridge. The details of optimal bridge design is discussed in Sec. 2.2.4.

The "data collection and control unit" consists of a data acquisition card (DAQ card) to simultaneously control the piezo stage and record output voltage from the bridge (V_{bridge}). This unit can be used both as a proximity sensor and a force sensor depending on how the V_{bridge} signal is processed. Since the V_bridge is proportional to the relative position of the sphere with respect to the flat plate, it can be used to either monitor the position of the sphere of the force. V_{bridge} be used to calculate the force with a calibration curve. Such a

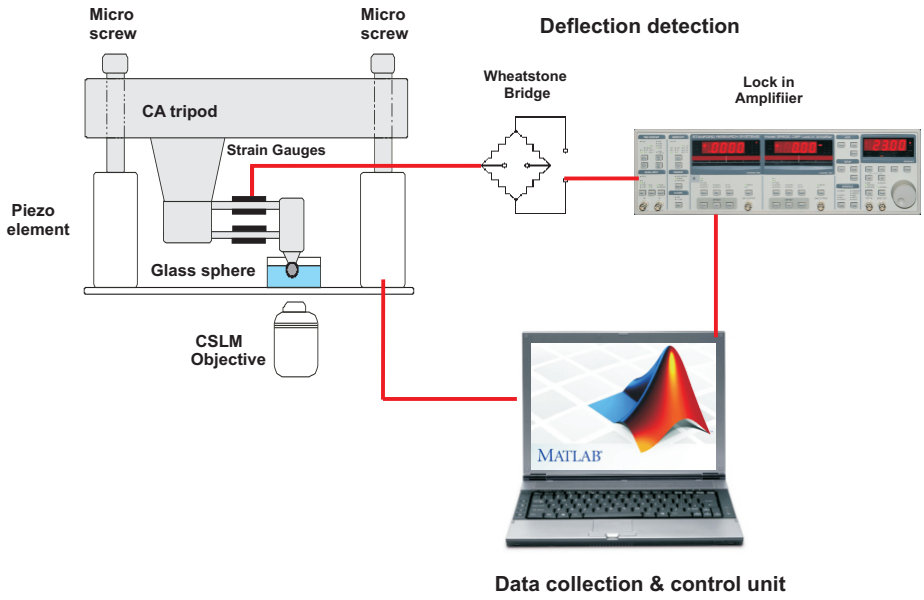

Figure 2.5: The detailed illustration of force sensor integrated into the *confinement apparatus*

calibration curve can be prepared by adding micro weights on the cantilevers and measuring the resulting V_{bridge} signal. The corresponding displacement vs. V_{bridge} relation can be determined by simply calibrating the system in contact with a solid surface. Comparing the slope of both curves yields a value for the stiffness of the spring constant of the double cantilever arrangement. The spring constant can be also be estimated from the from the dimensions of the cantilevers (b:width, h:thickness, L:length) and the elasticity of the material (E) with the formula $k = \frac{2Ebh^3}{L^3}$ is found to be 74.074 N/m. The same quantity calculated from the Force vs. piezo displacement is 73.25 N/m. These values show good agreement confirming the consistency of our approach.

To estimate the sensitivity of the bridge, we consider an ideal Wheatstone bridge in Figure 2.6a and derive the equations to connect Force applied to measured bending signal V_{bridge}. A more detailed

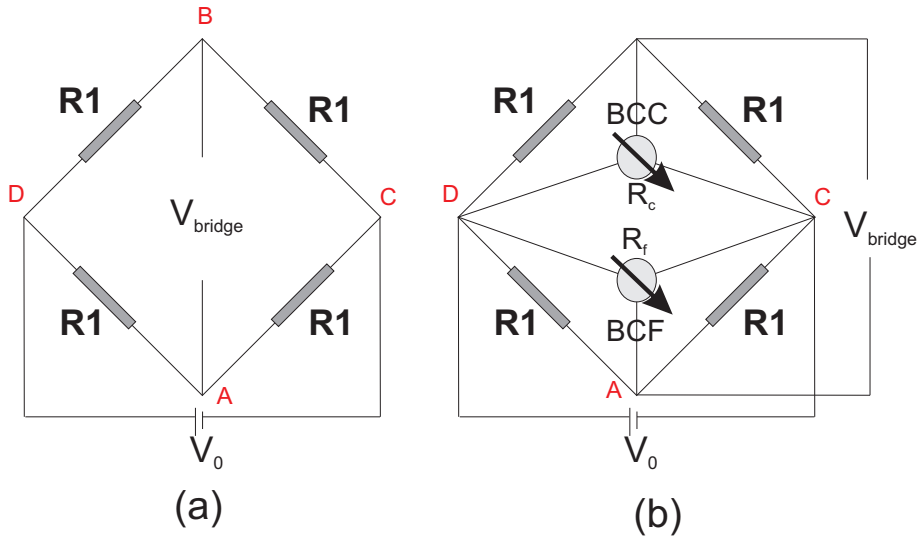

Figure 2.6: Panel (A) illustrates the classic Wheatstone Bridge and Panel (B) illustrates the Modified Wheatstone Bridge.

derivation is given in Appendix. For optimal sensitivity, the gauges are mounted such that when the cantilevers are bended; the resistances R1 and R3 will increase, R2 and R4 will decrease (Fig. 2.6). For a strain gauge, the variation in R with the bending will be given by

$$F_{ext} = 2F_l = \frac{2Ebh^3}{L^3} u_L \tag{2.2}$$

$$\frac{\delta R}{R} = \alpha \epsilon_s = C \frac{h u_L}{L^2} \tag{2.3}$$

where C is a constant dependent of system parameters. Hence we obtain

$$\frac{\delta R}{R} = C \frac{h u_L}{L^2} = \frac{Ch}{kL^2} F_{ext} \tag{2.4}$$

For an ideal bridge, the bridge voltage V_{bridge} will be given by

$$\frac{V_{bridge}}{V} = \frac{\delta R}{R} = C\frac{hu_L}{L^2} \tag{2.5}$$

In terms of force, $\frac{V_{bridge}}{V_0}$ can be written as

$$\frac{V_{bridge}}{V_0} = C\frac{hu_L}{L^2}F_{ext} \tag{2.6}$$

With Eq. 2.5 and Eq. 2.6, the bridge voltage is connected to the displacement or force.

2.2.4 Optimal Wheatstone Bridge

To obtain the optimal sensitivity from the Wheatstone bridge, bridge has to be in perfect balance in unloaded situation i.e. all the resistances prior to bending has to be same. Yet due to their intrinsic properties of strain gauges, it is not possible to get identical strain gauges. This limits the sensitivity of Wheatstone bridge, to measure smaller displacements bridge has be be compensated. The standard Wheatstone bridge given in Figure 2.6b is modified Wheatstone bridge composed of four strain gauges and two potentiometers. With the coarse and the fine adjustments the bridge can be compensated to minimum compensation error of 0.1 μV dramatically better then the value for a standard Wheatstone bridge 2 mVs.

2.2.5 Microfluidic chip for confinement

Confinement as the word implies is placing a suspension in a tight place and limiting the phase space of particles by altering the boundary conditions. It is rather effortless operation in simulation studies yet confining micron scale particles in micron scale well defined objects might be an experimentalists' nightmare. In simple terms there are three requirements for an optimal confinement setup: the confinement cell has to be well defined, particles have to be placed/removed with ease and the setup microscopy. Microfluidics provides a solution where all the requirements are fulfilled. We developed an multilayer

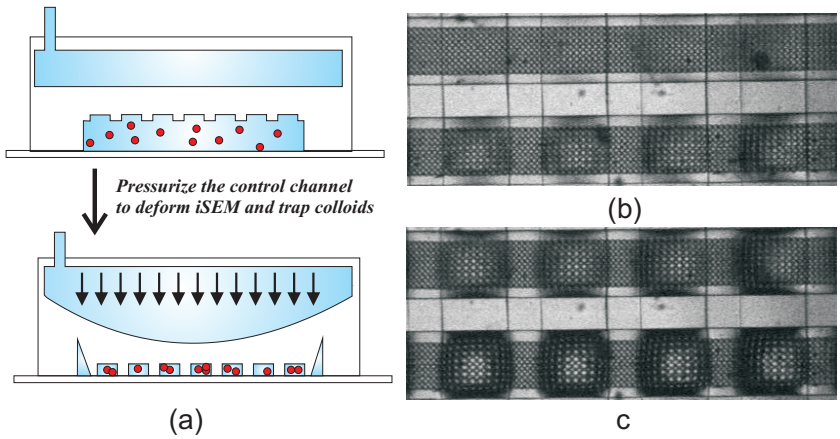

Figure 2.7: Illustration of the iSEM. Panel (a) demostrates the working principles of iSEM Panel (b) and (c) are confocal images of the iSEM where the pressure is off and on respectively.

microfluidic chip where the colloidal particles are confined in well defined three dimensional cavities so called iSEMs integrated structural membranes. The idea relies on the multilayer, elastic chips made of PDMS utilizing a cross channel geometry where the previously developed as microfluidic valves [7, 8]. The membrane separating the crossed channels is flexible. The membrane bends and blocks the bottom channel upon application of pressure to the top channel. We further developed the idea by adding three dimensional (3D) open cavities integrated to the membrane separating two crossed channels. Upon application of the open 3D cavities are pushed towards the bottom wall and 3D closed confining cells are formed. These confining cells can be designed of any shape within the limitations of soft lithography providing flexibility in design and easy access to confining geometry. They can be used to study confinement effects in various materials beyond colloidal suspensions.

In a nutshell, two separate molds are prepared one for the control channels and one for the membrane and the fluid channels. First, the fully cured/crosslinked control channels pealed from the mold are placed in a crossed geometry on the top of the partially cured

membrane and fluid channels. This assembled structure is fully cured overnight and later placed on the top of a glass slide spin coated with PDMS. The details of the manufacturing process can be found literature [9, 7, 8].

2.2.6 Hydrodynamic flow fields induced by Electrowetting

The basis of electrowetting (EW) was described in detail first by Gabriel Lippmann in 1875 [10]. Lippmann described the capillary depression of mercury in contact with electrolyte solutions could be varied by applying a voltage between the mercury and electrolyte. Electrowetting essentially alters the balance established by surface tension of three phases (γ_{SV}: solid-vapor, γ_{SL}:solid-liquid,γ_{LV}:liquid-vapor) by introducing a electric force.

$$cos\theta_Y = \frac{\gamma_{SV} - \gamma_{SL}}{\gamma_{LV}}, \tag{2.7}$$

In EW, the contact angle follows the Young-Lippman equation (Eq. 2.8) which is obtained by the force balance at three phase contact line (TCL) between the surface tension of three phases and the electric force. In Equation. 8.1), θ_Y is Young's angle and the electrowetting number η is defined by the vacuum permeability ε_0, the dielectric constant ε_r, the dielectric layer thickness δ, and the surface tension σ.

$$\cos\theta = \cos\theta_Y + \eta, \quad \eta \equiv \frac{\varepsilon_0 \varepsilon_r U^2}{2\delta\sigma}, \tag{2.8}$$

The classic EW setup (Fig. 2.8a) consists of a sessile drop placed on the top of a dielectric layer coated on a conducting electrode. In this thesis, Indium Tin Oxide (ITO) layer deposited on the glass substrate is used as it provides the conducting electrode for EW along with transparency required for observing the sessile drop from the bottom. A potential difference (U) is applied between the droplet and the ITO layer by inserting an inert platinum wire in the droplet. Alternatively interdigitated electrodes can be used to archive the same

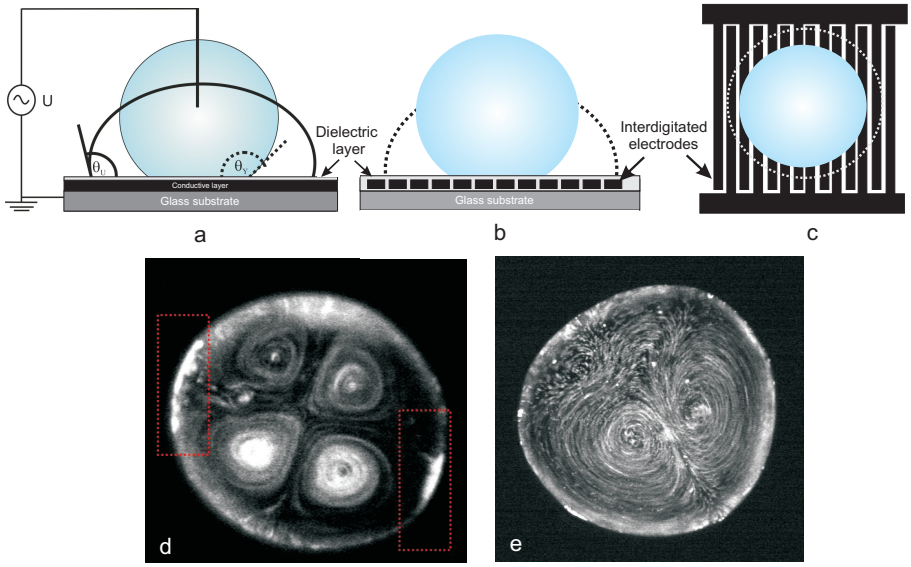

Figure 2.8: Illustration of EW setup and the hydrodynamic flow fields induced by EW. Panel (a) is the classic EW substrate. Panel (b) and (c) are the side and top view of interdigitated EW setup. Panel (d) and (e) are confocal images flows created by 1kHz 200V applied voltage to 0.5 μl drops. The drop consist of 5 μm diameter fluorescent particles dissolved in 0.01 M LiCl in water.

effect (Fig. 2.8b).In this wire-free setup, the ITO layer is lithographically patterned to form interdigitated electrodes and electric field is created between two adjacent electrodes. The dielectric materials commonly utilized in this thesis are Teflon AF, SU-8 and various polymeric thin films such as high density polyethlene, High density polystrene.

It is well established that hydrodynamic flows can alter the dynamics of soft matter systems as described in the introduction chapter. Electrowetting (EW) provides a mean to dynamically manipulate the contact angle [11] hence interface morphology for a body of fluid such as a drop. The changes in the shape of the fluid in return creates hydrodynamic flows that alter the dynamics of soft systems. EW exerts a dielectric force on the TCL while the contact angle is manipulated

the shape of the drop is altered. This shape altering transition gives birth to aforementioned hydrodynamic flows (Fig. 2.8d-e). Motion of TCL can be dynamically controlled by controlling the amplitude and the frequency of the applied potential difference hence internal flow patterns can be manipulated [12, 13, 14, 15]. The details and the governing mechanism of the hydrodynamic flow field induced by EW depends on various parameters such as the conductivity, surface tension of the drop and the surrounding fluid, frequency of applied potential difference, contact angle hysteresis and number of pinning sites.

2.3 Appendix

2.3.1 Simple considerations for Wheatstone Bridge

The relation between change in resistance (δR) and bridge voltage (V_{bridge}) can be deducted from a simple voltage balance given in Eq. 2.9.

$$
\begin{aligned}
R_1 &= R + \delta R \\
R_2 &= R - \delta R \\
R_3 &= R + \delta R \\
R_4 &= R - \delta R \\
V_1 &= V_0 \frac{R2}{R3 + R2} \\
V_2 &= V_0 \frac{R1}{R1 + R4} \\
V_{bridge} &= V_1 - V_2 = \left(\frac{R2}{R3 + R2} - \frac{R1}{R1 + R4} \right) V_0 \\
V_{bridge} &= \left(\frac{R + \delta R}{2R} - \frac{R - \delta R}{2R} \right) = \frac{\delta R}{R} V_0
\end{aligned}
\tag{2.9}
$$

2.3.2 Simple considerations for an optimal Wheatstone Bridge

To compensate for zero offset, two adjustable resistance seen in Figure 2.6 are placed in the circuit. Bridge compensator fine (BCF) which compensates for smaller offsets has the internal resistance R_f. Bridge compensator coarse (BCC) compensates for larger offsets has the internal resistance R_c. These two compensators are used in connection, first BCC is used to zero the measured voltage then BCF is utilized to further compensate for smaller offsets till microVolt accu-

racy. Depending on the position of the resistance knob both R_c and R_f distribute the the total resistance between two arms denoted as $R_{c1} = c * Rc, R_{c2} = (1-c) * R_c$ and $R_{f1} = f * Rf, R_{f2} = (1-f) * R_f$ respectively (Fig. 2.6)

$$
\begin{aligned}
V_1 &= V_0 \frac{cR2(R1 + (1-c)R_c)}{(1-c)R1(R2 + cR_c) + cR2(R1 + (1-c)R_c)} \\
V_2 &= V_0 \frac{fR4(R3 + (1-f)R_f)}{(1-f)R3(R4 + fR_f) + fR4(R3 + (1-f)R_f)} \\
V_{bridge} &= V_1 - V_2
\end{aligned}
\tag{2.10}
$$

The change in resistance is connected to the change in voltage with Eq. 2.10 which is different then Eq. 2.9 as expected. To estimate the accuracy of the bridge, the sensitivity of fine and coarse compansators $\frac{\partial V_{bridge}}{\partial c}$ and $\frac{\partial V_{bridge}}{\partial f}$ are calculated. For $R_c = 30k\Omega$ and $R_f = 1M\Omega$ the bridge can be set to zero within 100 nV. $\frac{\partial V_{bridge}}{\partial c} = 2.9 \cdot 10^{-2} V$ and $\frac{\partial V_{bridge}}{\partial f} = 8.6 \cdot 10^{-5} V$

2.3.3 Modeling of cantilever bending

The bending of the cantilevers is modeled to connect the deflection to force measured and the piezo displacement to actual displacement of the sphere. One important thing to figure out is the what we measure is deflection of cantilevers which is proportional to vertical displacement of sphere but not equal. To calculate the displacement of the sphere, we can convert deflection to displacement if we know the relation exactly.

The static deflection of a cantilever with length L, width b and height h, is described by the linear fourth order homogeneous differential equation.

$$
\frac{\partial^4 u}{\partial x^4} = 0 \tag{2.11}
$$

where u(x) describes the bended shape of the cantilever. For our CFA setup the boundary conditions are given by:

$$u(0) = 0, u(L) = u_L, \left(\frac{\partial u}{\partial x}\right)_{x=0} = 0, \left(\frac{\partial u}{\partial x}\right)_{x=L} = 0 \tag{2.12}$$

Integrating the eq. 2.11 provides the deflection as a function of position on the cantilever.

$$u(x) = u_L(3(\frac{x}{L}))^2 - 2(\frac{x}{L})^3) \tag{2.13}$$

The local strain inside the cantilever is given by:

$$\epsilon(x, y) = y\frac{\partial^2 u}{\partial x^2} \tag{2.14}$$

Hence the stain at the surface of the cantilever, y=h/2, is given by

$$\epsilon_s(x) = \frac{3hu_L}{L^2}(1 - 2\frac{x}{l}) \tag{2.15}$$

The stress inside the cantilever can be related to the external force acting at the end of cantilever, via torque balance

$$F_l = -\frac{\partial M}{\partial x} = -\frac{\partial}{\partial x}\int_{-h/2}^{h/2} y\sigma(x, y)b\partial y \tag{2.16}$$

$$F_l = -\frac{\partial}{\partial x}EB\left(\frac{\partial^2 u}{\partial x^2}\right)\int_{-h/2}^{h/2} y^2\partial y \tag{2.17}$$

$$F_l = \frac{Ebh^3}{L^3}u_L \tag{2.18}$$

Bibliography

[1] M. Minsky. Memoir on Inventing the Confocal Scanning Microscope. *Scanning*, 10:128–138, 1988.

[2] A. van Blaaderen and P. Wiltzius. Real-Space Structure of Colloidal Hard-Sphere Glasses. *Science*, 270:1177–1179, November 1995.

[3] E. R. Weeks, J. C. Crocker, A. C. Levitt, A. Schofield, and D. A. Weitz. Three-Dimensional Direct Imaging of Structural Relaxation Near the Colloidal Glass Transition. *Science*, 287(5453):627–631, January 2000.

[4] M. E. Dailey, E. Manders, D. R. Soll, and M. Terasaki. Confocal microscopy of living cells. In James B. Pawley, editor, *Handbook of Biological Confocal Microscopy*, pages 381–403. Springer US, 2006.

[5] M. A. Dichtl and E. Sackmann. Microrheometry of semiflexible actin networks through enforced single-filament reptation: Frictional coupling and heterogeneities in entangled networks. *PNAS*, 99(10):6533–6538, 2002.

[6] E. R. Weeks and J. C. Crocker. Particle tracking using IDL: website. http://www.physics.emory.edu/weeks/idl/.

[7] A. Scherer and S. R. Quake. From micro- to nanofabrication with soft materials. *Science.*, 290(5496):1536, 2000.

[8] S. A. Vanapalli, D. Wijnperle, A. van den Berg, F. Mugele, and M. H. G Duits. Microfluidic valves with integrated structured elastomeric membranes for reversible fluidic entrapment and in situ channel functionalization. *Lab on a chip*, 10:1461–1467, 2009.

[9] A. Unger, M., H. Chou, T. Thorsen, A. Scherer, and S. R. Quake. Monolithic microfabricated valves and pumps by multilayer soft lithography. *Science.*, 288(113):5463, 2000.

[10] G. Lippmann. Relations entre les phénoménes électriques et capillaires. *Ann. Chim. Phys.*, 5(494), 1875.

[11] F. Mugele and J.C. Baret. Electrowetting: From basics to applications. *J. Phys.: Condens. Matter*, 17(28):705–744, 2005.

[12] P. García-Sánchez, A. Ramos, and F. Mugele. Electrothermally driven flows in ac electrowetting. *Phys. Rev. E*, 81(1):015303, Jan 2010.

[13] K. P. Nichols and J. G. E. Gardeniers. A digital microfluidic system for the investigation of pre-steady-state enzyme kinetics using rapid quenching with maldi-tof mass spectrometry. *Analytical Chemistry*, 79(22):8699–8704, 2007.

[14] S. H. Ko, H. Lee, and K. H. Kang. Hydrodynamic flows in electrowetting. *Langmuir*, 24(3):1094–1101, 2008.

[15] H. Lee, S. Yun, S. H. Ko, and K. H. Kang. An electrohydrodynamic flow in ac electrowetting. *Biomicrofluidics*, 3(4):044113, 2009.

3 Influence of confinement by smooth and rough walls in dense hard-sphere suspensions

Abstract We used video microscopy and particle tracking to study the dynamics of confined hard sphere suspensions. Suspensions were confined in a quasi-parallel geometry between two glass surfaces: a millimeter-sized rough sphere and a smooth flat wall. First, as the separation distance (H) is decreased from 18 to 1 particle diameters; a transition takes place from a sub-diffusive behavior (as in bulk) at large H, to completely caged particle dynamics at small H. These changes are accompanied by a strong decrease in the amplitude of the Mean Squared Displacement (MSD) in the horizontal plane parallel to the confining surfaces. In contrast, the global volume fraction essentially remains constant when H is decreased. Second, measuring the MSD as a function of distance from the confining walls, we found that the MSD is not spatially uniform but smaller close to the walls. This effect is the strongest near the smooth wall where layering takes place. Although confinement also induces local variations in volume fraction, the spatial variations in MSD can be attributed only partially to this effect. The changes in MSD are predominantly a direct effect of the confining surfaces. Hence both wall roughness and the separation distance (H) influence the dynamics in confined geometries.

3.1 Introduction

The dynamics of particles in confined colloidal suspensions is an intriguing topic that has raised a lot of attention recently. On one hand; it has been argued that experiments on spatially confined systems can reveal the dynamic length scales that occur in bulk suspensions [1, 2] or molecular systems [3]. On the other hand, the influence of confining walls on the mechanisms and timescales of structural rearrangements is also a topic in its own right [4]. Most fluids that have been studied are (near) Hard Sphere (HS) suspensions, motivated by their conceptual simplicity at the level of the particle pair interactions. Even for this system, the collective dynamic behavior can already be rather complex. Bulk HS dynamics has been studied extensively, both at the macroscopic level of the colloidal glass transition[5, 6] and at the microscopic level of particle motions [7, 8] . On increasing the HS volume fraction, a consistent slow down of the dynamics was found, which has manifested itself as an increase in correlation time [9] and a decrease of the diffusion coefficient [10, 11, 12] or mean squared displacement (MSD) [7, 8, 13]. However, understanding the mechanisms underlying this slower dynamics beyond qualitative notions can be difficult. From an intuitive point of view, it is clear that the local free volume should play an important role. If this volume is decreased then the motion of individual particles will become more restricted by the (transient) cages formed by the surrounding particles, and consequently the system will slow down. A description of this cage dynamics in terms of length- and time-scales was given by Weeks and Weitz [14]. However on approaching the colloidal glass transition, also more collective rearrange-ments have been reported, that cannot be covered by a simple cage concept [3, 13]. This illustrates that our understanding of collective dynamics is still incomplete, even for colloidal hard sphere fluids. Spatial confinement of a HS suspension will certainly interfere with the mechanisms for structural reorganizations. If dimensions of the fluid container are reduced to the length scales involved in the structural rearrangements as occur in bulk, then at least certain modes of large-scale reorganization will be disabled. For example, while small scale processes like the caging of individual particles may be sustained until the confinement

distance becomes only a few particle diameters, collective motions of e.g. hydrodynamic clusters will become impossible already at larger confinement distances. Generally the disabling of dynamic modes is expected to result in a slower dynamics, manifested for example as a decrease in MSD. Indeed, this trend has also been found in several experimental [1, 2] and simulation [15, 16, 17] studies. However a deeper insight into how the observed reduction in MSD comes about is still lacking. Several shortcomings can be pointed out:

1. The effects of the particle-wall interaction are still incompletely understood. The simplest case is that of hard spheres confined by hard walls: here only the roughness of the wall has to be considered. In several computer simulation studies, wall roughness has been found to strongly affect the local particle dynamics [4, 15, 16]. However in experiments [1] the permanent adhesion of a fraction of the particles to a smooth wall did not have a noticeable effect. In another experimental study [2], a layer of particles was deposited and subsequently sintered in order to roughen the wall. As far as we know, no other experimental studies exist that specifically address the effect of wall roughness on particle dynamics in confined fluids.

2. How the effects of the confining walls on the particle dynamics are transmitted from the walls into the suspension is also an unsettled issue. Depending on the restructuring mechanism, the particle dynamics could be collective or alternatively very local and dependent on the separations from the walls. From the literature it is not clear which cases to expect. In computer simulations on Lennard-Jones fluids, a confinement-induced glass transition was reported as a collective effect of all layers [3]. Another simulation study [16] reported 'a lack of evidence that the particle layer closest to the wall was decoupling dynamically from the rest'. However in simulations on HS confined by spherical cavities with smooth and rough walls, Nemeth and Lowen [18] found MSDs that depend strongly on the distance from the wall. For the smooth walls, the tangential MSDs were larger at the wall as compared to the interior, whereas for rough walls a different spatial dependence was found. Experiments on HS suspensions confined between two flat plates, performed by Nugent et al [1] showed yet again different trends: MSDs in planes parallel to the wall did not depend on the distance from the wall. If and how

these different findings could be reconciled is not clear at present, and hence a further study is warranted. 3. To what extent local variations in the MSD of confined fluids could be attributed to local differences in volume fraction is also unknown at present. The issue has been raised, but only addressed in a few studies. Mittal et al [19] studied this issue via computer simulations, and found that higher local densities in a confined HS fluid correlated with a faster local diffusion. This counterintuitive result was explained via the increased Widom insertion probability. Also experimental data that allow correlating between local MSD and local volume fraction are scarce. Dullens et al [20] studied HS suspensions at a single wall and found up to a volume fraction ϕ = 0.54, a continuous decrease in MSD. Sarangapani and Zhu [2] measured local volume fractions in two confined samples but did not aim for correlation with local MSDs. Nugent et al [1] measured MSDs and local densities, and found that one of the two particle species of their bidisperse system showed a concentration peak at the wall, but no change in the MSD parallel to the wall.

In this chapter, we shed light on the three mentioned issues via an experimental study on confined hard sphere suspensions, focusing our analysis on the MSDs measured with video particle tracking. A systematic study was performed into the effect of confining a colloidal fluid by two different walls (smooth and rough), on local particle dynamics. We found that progressive confinement caused a dramatic decrease of the MSD, without significant changes in the overall concentration. Local concentration variations within the confinement gap did occur however, and showed significant asymmetry when comparing the different walls. Also the MSDs were significantly different at the smooth and rough walls. These trends will be analyzed, from which it will be concluded that the roughness of the wall and the distances from the rough and smooth walls have a much stronger influence on MSD than the variations in local volume fraction.

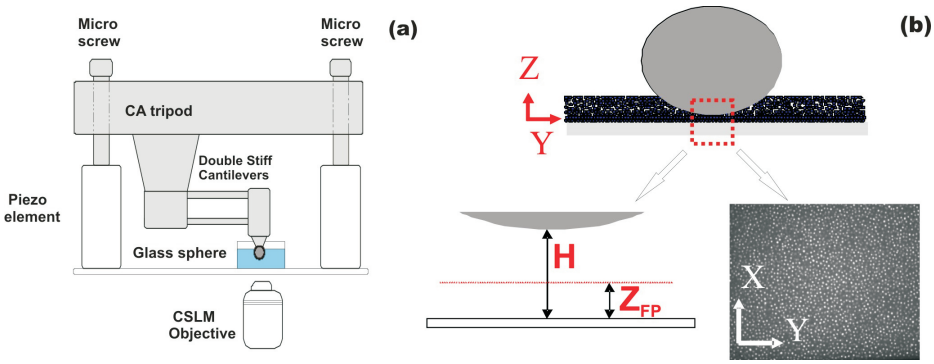

Figure 3.1: Panel (a) Schematic illustration of our confinement apparatus (CA). Colloidal fluid is confined between a glass plate and a sphere in a quasi-parallel geometry. The position of the sphere can be accurately controlled via the piezo stage on which the CA tripod is resting. Observations of the particles are made from below using a Confocal Scanning Laser Microscope (CSLM). Panel (b) Close up of the sphere-plane geometry with confinement gap (H) and height of the focal plane (Z_{FP}). Also a typical CSLM image of a confined fluid is shown (scale: 87 μm x 66 μm)

3.2 Experimental methods

3.2.1 Confinement apparatus

Our home-made Confinement Apparatus (CA) is sketched in Figure 3.1. Colloidal suspensions are confined between two glass surfaces (a sphere and cover slide). The sphere (D_{sphere} = 2 mm, Duke Scientific) is glued onto a holder, which is connected to the CA tripod via stiff double cantilevers. The tripod rests on a piezo stage via 3 micro screws. Coarse control over the gap height (H) is achieved via the screws, and guided by a visualization using fluorescent liquid. Fine control is achieved using a computer driven piezo stage (Physik Instrumente) with a vertical range of 20 μm, and an accuracy of 0.01 μm. In typical measurements, $D_{sphere} \ll H$, which means that an effective plane-plane geometry is obtained, independent of the precise alignment. Both confining surfaces were analyzed for topog-

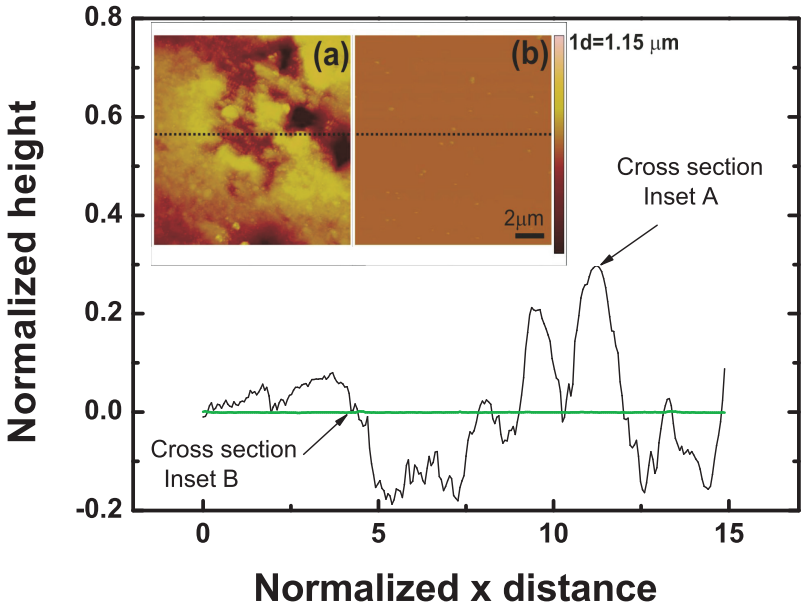

Figure 3.2: Representative cross sections of AFM topography analysis of the two confining surfaces. Axis ranges are scaled to the diameter of the colloidal particles (d). Inset (a) shows topography image of the rough glass sphere while inset (b) shows the smooth confining wall i.e. cover slip. The color bar of both insets shows the height, also scaled to d. The cross sections that were used to plot main graph are shown via dotted lines.

raphy with Atomic Force Microscopy (AFM). The results are shown in Fig. 3.2. The root mean square (rms) value of the height variations reveals that while the bottom surface is smooth (rms=10 nm), the surface of the glass sphere shows significant roughness (rms=0.13 μm).

3.2.2 Colloidal Fluid

Core-shell silica particles with outer diameter d=1.1 μm were synthesized following the method described in [21], which entails the deposition of non-fluorescent silica onto a fluorescent core. In our

case, the core contains rhodamine isothiocyanate (RITC) and had a diameter of ≈ 500 nm. Such core-shell particles allow for an accurate localization of particle centers from video microscopy images, even at high volume fractions. The polydispersity was assessed to be 8% from Scanning Electron Microscopy images (see Supplementary Information). To obtain (near) hard sphere suspensions, the solvent was changed to a refractive index matching mixture of H2O/DMSO [22] to minimize the Van der Waals attractions (and to optimize visualization, see Sec. 3.2.3), while LiCl was added to a final concentration of 0.01 M, to reduce the electrical double layer thickness to ≈ 7 nm.

Soft centrifugation (1000 g for 1 hr) was used to concentrate the fluid. This was done directly in the sample holder, which was made of an open cylindrical tube (diameter: 20 mm) glued onto a round glass cover slip. Sediments were prepared at volumes ranging in between 0.25-1.5 ml, at an initial volume fraction $\phi \approx 0.66$, in line with expectations for random close packing of a system with 8% polydispersity [23]. After removal of the supernatant the tube was weighed, and the amount of solvent needed to achieve the target ϕ was added. Then the sediment was resuspended using a whirl mixer. Samples were prepared at ϕ-values ranging from 0.15 to 0.57.

The precise volume fractions were ascertained a posteriori from the CSLM observations. Localizing all particles (see section 3.2.3) allowed to obtain ϕ values as follows: (X,Y,Z) control volumes (V) were defined as (65 μm x 65 μm x ΔZ) with either $\Delta Z = H$ (for the global volume fraction) or $\Delta Z << H$ (for local ϕ values). Then it was calculated for each particle (i), which fraction (f_i) of its volume fell within the control volume V, by using the relative location of the particle to the boundaries of V, and assuming d=1.12 μm. For V $\leq\leq \pi d^3/6$ this mostly corresponded to f_i = 1, but for small ΔZ mostly $0 \leq f_i \leq 1$. Then taking $N_{eff} = \sum N_i f_i$ as the effective number of particles, allowed to calculate ϕ as $N_{eff} \ll \pi d^3/6V$. In this way it was ensured that ϕ always represents a physical volume fraction, even for $\Delta Z \ll d$. Typical values were $N_{eff} \ll 1000$ (global ϕ) and $N_{eff} \approx 1000$ (local ϕ). In the case of local volume fractions it must be underlined that this is a strictly geometrical definition; hence it will be designated as ϕ_s from now on.

An accurate and consistent way to measure d, was to analyze a

CSLM image of a very dense layer on a cover slip with many particles touching each other. The average distance between touching particles was found to be 1.12 ± 0.03 μm, giving an estimated relative inaccuracy in the volume fraction of 8%. Also the magnitude of H was measured more accurately, making use of the CSLM recordings. The location of the bottom surface was defined as 0.5*d below the measured average Z position of all particle centers in the lowest layer. The top surface was localized by extrapolating the steep flank of the concentration profile to zero (see Fig. 3.6) and adding 0.5*d. Considering the particle polydispersity and the rms roughness of the top surface, we estimate the inaccuracy of H to be 0.2-0.3 μm.

In the presence of confining surfaces, concentrated suspensions may change their structure and dynamics. However the time that is needed for such changes is not known a priori, and may depend on the volume fraction. For this reason, we studied confined systems at $\phi = 0.33 - 0.42$, i.e. well below the glass transition point for hard spheres at $\phi = 0.58$ [5]. Moreover we also examined the influence of the waiting time after the fluid had been confined to a new gap height. Here it turned out that waiting 4 hours instead of the (standard) 1 hour, gave similar results. Furthermore, we checked whether the colloidal fluid crystallized at time scales comparable to the duration of our experiment. No evidence of crystallization was found, in accordance with the 8% polydispersity and a previous study [24].

3.2.3 Confocal microscopy and Particle tracking

The Confocal Scanning Laser Microscope (CSLM) was an UltraView LCI10 system, Perkin-Elmer) containing a Nikon Eclipse inverted microscope equipped with a Nipkow disk (Yokogawa module) and 100X NA 1.3/oil objective. When tracking particle dynamics, we imaged horizontal (X,Y) focal planes for 240 s at a rate of 10 frames/s. For measuring particle locations in three dimensions (3D) we measured series of images along the Z-direction (up to 30 μm from the bottom, taking ≈ 60 s) at 0.1 μm/step. The images were processed via the available particle tracking codes in 2D and 3D [25]. The accuracy of locating the centroid of particles in 3D was 0.02 μ m in X-Y and 0.05 μm in Z direction. The Z-resolution of our 2D particle tracking

was measured to be ≈ 0.8 μm (full width half maximum), by localizing (almost stationary) particles in a 3D volume and subsequently analyzing per focal plane, up to which distance from the focal plane particles were still accepted by the 2D particle tracking code (using typical selection criteria for brightness, object size etc.).

Image-time series aimed at studying particle dynamics typically consisted of 2500 time steps. After localizing all particles in each frame and building trajectories, mean squared displacements (MSDs) in the horizontal plane were calculated, using:

$$\langle r^2(\tau)\rangle = \left\langle [x(t+\tau) - x(t)]^2 + [y(t+\tau) - y(t)]^2 \right\rangle \tag{3.1}$$

where x(t) is the X-position of a particle at real time t, τ is the lag time, the {} brackets indicate an averaging over all times t and the $\langle\rangle$ brackets indicate an averaging over all particles. In the calculation of x(t) and y(t) a correction for mechanical drift was applied by subtracting the measured average displacement of the ensemble of particles. The typical accuracy in the MSD was $1.0 * 10^{-4}$ μm^2. In the following, MSDs will be fitted as

$$\langle r^2(\tau)\rangle = A\left(\frac{\tau}{\tau_0}\right)^{\alpha} \tag{3.2}$$

with A as the amplitude, τ_0 as the shortest exposure time and α as the exponent indicating the behavior of Brownian motion (α=1 diffusive, $\alpha \leq 1$ subdiffusive).The fitting range for α was taken from 0.1 to 10 s.

3.3 Results

3.3.1 Particle dynamics in bulk fluids

As a reference, we present in Fig. 3.3 a series of MSD curves measured for the bulk suspensions at different volume fractions ϕ= 0.16-0.57. To ensure that the measurements pertained to the dynamic behavior in bulk, observations were done at Z_{FP} = 30 μm, which will be shown to be sufficiently far away from the wall. As ϕ is increased both

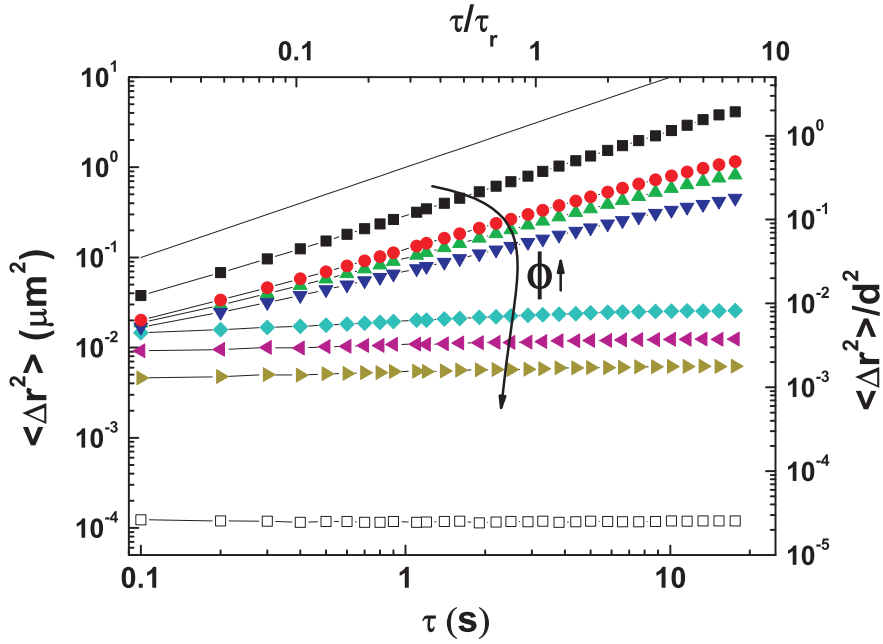

Figure 3.3: MSD vs. time lag for bulk samples at different volume fractions. Lower abscissa and left ordinate: lag time (s) and mean squared displacement (μm^2). Upper abscissa and right ordinate: normalized data, where $\langle \Delta\, r^2(\tau) \rangle$ was divided by d^2 = 1.32 μm^2 and τ by the Brownian time (τ_r) where $\tau_r = d^2/4D_0$ equals 3.54 s. The symbols indicate volume fractions (ϕ) of 0.16 (■), 0.26 (●), 0.37(▲), 0.42(▼), 0.52(⋄), 0.54(◀) and 0.57(▶). The square symbols (□) indicate the noise floor.

the amplitude A and the exponent α of $\langle \Delta r^2(\tau) \rangle$ (see Eq.3.2) become smaller. The exponent (α) is observed to change from almost 1.0 (as for a viscous liquid) to approximately 0.0 (as for a solid). The occurrence of a plateau for $\phi \geq 0.52$ suggests a solid-like microscopic dynamics already starting at this volume fraction, whereas the macroscopic glass transition for colloidal HS is supposed to occur at ϕ=0.58 [5]. These results are qualitatively in agreement with other studies, and will be further analyzed in Sec. 3.4.1.

3.3.2 Particle dynamics in confined fluids

The effect of confinement on the MSD was examined for bulk volume fractions of 0.33, 0.38 and 0.42, in the range where the bulk fluid still showed liquid-like behavior. For all three volume fractions the trends were similar; results will be presented for the system at ϕ=0.33, unless mentioned otherwise. Fig. 3.4a shows the MSDs taken in the mid-plane of the gap (Z_{FP} =$H/2$) between plate and sphere. On decreasing H from 20 μm to 1 particle diameter, strong changes in the MSD curve are observed: a reduction in amplitude as well as a decrease in the exponent, eventually reaching 0. These changes are qualitatively similar to the effects of increasing the volume fraction in bulk systems, and that eventually led the system into the glass state (Fig. 3). Same trend is observed for Fig. 4b where the MSDs at a fixed distance (2 μm) away from the rough and smooth walls are monitored.

A systematic study was performed, covering MSDs as a function of distance from walls. It then turned out that the MSDs of our confined fluids are not constant over the gap. This is demonstrated by the comparison of Fig. 3.4a, which shows the MSDs measured at the mid-plane, with Fig. 3.4b in which the MSDs measured at Z_{FP} = 2 μm and Z_{FP} = H – 2 μm are plotted. Clearly, near the surfaces the MSDs are different than at the mid-plane. It is also evident from Fig. 3.4b that near the smooth bottom plate, the MSDs are consistently lower than at the rough surface of the top sphere. This difference will be further discussed in Sec. 3.4.2.

We examine the MSD(H,Z_{FP},τ) function in more detail by plotting the magnitude of $\langle \Delta\, r^2(\tau) \rangle$ evaluated at a lag time τ=10 s, for many (H, Z_{FP}) combinations. At this lag time, the differences between the MSDs are more pronounced than at shorter times, while the typical errors found at long times (due to poor statistics and gradients in drift [26]) are still small.

The solid symbols in Fig. 3.5 show the spatially resolved MSDs for the same gap heights as in Fig. 3.4a (including an additional experiment for which $H \to \infty$). It is observed that the MSDs show a maximum in between the two confining surfaces. This maximum is not in the middle of the gap but closer to the surface of the top sphere.

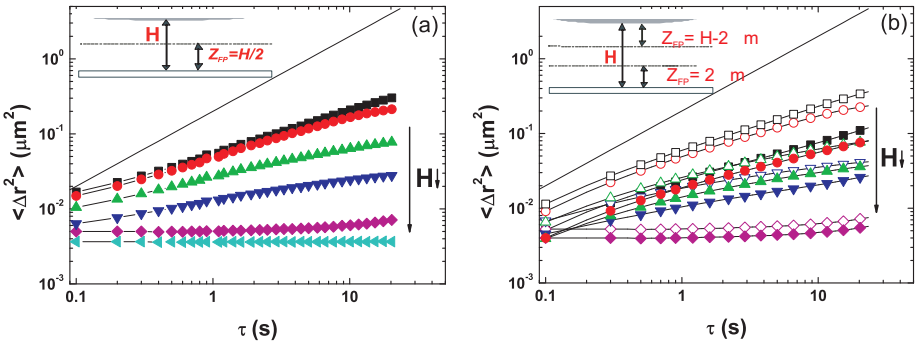

Figure 3.4: Mean square displacement (MSD) vs. time lag plot for decreasing confinement gap (H). In panel a, each curve indicates the MSD at the midplane $Z_{FP} = H/2$ (see Fig. 1). Correspondence between H (μm) and symbols: 20 μm(■), 16 μm(•), 12 μm(▲), 8 μm(▼), 4 μm(◇) and ≈1.3 μm (◀). Panel b: MSD vs. time lag for different gap heights H, now for planes 2 μm away from the confining walls. Open and closed symbols correspond to rough (top) and smooth (bottom) walls, respectively. Volume fraction (ϕ) of the sample is 0.33. Qualitatively similar behavior was observed for samples at ϕ=0.38, 0.42.

It is also noted that the Z_{FP}-dependence of the MSD is gradual. Although the MSDs become rather small due to the confinement, they all remain well above the noise-floor, indicating that the particles are still rearranging themselves. This finding is corroborated by our trajectory analysis (not shown), in which all particles still show motion. Hence we found no evidence that particles had permanently stuck to any surface.

Considering the possibility of layer formation at walls, and the clear dependence of the MSD on the concentration in bulk HS systems (Fig. 3.3 and 3.7), the question arises to what extent the variations in MSD could be attributed to local volume fraction effects.

The main graph of Fig. 3.6 shows the geometrical local volume fraction profile $\phi_s(Z)$, calculated as explained in Sec. 3.2.2. Clearly, the profiles are strongly peaked near the bottom wall. The peaks are approximately equally spaced (distance $\Delta\ Z_{pp} \approx 1.14\ \mu m$) and their amplitude becomes progressively smaller as the distance from

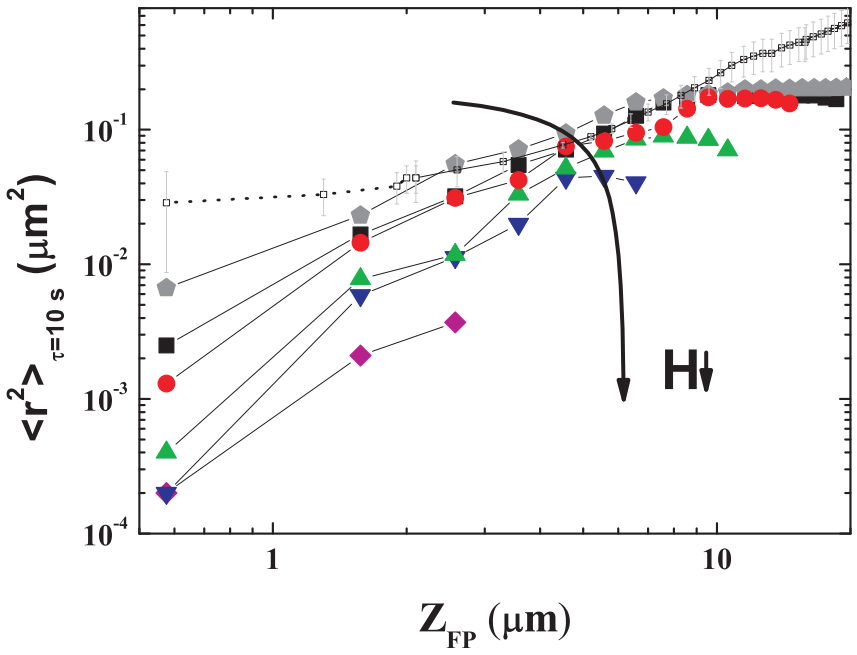

Figure 3.5: Spatially resolved behavior of $MSD_{\tau=10s}$ for the fluid at ϕ=0.33, confined at different gap heights H. Correspondence between H (μm) and symbols: 20 (■), 16(•), 12(▲), 8(▼) and 4(⋄). The pentagram symbol belongs to the experiment where the second confining surface is far away ($H \to \infty$). Corresponding open symbols indicate "bulk" MSD values calculated from the local volume fraction showing what $MSD_{\tau=10s}$ would be if the system was bulk and dynamics were solely governed by volume fraction. The open symbols have been calculated from the linear fit to a characteristic curve in the inset of Figure 3.6. The error bars has been calculated from different fits to inset of Figure 3.6. The dotted part of open symbols indicates extrapolation. See text for further details)

the wall is increased. This is similar to the behavior that was found in previous studies on layering of HS suspensions [27, 28]. In our case the depth of the first minimum is remarkably low, corresponding to a very low occurrence of sphere centers (as was checked from the 3D localization data). Furthermore, the first peak to peak distance is slightly larger; we offer no tentative explanation for this.

Confinement by the second surface causes only little changes in the ϕ(Z) profile near the bottom surface; the strongly peaked structure remains and also the ϕ values super-impose fairly well. The overall volume fraction shows a small decrease upon confining the fluid from $H \to \infty$. to $H = 20\ \mu m$, but upon progressive confinement it shows less than 5% relative variation. Also the concentration profile under the top sphere can now be studied. Although some layering occurs, the peaks are by far less pronounced than at the bottom surface. Again this points at an important difference between the top and bottom surfaces, which will be discussed in Sec. 3.4.2.

We return to the question whether the variations in MSD could be due to the variations in local volume fraction only. We examine this by measuring the relation between the local ϕ and the local MSD, and subsequently comparing each local MSD magnitude with the value that it would have in a bulk system at the local ϕ. A question that then arises is down to which length scale a calculated local ϕ would still be meaningful. Since the MSD of a particle should at least depend on the cage defined by its direct neighbors, the use of ϕ-values calculated at smaller length scales than this cage length would not make sense (the precise length scale at which local ϕ does matter still has to be assessed for confined systems). To take this aspect into account and sample the ϕ(Z) profile at a more appropriate length scale, we convoluted the Z-histogram of particle center locations with a block profile of width $\Delta Z_{pp} \approx$ d. Subsequently we applied an additional convolution with a Gaussian kernel with 0.8 μm FWHM, to account for the optical Z-resolution of the MSD measurement (see Sec. 3.2.3). These operations produce the ϕ(Z) profiles shown in the inset of Fig. 3.6. Looking up the ϕ values from this profile and interpolating against the MSD(ϕ) relation for bulk samples then produces the densely dotted MSD(Z) data shown in Fig. 3.6. Since slightly different convolutions and interpolations would have

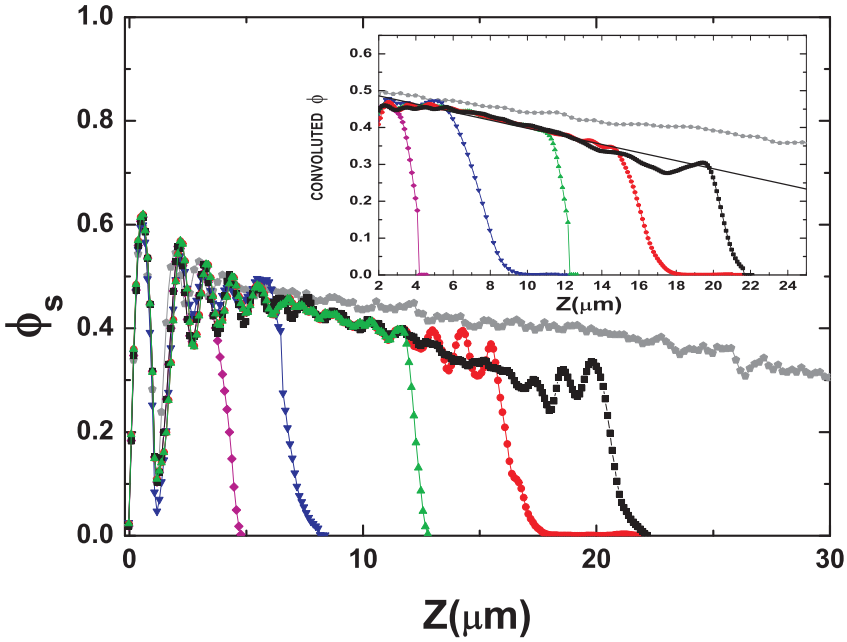

Figure 3.6: Geometric volume fraction (ϕ) vs Z for different confinement gaps: Correspondence between $H\,(\mu m)$ and symbols: 20 (■), 16(•), 12(▲), 8(▼) and 4(⋄). The pentagram symbol belongs to the experiment where the second confining surface is far away ($H \to \infty$). ϕ indicates local volume fraction calculated in a bin. Inset: Convoluted volume fraction (ϕ) vs. Z-histogram, as needed for generating reference $MSD_{\tau=10s}$ data at in Fig. 3.5. Solid line is linear interpolation to convoluted volume profile used to calculate expected MSD values in Figure 3.5. See text for further details.)

been possible, we represent the effect thereof on the MSD values by error bars. Now comparing the interpolated MSD curves to the measured data, it becomes clear that the data interpolated from the MSD(ϕ) relation strongly over-estimate the MSDs of the confined systems, and the more so as H gets smaller. This demonstrates that the dramatic decrease in MSD near the surface(s) can only for a very small part be attributed to variations in local volume fraction.

Confinement experiments were done at several volume fractions

(ϕ = 0.33, 0.38, 0.42), but so far only the results at ϕ = 0.33 were shown. Importantly, for all three samples a similar behavior was found when the gap height was reduced from (effectively) infinite to just a few particle diameters. To illustrate this, we plotted MSD data at τ = 10s, for both bulk and confined fluids in Fig. 3.7. For all three confined fluids, the local volume fraction changes only little with confinement, and dramatic reductions in MSD compared to the bulk are found. At the smallest gaps, it seems that the volume fraction differences even do not matter anymore. This strong dependence of the MSD on H as compared to the dependence on ϕ, is also illustrated in the inset of Fig. 3.7. This underlines once more that the reductions in MSD are largely due to confinement, rather than due to the local volume fraction.

3.4 Discussion

3.4.1 Comparison with Hard Sphere systems

Besides using the MSDs in Fig. 3.3 for comparison between bulk and confined fluids, it is also interesting to examine if they show the behavior as expected for Hard Spheres. From the curve at ϕ=0.16 an apparent viscosity of 6.0 mPa.s was extracted using the Stokes-Einstein equation; this gives a relative viscosity of 1.47 which is fairly close to ≈ 1.6 as expected for HS [28, 27]. However the calculation of a viscosity from MSD data using the Generalized Stokes Einstein Relation [29, 30] is not trivial for non-dilute HS suspensions. Alternatively also the normalized diffusion coefficient D/D_0, with D_0 the diffusion coefficient for $\phi \to 0$, can be compared to literature. For $\phi \approx 0.16$, Ottewill and Williams [31] found a normalized self diffusion coefficient of ≈ 0.72 at short times and ≈ 0.44 at long times. This suggests that our data at ϕ=0.16 (where D/D_0 = 0.68) show the short-time self diffusion. The sub-diffusive behaviors (0< α <1) at higher volume fractions then show intermediate regimes between short- and long-time self-diffusion.

Also direct comparisons with MSDs of other HS systems are possible. Kasper et al[24]studied cross-linked poly-t-butylacrylate parti-

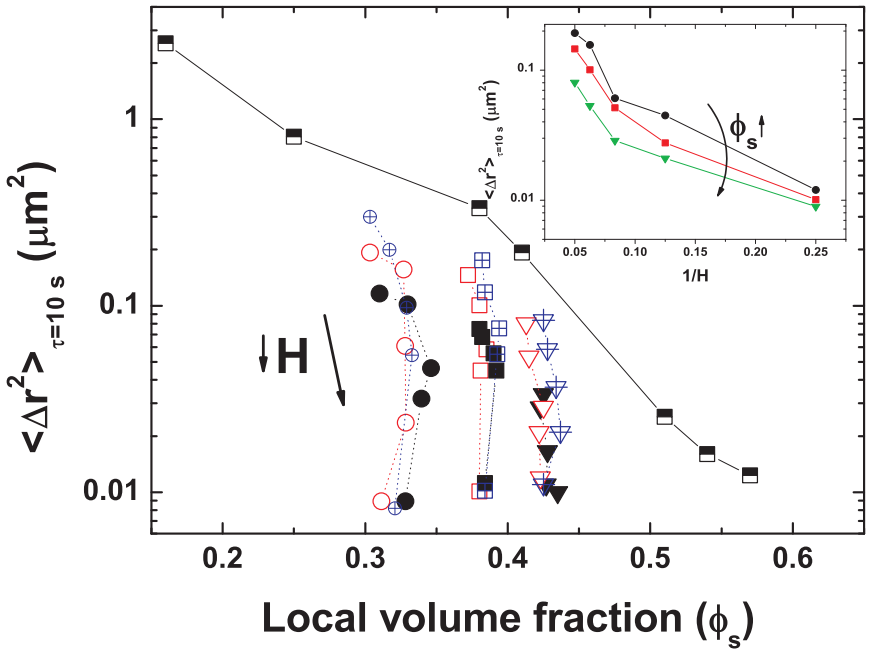

Figure 3.7: MSDτ=10 s vs. local volume fraction. Half full squares indicate bulk measurements; all other symbols refer to confinement. Open red: Z_{FP} = $H/2$, solid black: Z_{FP} = 2 μm, crossed blue: Z_{FP} = $H-2$ μm. Symbol shapes indicate the initial volume fraction: ϕ=0.33 (•), 0.38(■), 0.42(▼). H varies between 20 and 4 μm for this graph. Inset: same MSD data at Z_{FP} = $H/2$ plotted vs. $\frac{1}{H}$.

cles (d=910 nm) in 4-fluorotoluene at $Z_{FP} \approx 10$ μm (or 11 particle diameters) for ϕ= 0.32-0.60. They also observe a transition from an almost diffusive behavior (at ϕ= 0.32) to a plateau (at ϕ= 0.60), with sub diffusive behaviors (0< α < 1) in between. After normalizing MSDs as $(\Delta r)/d^2$ and τ^*4D_0/d2, which should result in a master curve for hard spheres, their data can be compared to ours. It then turns out that while the pattern of MSD curves matches well between the two systems, the volume fractions of the superimposing curves do not correspond well (see supplementary information).

Reference data are also available for systems of poly(hydroxystearic acid) (PHS) coated spheres suspended in tetralin/decalin/carbon tetra-

chloride [8], cycloheptylbromide /decalin [7] and cyclohexylbromide/decalin [1, 2]. However these studies address normalized times that are much longer, and in a range that gives only a small overlap with our data (see supplementary information). Also at these longer timescales, the normalized MSD curves of the various systems do not show the overlap expected for ideal hard spheres.

Comparison with literature for (near) HS systems thus leads to two conclusions: 1) the dynamics of our bulk silica suspensions qualitatively resembles that of other (near) Hard Sphere fluids, and 2) the MSDs of several (near) HS systems do not all collapse onto the expected master curve. This suggests that the particle dynamics in near-HS fluids is rather sensitive to small deviations from ideal HS behavior, and underlines the value of MSD measurements in bulk, as a reference for analyzing the dynamics under confinement.

3.4.2 Asymmetry between the two confining surfaces

From the AFM topography images (Fig. 3.2) it was clear that whereas the coverslip was very smooth, the surface roughness of the glass sphere was certainly not negligible when compared to the size of the silica particles. The layering that we found at the smooth wall and the almost complete absence thereof at the rough wall (Fig. 3.6) are also in good agreement with expectations for ordering phenomena at smooth and rough walls: in several previous studies (e.g. [16, 17]) such behavior has been found. Taking these observations together with the strong effects of wall roughness on local particle dynamics as found in computer simulations [4, 16, 17], it seems rather likely that the different MSDs found at the two glass surfaces are to be attributed to the differences in wall roughness.

However since the mass density of our particles exceeds that of the solvent by ≈ 800 kg/m3, it cannot be excluded a priori that also gravity could affect the particle dynamics (and hence contribute to the asymmetry between top and bottom surfaces). An estimation of the importance of gravity can be made by comparing the buoyancy force on a single particle to the thermal force kT/a (with a the particle

radius). Expressed as a Peclet number $Pe = \Delta\rho g a^4/kT$ [32, 33] we obtain Pe=0.2. This suggests that the thermal forces are stronger, but also indicates that the effect of gravity should not be completely ignored. Another way of assessing the importance of gravity is to look at the ϕ(Z) profiles for Z≥10 μm. While the data in Fig. 3.6 indeed show a decreasing trend, taking this effect of gravity on ϕ into account as in Fig. 3.6 (open symbols), it came out that a substantial part of the reduction in MSD at the bottom wall (compared to the bulk) cannot be attributed to the volume fraction change. This corroborates once more that the surface effects dominate.

The availability of different wall surfaces (in contact with the same fluid) together with the ability to control H, make it interesting to compare the effects of the single walls and the confinement distance on the MSD. This is illustrated in Fig. 3.8, which presents the same data as in Fig. 3.5, but now as a function of the normalized distance from both walls. Also the magnitude of the bulk MSD at ϕ=0.33 (obtained by interpolation) is included. The data at H = 20 μm show a large MSD plateau with a magnitude close to that of the bulk system. This means that the effects of the separate walls (i.e. without the influence of a second surface) can be estimated from the difference between the solid and dashed black lines. Clearly, for the smooth wall the reduction in MSD is appreciable and extends over long distance, whereas for the rough wall the effect is small and short- ranged. Fig. 3.8 also makes clear that both a smooth wall and confinement can cause a major reduction in MSD, and moreover that layering and confinement can also work together: even very close to the smooth surface, where the MSD was already reduced by two orders of magnitude due to the layering, the confinement is able to further reduce the MSD by more than an order of magnitude. For the rough wall, it is illustrated that the wall effects become negligible compared to the confinement effects, already at relatively large H. This corroborates the approach taken in reference [1] where the wall was roughened in order to mitigate layering effects. The implication of these findings for practical cases (such as channels in a microfluidic chip, or pore channels) is that the overall dynamics in the cavity could be controlled by engineering the roughness of the walls.

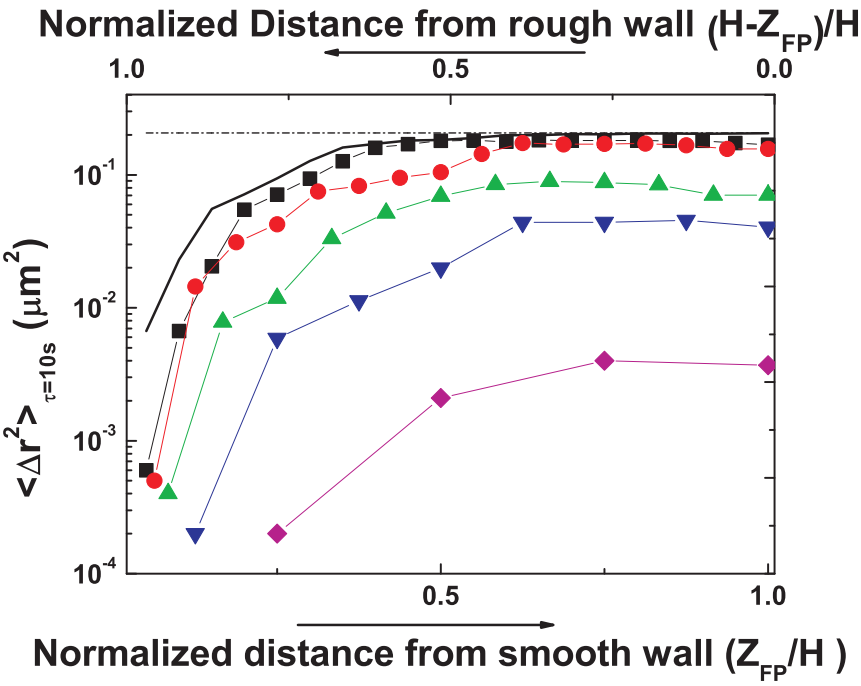

Figure 3.8: Alternative representation of the data in Fig. 3.5, to reveal the contributions of layering and confinement on the MSD at τ=10 s. The dashed line indicates the MSD of the bulk fluid (at ϕ=0.33) whereas the solid black line belongs to the layered system (i.e. in absence of the top surface).Correspondence between H (μm) and symbols: 20 (■), 16(•), 12(▲), 8(▼) and 4(⋄)

3.5 Conclusions

We investigated the dynamics of dense hard sphere suspensions under confinement between a smooth and a rough surface. Upon decreasing the gap height H, the overall particle dynamics was found to slow down dramatically, in accordance with previous studies. Systematic experiments allowed us to conclude that this slow down is predominantly a direct effect of confinement, and the confinement-induced variations in particle density play s role in the dynamics within the gap. Within the gap, local differences in the dynamics were found.

Local MSD minima occurring at the walls indicated that besides the confinement effect also wall effects can contribute to the dynamics. In the case of a smooth wall, interplay between the effects of layering and confinement occurs.

Our finding that volume fraction alone cannot explain the variations in MSD for layered or confined systems, confirms that studies of mechanistic details will be needed to achieve a deeper understanding. Finally we also remark that the dynamics of confined (near) HS suspensions appears to be sensitive to details of the interparticle and the particle-wall interactions. Choosing very similar materials for the particles and walls could help to better define the systems. Also more systematic experiments regarding wall roughness should be performed.

3.6 Acknowledgments

H.B.Eral would like to thank Michiel Hermes for fruitful discussions, Sissi de Beer for AFM analysis, Klaas Smit for mechanical assistance and Mariska van der Weide-Grevelink and Cor Harteveld for technical support. Eric Weeks is acknowledged for providing particle tracking software. We thank the Chemical Sciences division of the Netherlands Organization for Scientific Research (NWO-CW) for financial support (ECHO grant).

Bibliography

[1] C. R. Nugent, K. V. Edmond, H. N. Patel, and E. R. Weeks. Colloidal glass transition observed in confinement. *Phys. Rev. Lett.*, 99(2), 2007.

[2] P. S. Sarangapani and Y. Zhu. Impeded structural relaxation of a hard-sphere colloidal suspension under confinement. *Phys. Rev. E*, 77(1), 2008.

[3] M. Alcoutlabi and G. B. McKenna. Effects of confinement on material behaviour at the nanometre size scale. *J. Phys.: Cond. Matt.*, 17(15):R461–R524, 2005.

[4] T. Fehr and H. Löwen. Glass transition in confined geometry. *Phys. Rev. E*, 52(4):4016–4025, 1995.

[5] P.N. Pusey and W. van Megen. Phase behaviour of concentrated suspensions of nearly hard colloidal spheres. *Nature*, 320(27):340–342, 1986.

[6] P. N. Pusey and W. van Megen. Observation of a glass transition in suspensions of spherical colloidal particles. *Phys. Rev. Lett.*, 59(18):2083–2086, Nov 1987.

[7] E. R. Weeks, J. C. Crocker, A. C. Levitt, A. Schofield, and D. A. Weitz. Three-Dimensional Direct Imaging of Structural Relaxation Near the Colloidal Glass Transition. *Science*, 287(5453):627–631, 2000.

[8] W. K. Kegel and van Blaaderen Alfons. Direct Observation of Dynamical Heterogeneities in Colloidal Hard-Sphere Suspensions. *Science*, 287(5451):290–293, 2000.

[9] W. van Megen, S. M. Underwood, and P. N. Pusey. Nonergodicity parameters of colloidal glasses. *Phys. Rev. Lett.*, 67(12):1586–1589, Sep 1991.

[10] A. Vanveluwen. Measurement of the short-time self-diffusion coefficient in dilute and concentrated suspensions: Influence of direct particle interactions. *J. Chem. Phys.*, 87(12):4873, 1987.

[11] A. J. Banchio and G. Nagele. Viscoelasticity and generalized stokes–einstein relations of colloidal dispersions. *J. Chem. Phys.*, 128(10):104903, 2008.

[12] A. Sierou and J. F. Brady. Accelerated stokesian dynamics simulations. *J.Fluid Mech.*, 448(10):115–146, 2001.

[13] E. R. Weeks and D. A. Weitz. Properties of cage rearrangements observed near the colloidal glass transition. *Phys. Rev. Lett.*, 89(9):095704, 2002.

[14] E. R. Weeks and D. A. Weitz. Subdiffusion and the cage effect studied near the colloidal glass transition. *Chem. Phys.*, 284(1-2):361 – 367, 2002.

[15] P. Scheidler, W. Kob, and K. Binder. The relaxation dynamics of a simple glass former confined in a pore. *EPL*, 52(3):0295–5075, 2000.

[16] P. Scheidler, W. Kob, and K. Binder. Cooperative motion and growing length scales in supercooled confined liquids. *EPL*, 59(5):701–707, 2002.

[17] P. A. Thompson, G. S. Grest, and M. O. Robbins. Phase transitions and universal dynamics in confined films. *Phys. Rev. Lett.*, 68(23):3448–3451, 1992.

[18] Z. T. Németh and H. Löwen. Freezing and glass transition of hard spheres in cavities. *Phys. Rev. E*, 59(6):6824–6829, 1999.

[19] J. Mittal, T. M. Truskett, J. R. Errington, and G. Hummer. Layering and position-dependent diffusive dynamics of confined fluids. *Phys. Rev. Lett.*, 100(14):145901, 2008.

[20] R. P. A. Dullens and W. K. Kegel. Topological lifetimes of polydisperse colloidal hard spheres at a wall. *Phys. Rev. E*, 71(1):011405, 2005.

[21] N. A. M. Verhaegh and A. van Blaaderen. Dispersions of rhodamine-labeled silica spheres: Synthesis, characterization,

and fluorescence confocal scanning laser microscopy. *Langmuir*, 10(5):1427–1438, 1994.

[22] V. I. Uricanu and M. H. G. Duits. Micromechanical behavior of adhesive granular silica layers. *Langmuir*, 22(18):7783–7792, 2006.

[23] W. Schaertl and H. Sillescu. Brownian dynamics of polydisperse colloidal hard spheres: Equilibrium structures and random close packings. *J. Stat. Phys.*, 77(5):1007–1025, 1994.

[24] A. Kasper, E. Bartsch, and H. Sillescu. Self-diffusion in concentrated colloid suspensions studied by digital video microscopy of coreâ^'shell tracer particles. *Langmuir*, 14(18):5004–5010, 1998.

[25] J. C. Crocker and D. G. Grier. Methods of digital video microscopy for colloidal studies. *J. of Coll. and Int. Sci.*, 179(2):298–310, 1996.

[26] T. Savin, P. T. Spicer, and P. S. Doyle. A rational approach to noise discrimination in video microscopy particle tracking. *Appl. Phys. Lett.*, 93(2), 2008.

[27] J. C. van der Werff and C. G. de Kruif. Hard-sphere colloidal dispersions: the scaling of rheological properties with particle size, volume fraction, and shear rate. *J.Rheo.*, 33(3):421–454, 1989.

[28] S. Phan, W. B. Russel, Z. Cheng, J. Zhu, P. M. Chaikin, J. H. Dunsmuir, and R. H. Ottewill. Phase transition, equation of state, and limiting shear viscosities of hard sphere dispersions. *Phys. Rev. E*, 54(6):6633–6645, 1996.

[29] T. Mason. Estimating the viscoelastic moduli of complex fluids using the generalized stokes–einstein equation. *Rheologica Acta*, 39:371–378, 2000.

[30] T. A. Waigh. Microrheology of complex fluids. *Reports on Progress in Physics*, 68(3):685, 2005.

[31] R. H. Ottewill and N. St. J. Williams. Study of particle motion in concentrated dispersions by tracer diffusion. *Nature*, 325(6101):232, 1989.

[32] J. P. Hoogenboom, P. Vergeer, and A. van Blaaderen. A real-space analysis of colloidal crystallization in a gravitational field at a flat bottom wall. *J. Chem. Phys.*, 119(6):3371–3383, 2003.

[33] K. E. Davis, W. B. Russel, and W. J. Glantschnig. Disorder-to-Order Transition in Settling Suspensions of Colloidal Silica: X-ray Measurements. *Science*, 245(4917):507–510, 1989.

4 Anisotropic and hindered diffusion of colloids in a cylinder

Abstract Video microscopy and particle tracking were used to measure the spatial dependence of the diffusion coefficient (D_α) of colloidal particles in a closed cylindrical cavity. Both height and radius of the cylinder were equal to 9.0 particle diameters. The number of trapped particles was varied between 1 and 16, which produced similar results. In the center of the cavity, D_α turned out to be 0.75 times D_0 measured in bulk liquid. On approaching the cylindrical wall, a transition region of about 3 particle diameters wide was found, in which the radial and azimuthal components of D_α decrease to respective values of 0.1 and 0.4 times D_0, indicating asymmetric diffusion. Hydrodynamic simulations of local drag coefficients for hard spheres produced very good agreement with experimental results. These findings indicate that the hydrodynamic particle-wall interactions are dominant, and that the complete 3D geometry of the confinement needs to be taken into account to accurately predict the spatial dependence of diffusion.

4.1 Introduction

Understanding how confinement affects the diffusive behavior of colloidal particles is crucial for understanding various dynamic processes in biological and microfluidic systems [1, 2, 3]. A first class of examples is given by particles that have to diffuse towards a flat wall before they become immobilized as needed e.g. for coating applications or for biomedical diagnostics in microfluidic chips [4, 5]. Here diffusive processes under confinement have been found to have a direct influence on measurable quantities such as reaction rates and retardation times [6, 7] . Also confinement of particles in more than one dimension and/or involving wall curvature occurs; examples are the synthesis of colloids inside droplets [7], trapping of particles inside pores [8, 9] and the diffusion or directed transport of biomolecules or particles inside biological cells (or model systems for these golding [10, 11]). For each of these cases, understanding the time dependent particle dynamics is tightly connected to the question how the confinement influences the diffusion [12]. Surprisingly, the majority of fundamental studies referring to this problem have been limited to simple geometries such as a particle approaching a flat wall, or quasi two-dimensional systems [13, 14, 15, 16]. Theoretically, the classical problem of a particle translating in the vicinity of a rigid flat wall was first treated in 1907 by Lorentz [17], then Faxen [18, 19] later improved by Brenner [20] in 1961 and extended to the double wall case by Goldman [21]. drag force along the axis of cylinders was studied theoretically by Sano [22]. For some geometries, the quantitative correspondence between differently obtained analytical expressions is still an issue, as evidenced by recent papers on methods to improve the analytical solution [22, 23, 24] . Experimentally, single wall and double wall cases have been studied with optical tweezers [25, 26], microscopy [14], total internal reflection velocimetry [27] and light scattering [27, 28]. Although each of these techniques has their own challenges, the results of these studies coincided reasonably well with each other and with the theoretical expressions. Cylindrical geometries were also studied in a few (quasi-one-dimensional) cases: macroscopic measurements of the drag coefficient for a mm-sized sphere settling along the axis of a closed 3D cylinder [29, 30] and micro-

scopic measurements of diffusion along of the axis of long cylindrical microchannels [31, 32].

From this short overview, it is clear that both theoretical and experimental studies which extend beyond simple confining geometries are scarce. From the experimental side this could perhaps be explained by the challenges in measuring local diffusion coefficients (or alternatively drag forces) in 3D confinements and in manufacturing suitable confining structures. However, recent developments in soft lithography [33, 34] have provided new opportunities for the latter. Three dimensional (3D) micron scale confining geometries can now be manufactured in a variety of materials [35]. Moreover, these geometries can be also integrated into microfluidic systems in which liquid flow is controlled via pumps and valves [35]. These new capabilities offer unique opportunities for studying diffusion in 3D confinement because of the flexibility in the design of the confining geometry, the active control over liquid flow and the good optical access to the confined volume.

In this chapter, we study the spatial dependence of the diffusion coefficient in 3D closed cylinder geometry experimentally and compare our results with numerical simulations. Combination of soft lithography and real-time Confocal Scanning Laser Microscopy (CSLM) allowed us to observe the diffusion of micron sized colloidal spheres in cylindrical cavities, in which both height and radius are 9 particle diameters. Microfluidic chips containing pressure-controlled structured membranes [36] were used to define the liquid environment and trap the particles. Diffusion coefficients were measured via particle tracking in two horizontal planes; one crossing the cavity center and one near the bottom. Good optical contrast and a large number of observations allowed us to resolve the radial (D_r) and azimuthal (D_θ) diffusion coefficients as a function of distance from the wall, with high resolution.

This chapter is further organized as follows: in Sec.4.2 we will explain how drag forces are calculated from the 3D Stokes equation and translated into diffusion coefficients. In Sec.4.3 we describe the colloidal fluid, the design and operation of the cylindrical cavities, the video particle tracking experiments and the data analysis. In Sec.4.4 we show how spatially dependent diffusion coefficients are obtained

from image analysis, and compare the diffusive behaviors for 1 and 16 enclosed particles to each other and to numerical calculations. Conclusions will be drawn in Sec.4.5.

4.2 Numerical calculations

In the low Reynolds number regime, we have a fundamental linear relation between hydrodynamic force (F_H) and the velocity of particle (v_α), via the diffusion tensor ($\boldsymbol{D}$).

$$v = -\beta \boldsymbol{D} F_H \tag{4.1}$$

Here $\beta = 1/k_B T$ while $\boldsymbol{D}$ is a diagonal tensor with components D_r ,D_θ and D_z corresponding to the principal directions in cylindrical coordinates. The diffusion coefficient D_α in each direction can be expressed in terms of resistance and thermal energy.

$$D_\alpha = \frac{k_b T}{f_\alpha} \tag{4.2}$$

where k_B and T are the Boltzmann constant and the absolute temperature, respectively. For a spherical particle in infinite medium, Eq. 4.2 becomes the well-known Stokes-Einstein equation:

$$D_0 = \frac{k_b T}{3\pi\mu d_p} \tag{4.3}$$

where μ and d_p are the viscosity of medium and the diameter of particle, respectively. From Eq. 4.2 and Eq. 4.3, it can be shown that the normalized diffusion coefficient (D_α/D_0) is the inverse of the drag coefficient ($c_d = \frac{F_\alpha}{F_0}$).

$$\frac{D_\alpha}{D_0} = \frac{3\pi d_p v_\alpha}{F_\alpha} = \frac{F_0}{F_\alpha} \tag{4.4}$$

In our numerical simulations, the local diffusion coefficient is obtained by solving the Stokes equation to calculate the drag force $\boldsymbol{F}$ for given $\boldsymbol{v}$. This can be done for a particle at any chosen position inside the cylinder. Imposing no-slip boundary condition on the container wall and giving the particle a velocity v_α, the drag forces

and diffusion coefficients in the $r-$ and θ- directions are obtained separately by applying the velocity in these separate directions. All simulations were implemented using the commercial COMSOL Multiphysics package [37]. In these simulations, only the single particle case is considered. Hydrodynamic interactions between multiple particles are not taken into account. The numerical calculations were validated by comparing the calculated drag coefficients with analytical solutions for well-known geometries: a spherical particle near single wall and in between two walls.

4.3 Experimental Methods

4.3.1 Colloidal Fluid

Poly(styrene) latex particles with a diameter (d_p) of 1.13 ± 0.05 μm, containing a red-fluorescent dye and carboxylate surface groups were obtained as an aqueous suspension from Polysciences. This suspension was sonicated and subsequently diluted with a 100 μM NaCl solution to a particle volume fraction of approximately 0.5%. The final salt concentration corresponds to a calculated electric double layer thickness of 30 nm, which is small compared to the particle size but large enough to maintain colloidal stability. Given the size and mass density ($\rho = 1.05 g/ml$) of the particles, the sedimentation length $l = k_b T/6\pi g d_p^3 \approx 30\ \mu m$, which is large enough to prevent significant particle settling. The refractive index of the PS-latex particles is 1.6 whereas that of the aqueous solvent is 1.33. All diluted suspensions were studied at 22 ± 2 ^0C

4.3.2 Microfluidic Cylindrical Cavities

Capture of particles into 3D confinements was achieved by filling a microfluidic channel with suspension and subsequently pressing down a membrane with embedded cylinder- shaped cavities to trap fluid underneath (see Fig. 4.1). The number of particles that could be trapped varied between 1 and 16. The device used for this is a poly(dimethylsiloxane) (PDMS) based multilayer microfluidic chip

as described in ref. [41]. Briefly, the chip consists of two layers of channels running in perpendicular directions: one for containing the fluid of interest and the other for control. The ceiling of the fluidic channel is an elastomeric membrane, in which the cavities are embedded. On pressurization of the control channel, the membrane deflects and touches the floor; releasing the pressure restores the original state. Cylinders are visualized through a 170 μm thick glass slide covered by a PDMS layer of 50 μm. This application using so-called integrated Structured Elastomeric Membranes (iSEMs) allows trapping aqueous liquids in cavities of arbitrary shape, and dimensions in the micron range. Also simultaneous study of multiple cavities is possible. Our microfluidic channel had a height and width of 16 and 200 μm respectively. The cavities had a height H and diameter $2R_{cyl}$ of 10 and 20 μm respectively.

4.3.3 Confocal microscopy and Particle tracking

The Confocal Scanning Laser Microscope (CSLM) was an UltraView LCI10 system, Perkin-Elmer) containing a Nikon Eclipse inverted microscope equipped with a Nipkow disk (Yokogawa module) and 100X NA 1.3/oil objective. When tracking particle dynamics, we imaged horizontal (X,Y) focal planes for 240 s at a rate of 10 frames/s. For measuring particle locations in three dimensions (3D) we measured series of images along the Z-direction (up to 30 μm from the bottom, taking $\approx$ 60 s) at 0.1 μm/step. The images were processed via the available particle tracking codes in 2D and 3D [28]. The accuracy of locating the centroid of particles in 3D was 0.02 μ m in X-Y and 0.05 μm in Z direction. The Z-resolution of our 2D particle tracking was measured to be $\approx$ 0.8 μm (full width half maximum), by localizing (almost stationary) particles in a 3D volume and subsequently analyzing per focal plane, up to which distance from the focal plane particles were still accepted by the 2D particle tracking code (using typical selection criteria for brightness, object size etc.).

Image-time series aimed at studying particle dynamics typically consisted of 2500 time steps. After localizing all particles in each frame and building trajectories, mean squared displacements (MSDs) in the horizontal plane were calculated, using:

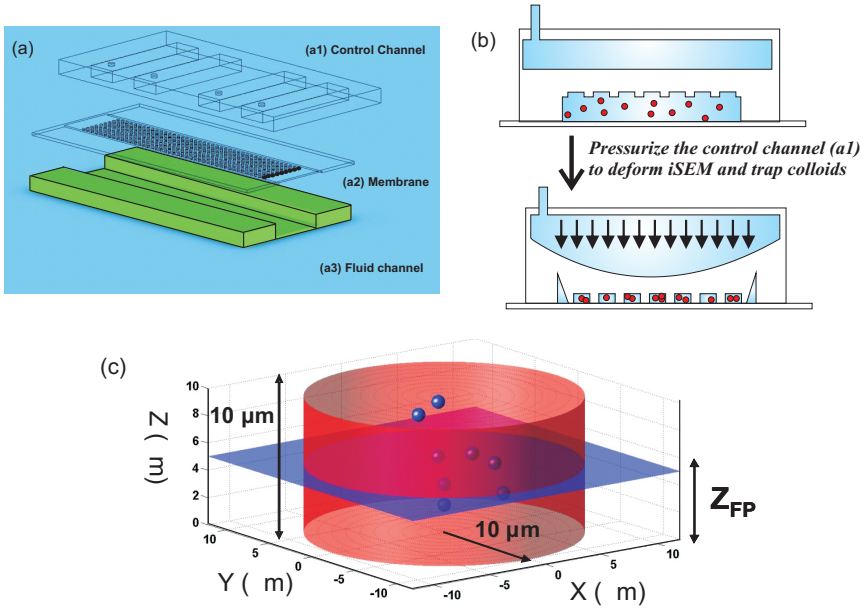

Figure 4.1: Panel a) 3D representation of our device with integrated Structured Elastomeric Membranes (iSEMs). The device consists of 3 major structures: a control channel (a1) that can be pressurized, a membrane (a2) in which cylinder structures are defined, and a fluidic channel (a3) via which particles and solvent are delivered. The control and fluidic channels intersect each other perpendicularly. Panel b) Applying pressure to the control channel leads to deflection of the membrane and trapping of the particle suspension. Panel c) Schematic illustration of the experiment in which the particles are imaged in a chosen focal plane of a confocal microscope

4.3.4 Confocal Scanning Laser Microscope

Images were recorded with an UltraView LCI 10 CSLM system (Perkin Elmer), consisting of a Nikon Eclipse inverted microscope, a Yokogawa (Nipkow disk) confocal unit and a Hamamatsu 12-bit CCD camera. All recordings were done in fluorescence mode using a 25 mW laser with α = 641 nm and a 100X/oil objective with NA=1.3. The pixel size corresponding to the images was 0.135 μm and the frame rate was 10 per second. Different focal planes and different numbers of particles per cavity were studied; for each condition 6 subsequent movies of ≈ 8000 frames each were recorded.

4.3.5 Particle Tracking

The majority of our image analysis (section 3.5) is based on the accurate localization and tracking of particles; this was done using the IDL implementation of the algorithm from Crocker and Grier [38]. Additional procedures that are commonly used for data inspection and error analysis have been described in detail [39] and are not repeated here. Few aspects that were specific for the present study will follow now. Due to the refractive index mismatch between particles and solvent, image distortion occurred and also the optical contrast deteriorated with increasing depth (Z). However, due to the low particle concentration, sufficient visibility could be obtained at all Z-values of interest. At Z = 5 μm above the PDMS floor, the localization accuracy in the (X,Y) focal plane was 30 nm as in an earlier study [40]. The 'effective focal depth' relevant for particle tracking was estimated to be 2.0 μm from an intensity-vs.-Z scan of a particle that was stuck to the bottom. A more detailed discussion of 'effective focal depth' is given in the Supplementary Information. The same immobilized particle also allowed estimating the mechanical drift of the cavities; we found it to be less than 1 pixel per 100 s, which is negligible for our purpose

4.3.6 Image Analysis

Cavity Geometry

To inspect the 3D geometry of the cavity, we employed two different methods. In the first method, fluorescently dyed aqueous liquid was pumped into the chip and directly visualized by making horizontal (X, Y) images at various vertical (Z) locations. This allowed a fairly accurate measurement of the contour in the horizontal plane, and an estimate of the cavity height (see Appendix). A second, independent check of the (X, Y) contour was made after replacing the dye solution by suspension, and localizing the captured particles for typically $5x10^4$ frames. Making a time projection of all locations where a particle was found, resulted in a cloud representing the accessible area. From this cloud, a contour line was constructed by connecting the outermost points. A careful smoothening was applied, which resulted in a contour that contained all but a few particles. The excluded particles were still very close (1 pixel) to the calculated contour and reflect the uncertainty in the localization of the contour. Finally the contour was inflated by 1 particle radius, to account for the fact that the localizations pertained to the centers of the particles. For the cavity with 16 particles, the contours found with the two methods corresponded well to each other and to the dimensions of the PDMS master, from which the iSEMs had been made (not shown). With only 1 particle in the cavity the visualization with fluorescent liquid worked better.

It turned out that the cylinders did not display perfectly circular cross sections (see Fig. 2 for an example), which necessitated a description of the radial position of the wall R_{max} as a function of the angle θ. The transformation from Cartesian (X, Y) to polar (R, θ) coordinates was made by localizing the cavity center and subsequently decomposing the relative vectors (ΔX, ΔY) into R and θ components. Performing this operation also on the calculated contour line, resulted in a R_{max} (θ) function, which turned out to have a specific dependency for individual cavities. To facilitate description of the contour, we described it with a Fourier series:

$$R_{max} = R_{fit} + \sum_{l}^{m} A_m sin(m\theta) + B_m cos(m\theta) \tag{4.5}$$

with a truncation at m=4. The quality of this fit turned out to be very good.

Diffusive behavior

As explained in Sec.2, local diffusion coefficients D_α were calculated from resistance and thermal energy. Experimentally they can be measured from the mean squared displacement $\langle \Delta r_\alpha^2 \rangle$ using the Einstein-Stokes-Sutherland equation:

$$\left\langle \Delta \mathbf{r}_\alpha^2 \right\rangle = 2D_\alpha \tau \ where \ \alpha \ \in \ r, \theta, z \tag{4.6}$$

with $\Delta \boldsymbol{r} = \Delta R \mathbf{e}_r + R\Delta\theta \mathbf{e}_\theta + \Delta z \mathbf{e}_z$ and $\mathbf{D} = D_r \mathbf{e}_r \mathbf{e}_r + D_\theta \mathbf{e}_\theta \mathbf{e}_\theta + D_z \mathbf{e}_z \mathbf{e}_z$. Here τ is the lag time and $\Delta \mathbf{r}_\alpha$ the α component of the vector that describes the 2D displacement of a particle during that time. In our case, the brackets indicate an averaging over different times and particles at a given location. In Eq. 4.2 D_α can be expressed as a diagonal tensor which has components D_r ,D_θ and D_z corresponding to the principal directions in cylindrical coordinates. In our experiments, we focused on the in-plane MSD hence only D_r ,D_θ are measured. The diffusion coefficient was measured from the initial slope corresponding short time behavior.

A fundamental question is, how to define the location where D_α is measured, given that D_α itself is measured via a displacement. If the length scale over which the MSD can show spatial variation is much larger than the typical magnitude of $\Delta \mathbf{r}_\alpha$ (as in [41]) then this is only a minor issue. In the present study, where strong variations in D_α can be expected close to the wall, we optimized the spatial resolution by considering $\Delta \mathbf{r}_\alpha$ only for the smallest (i.e. unit) time step τ_1 (=100 ms). This generated a minor secondary issue: since the exposure time of the camera per image (σ) was only slightly smaller than τ_1, the found magnitude of $\langle \Delta r_\alpha^2 \rangle$ had to be corrected by subtracting $\sigma/3$ from τ as prescribed by Eq. (14) of Savin et al [42]. Our σ was measured from a plot of $\langle \Delta r_\alpha^2 \rangle$ vs. τ for a bulk viscous liquid (see Appendix).

Unless mentioned otherwise, the location of D_α was assigned to the midpoint of $\Delta\mathbf{r}_\alpha$. Rounding the measured X,Y locations to discrete (pixel) numbers was done to make a pixel map which could be presented as an image; for a cavity with 16 particles observed for $\approx 5 * 10^4$ frames, a pixel was typically 'hit' 20 times. To distinguish between the fundamentally different diffusion directions in a cylinder and to allow averaging over equivalent pixels, Δr_α was decomposed into radial (R) and azimuthal (θ) directions. This produced values of D_r and D_θ as a function of R and θ. In our analysis the distance ΔR from the cylindrical wall is a more appropriate variable than R. In view of the slight deviations from a perfect cylindrical shape (see Sec.4.3.6), we used the Fourier description (Eq. 4.6) of R_{max} (θ) to calculate $\Delta W(\theta)$ (or its normalized form ξ)

$$\Delta W(\theta) = R_{max}(\theta) - R \; and \; \xi = \Delta W / d_p \tag{4.7}$$

Hereafter Eq. 4.7 was used to group data for D_r and D_θ measured at the same ΔR.

4.4 Results and Discussions

4.4.1 Spatial dependence of diffusion coefficients

To start with an overview we first show representative maps for the normalized diffusion coefficient (Fig. 2a) and the occurrence frequency (Fig. 2b). Both maps were measured in the midplane ($Z_{FP} = H/2$) of the cylinder. It turns out that even farthest away from the walls, D_α is significantly lower than that of a free particle in bulk liquid. Moreover it is clearly visible that D_α is progressively reduced as the cylindrical wall is approached. The occurrence map looks fairly homogeneous except for a depletion zone in the vicinity of the cylindrical wall (this will be discussed in Sec.4.4.2).

A closer inspection of Fig. 4.2b reveals two issues that had to be addressed. Firstly, at two (X,Y) locations the occurrence probability was significantly larger: near the cylindrical wall at (X=22, Y=23) and near the center at (18,15). Both particles appeared to be sticking to a wall for at least part of the time. The particle near the

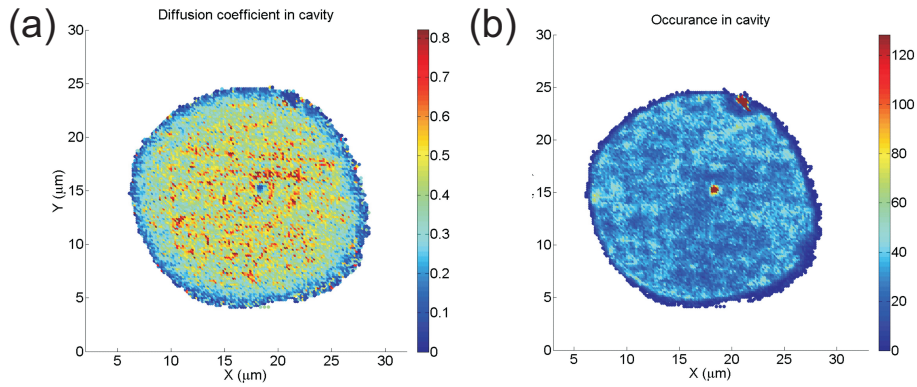

Figure 4.2: Overview for the experiment with 16 particles, with all trajectories superimposed. Panel (a) Diffusion coefficient (D_α) in the midplane ($Z_{FP} = H/2$) of the cylindirical cavity, as a function of (X, Y) position. D_α has been normalized with respect to the diffusion coefficient of a free particle in pure solvent (D_0). Panel (b) Corresponding map for the number of times that a particle was found in each (X, Y) pixel.

center appeared to be at the bottom plane, and was detected due to an enhanced brightness for such particles (see also below). The other particle was clearly stuck to a cylindrical wall. Overall such sticking events were rare; in 60 hours of recording only 3 such cases were found. Secondly, also slight temporal fluctuations of the cavity contour were observed. This was manifested as small differences between the contours found from subsequent movies, and shows up in the time-projection of Fig. 4.2b as an increased width of the particle depletion zones in the lower and right-hand parts. Both issues (whenever they occurred) were resolved by excluding the problem areas from the analysis. Omitting this filtering operation resulted in significantly different results (in Figs. 4.3, 4.4, 4.5) in the vicinity of walls.

4.4.2 Dynamics at the midplane

More detailed information was obtained by binning data as plotted in Fig. 4.2b according to the distance from the cylindrical wall, and decomposing the diffusion coefficient into radial and azimuthal components as explained in Sec.4.3.6. We first consider 1 particle in the midplane (Z_{FP}=H/2) of the cylinder. The experimental data in Fig. 4.3 reveal several aspects. In the center of cavity D_r and D_θ are equal, while the total D_α is $\approx 25\%$ lower than the bulk value D_0. As the particle approaches the side wall along the radial direction, its diffusion coefficient follows a plateau, down to ≈3 particle diameters from the wall, where a gradual decrease sets in. This decrease is stronger for D_r, which is qualitatively in line with expectations from the known diffusive behavior of a particle near a single flat wall: here the perpendicular drag force is always greater or equal to the parallel drag force [20].

Also shown in Fig. 4.3 are numerical calculations (see Sec.4.2) that take into account the specific 3D geometry of our experiments. The theoretically predicted trends of D_r and D_θ as a function of ξ correspond remarkably well with those of the experiments. Concerning the magnitudes, a 10% discrepancy is found between the model and the experiments. We think this should mainly be ascribed to the error introduced by the normalization step with D_0 : the latter quantity may have been measured at a slightly lower temperature. Another experimental error could be due to the slight uncertainty in the size of the individual particle in the cavity. Finally, we remark that the signal/noise (S/N) ratio of the experimental data is fair, even for ≈ $5x10^4$ observations.

The case of 16 particles in the cavity suffers less from poor statistics, but the question is to what extent the diffusive behavior is the same. The still rather low particle volume fraction ($\phi \approx 0.004$) suggests that close-range hydrodynamic interactions ('collisions') between the particles will rarely occur. A comparison between the cases of 1 and 16 particles per cavity is shown in Fig. 4.4. The corresponding curves for D_r and D_θ look fairly similar. The data for the 16 particles show a slightly less steep decay near the wall, and in the center of the cavity D_α appears to be 5% smaller. The latter discrep-

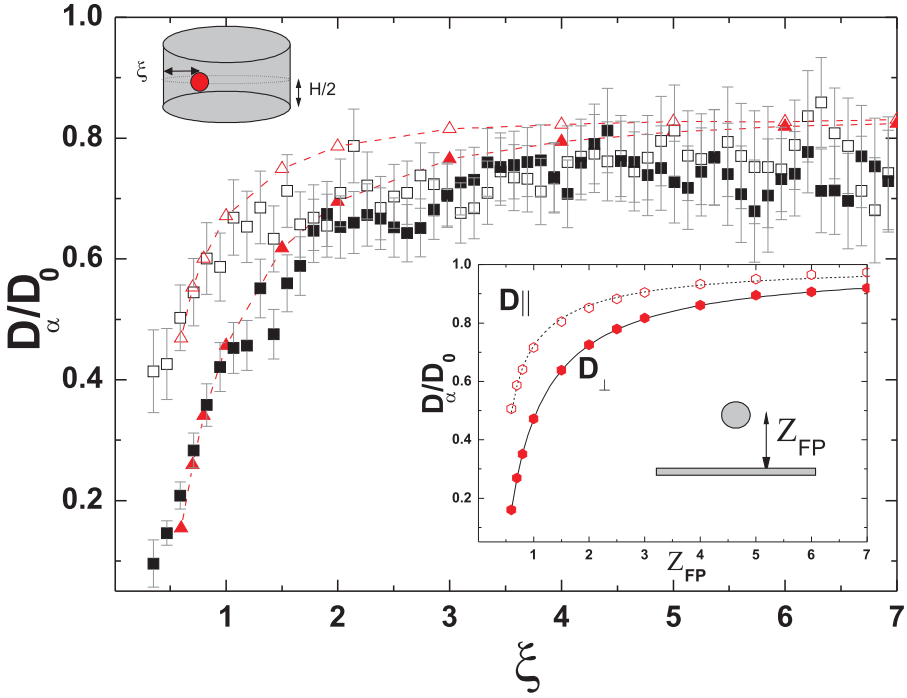

Figure 4.3: Normalized diffusion coefficients of a single particle in the Z-midplane of the cavity, plotted versus the normalized distance (ξ) from the cylindrical wall. Squares (open for D_θ, closed for D_r) show the experiments, while vertical bars represent estimated standard deviations (see text). Triangles connected by dashed lines correspond to the numeric solution of the 3D Stokes problem. The inset shows the validation of the numerical method against the reference case of a particle near a flat wall. The diffusion coefficient parallel (D_{II} ,open circle) and perpendicular ($D_\perp$,solid circle) to single wall as function of distance from the wall (Z_{FP}). Circles show our calculations while red dashed lines represent the analytical solution from Brenner [20]. Similar quantitative agreement was found for the case of 2 parallel walls (not shown).

ancy falls within the experimental error. Whether the former small difference could perhaps reflect inter-particle hydrodynamics remains to be elucidated, and would require a different simulation method. In any case, the better statistical accuracy of the experiment with 16 particles allows addressing several additional questions. We first address the accuracy that can be reached in measuring local diffusion coefficients with our particle tracking method. Uncertainties exist in both the magnitude of D_α and in the location where it is measured, and the errors can be either systematic or stochastic.

A first issue is related to the assignment of a location to the measured D_α. Different choices can be made: the beginning-, end- or midpoint of the diffusive displacement $\Delta\mathbf{r}_\alpha$. The consequences of this choice are shown in the inset of Fig. 4.4. The differences are only small, which is rationalized by the fact that the typical displacement in $\tau_l = 0.1$ s is only 0.1-0.2*ξ. At the smallest ξ, the value of D_r based on the midpoint is smaller than for the begin/end point. This can be understood by considering that of all radial displacements that begin or end in the ring closest to the wall, only those that are small will also have the midpoint in that ring. Larger steps will result in midpoints at larger ξ. This biasing effect applies only for radial displacements in the outer ring.

A second issue is the drift (i.e. nonzero average displacement [43]) due to the gradient of the diffusion coefficient ($\frac{\partial D_r}{\partial \xi}$) in the radial direction, which can make a contribution to $\langle \Delta\mathbf{r}_\alpha^2 \rangle$, proportional to ξ^2. We simulated this effect for the case of a particle near a flat wall, and found (see Appendix) that on using the Einstein-Stokes equation, the local D_r (perpendicular to the wall) had to be replaced by:

$$D_r^{eff}(\xi) = \frac{2\xi - 1}{2\xi}\left[1 + \frac{4\xi^2 - 3(2\xi - 1)}{8\xi^3(2\xi - 1)}\right] \tag{4.8}$$

with $\acute{\tau}$ the normalized lag time ($\acute{\tau} = \tau/t_0$, where $t_0 = d_p^2 D_0$), which amounts 0.028 in our case. The term in round brackets incorporates the effect of the wall on the drag coefficient while the term in square brackets represents the drift effect. The latter term is always > 1 but becomes < 1.1 for $\xi > 0.58$. This means that the correction term

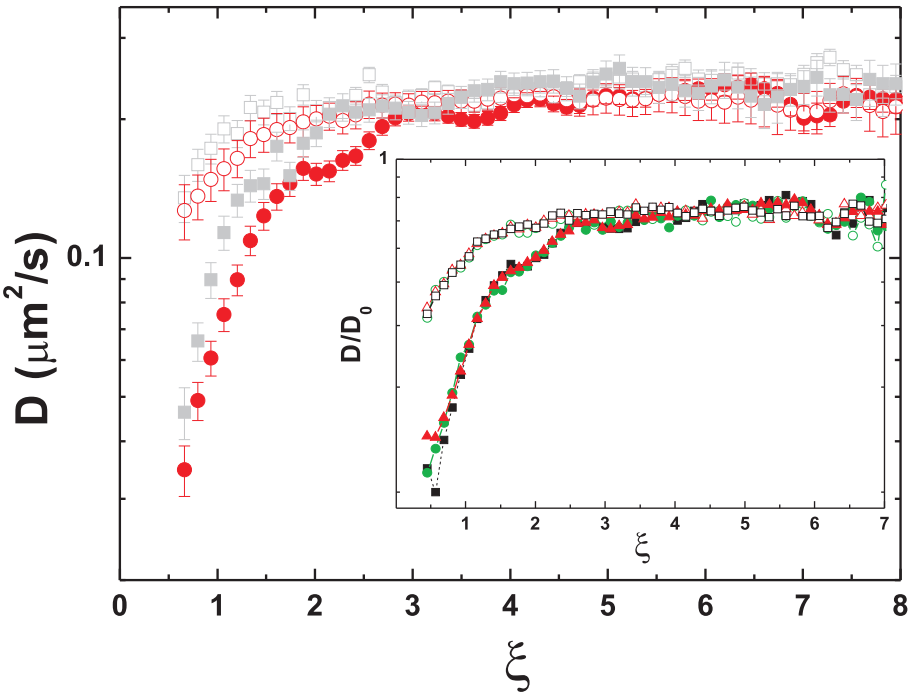

Figure 4.4: Comparison between diffusive behaviors of 1 particle (grey squares, same data as Figure 4.3) and 16 particles (red circles) in the mid-plane of the cavity (Z=H/2). Note that the diffusion coefficients are now given in absolute numbers. The inset shows (for the case of 16 particles) how the apparent D_α/D_0 depends on the assignment of the location where D_α was measured: begin-, (red triangles) end- (green circles) or midpoint (black squares) of the displacement step. Open symbols correspond to D_θ and closed symbols to D_r.

only plays a role very close to the wall (1 camera pixel in our case). Although the correction is thus only minor for our case, it is also clear from Eq. 4.8 that this is due to the small value of τ.

A third issue is how the magnitudes of D_α are affected by localization errors. The measured coordinates of the contour and center of the cavity suffer from inaccuracies that are larger than that of the particle localizations, and it is obvious that the strongest influence of these errors is expected near the wall. We examined this issue by repeating the image analysis but now increasing or decreasing the local contour radii $R_max(\theta)$ by $0.15*d_p$. Also the X and Y coordinates of the cavity center were varied by the same amount. Comparing D_α values at the same Δr for the different datasets thus created, allowed to estimate a Δr-dependent standard deviation. To obtain the total standard deviation, these errors were combined with the statistical inaccuracy that arises from the finite number of observations N within each Δr ring. The relative error due to this effect amounts $(2/N)^{\frac{1}{2}}$ and is also Δr-dependent. The resulting error bars for individual cases are shown in Figs. 4.3 and 4.4. It turns out the typical relative error in D_α is 8% for 1 particle per cavity and 4% for the 16 particle case.

Bottom plane

For the case of 16 particles, the diffusive behavior at the bottom of the cavity could also be examined, albeit that an additional data filtering step was needed to ensure that only particles very close to the bottom are taken into account. The need for this step arises from the fact that the Z-range in which particles are detected is $\approx 2\mu m$ (see Appendix). With the focus at $Z_{FP} = 4.5 \pm 1\mu m$, this effect is unimportant, since the distance δZ of a particle to the nearest wall varies only between 4 and 5 μm. However at $Z_{FP} = 0.5d_p$, ΔZ varies between 0.5 μm (contact) and 2 μm. In this range D_r and D_θ can be expected to show strong dependence on Z position.

To exclude particles that are not very close to the bottom, we collected the intensities of all $\approx 10^5$ particles tracked at $Z_{FP} = 0.5d_p$, into a histogram (see inset of Fig. 4.5). Two distinctive peaks were found, which differ in intensity by a factor of ≈3. We then assumed

that only this secondary peak corresponds to particles at the bottom, and restricted our analysis to this subset. The fact that this data selection gave substantially lower values for D_r and D_θ, whereas a similar filtering at $Z_{FP} = H/2$ had negligible effects, seems to justify our assumption.

The thus measured dependencies of D_r and D_θ on ξ at the bottom plane are presented in Fig. 4.5, together with the data observed in the midplane (and with numerical simulations). For ξ >3, the proximity of the bottom plane is manifested as a $\approx 25\%$ reduction in the D_α values as compared to the midplane. As the cylindirical wall is approached (ξ <3) a transition takes place to a regime in which the drag force becomes strongly dominated by the cylindirical wall. This is evident from the quantitative correspondence at small ξ of the D_r and D_θ curves measured at the bottom and mid-planes.

The comparison to numerical calculations revealed some interesting aspects. Since the inaccuracy in Z_{FP} was estimated to be 0.2 μm, calculations were performed for $Z_{FP} = 0.6 - 1.5 * d_p$. The results (shown in the Appendix) revealed that the plateau levels for D_r and D_θ depended strongly on Z_{FP}, and that the best agreement with our experiments was found for $Z_{FP} \approx 0.6\mu m$. It also turned out that all calculated D_r curves showed a very similar limiting behavior for $\xi < 1$, which was however significantly steeper than that of our experiment. This is also shown by the numerical D_r curve in Fig. 4.5. Part of this discrepancy could perhaps be attributed to a slightly less steep ξ dependence for the case of 16 particles (as remarked before). Besides that, we have no explanation for the discrepancy. For the D_θ curves, comparison between simulation and experiment produced a better correspondence than for D_r.

Comparison with other geometries

To further emphasize the effect of confining geometry on the spatial dependence of local diffusion behavior, we performed additional numerical calculations. In Panel (a) of Fig. 4.6 we compare the radial and azimuthal diffusion coefficients for three distinct geometries: (1) our closed cylinder ($R_{cyl} = 9d_p$, $H = 9d_p$) at the midplane ($Z_{FP} = H/2$), (2) an infinitely long cylinder with $R_{cyl} = 9d_p$ and (3) a

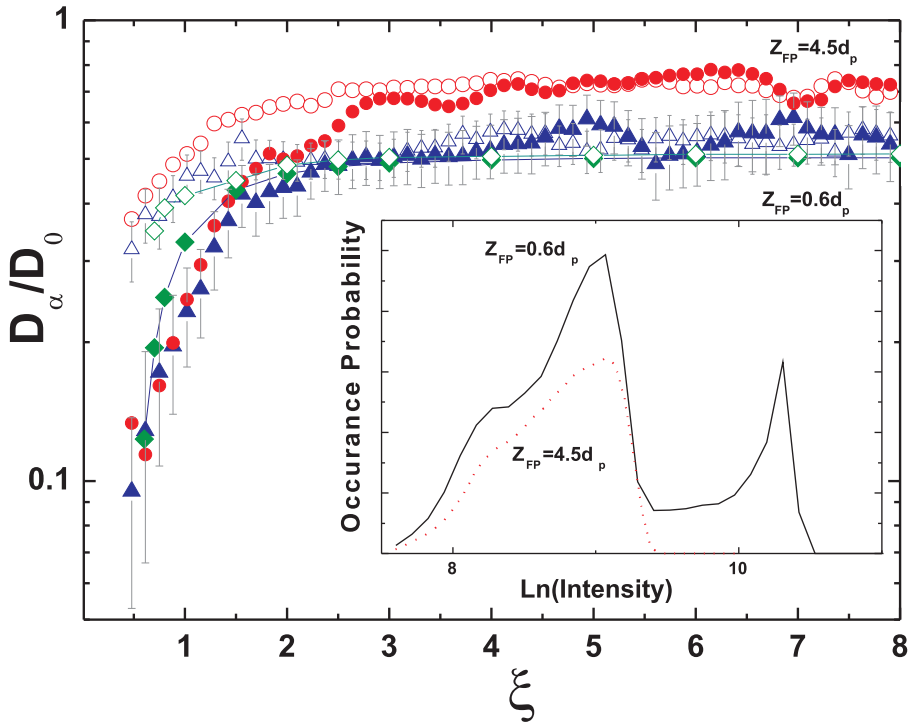

Figure 4.5: Normalized radial (D_r) and azimuthal (D_θ) diffusion coefficients measured at the midplane ($Z_{FP} = H/2$, red circles) and bottom ($Z_{FP} = 0.6d_p$, blue triangles) for the case of 16 particles in the cavity. Open symbols correspond to D_θ and closed symbols to D_r. Diamonds connected by solid lines show the numerical solution of the 3D Stokes equation. Open symbols correspond to D_θ and closed symbols to D_r.The inset shows histograms for the intensity measured at $Z_{FP} = 0.6d_p$ (solid line) and $Z_{FP} = H/2$ (red dashes). This intensity corresponds to the brightness of the fluorescent image of a particle, which depends on its distance to the focal plane $Z - Z_{FP}$ as well as on Z_{FP} itself.

single flat wall. Comparing cases (1) and (2), we find that for small ξ (ξ <2) the diffusive behavior is largely dominated by the cylindrical wall; this is similar to the experimental trend in Fig. 5. However as the central axis of the cylinder is approached, the limiting behaviors are clearly different: even 4.5 particle diameters away from top and bottom surfaces, the latter boundaries still lower the value of D_α by 8% compared to the infinite cylinder case. To reduce this difference to 1%, the distance of the end planes from the center has to reach 20 particle radii (data not shown).

To further corroborate the importance of end planes, we also compared the previous cases (1) and (2) with calculations for a cylinder with $R_{cyl} = 9d_p$and $H = 9d_p$ but now with one end open. Fig 6b shows once again that in the vicinity of cylindrical wall, all curves collapse. Closer to the center of the cylinder, the diffusion behavior is clearly influenced by the absence of end planes. Each added boundary further decreases the limiting value for both D_r and D_θ .

Finally we also examine the influence of wall curvature. The comparison between the cases of an infinitely long cylinder and a single flat plane reveals that very close to the wall ($\xi < 1.5$) the diffusivities of the particle are essentially the same in Figure 6a. This indicates that very close to the wall, the curvature of the latter can be neglected for $R_{cyl}/d_p \leq 9$. However close to the radial axis, the diffusion behavior is notably different. In summary, the calculations given in Figure 6 illustrate once more that -as a rule- the complete 3D geometry needs to be considered to obtain a quantitative description of spatial distribution of local diffusion.

4.4.3 Particle depletion near the wall

We now discuss the occurrence map N(X,Y) shown in Fig. 2b. A slight but measurable depletion of particles occurs near the cylindrical wall, which raised questions about its origin and possible implications. Both thermodynamic particle-wall interactions and fluctuations of the wall could be responsible. To examine this further, we calculated the occurrence probability P as a function of distance from the wall, by radial averaging. The data in Fig. 4.7 show that P remains fairly constant down to $\xi \approx 0.65$. In the range $\xi = 0.5 - 0.65$,

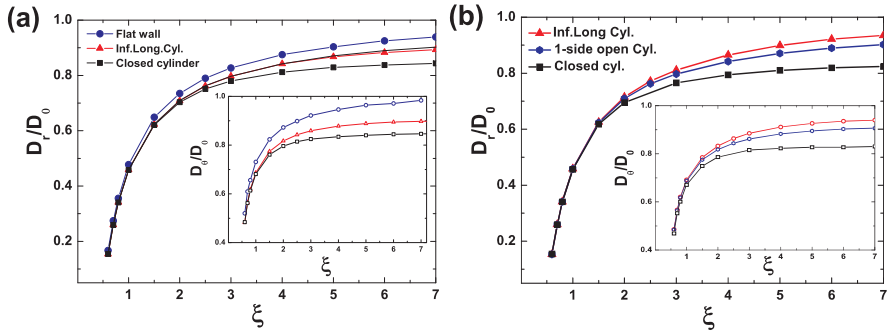

Figure 4.6: Numerical simulations. Panel (a): Effect of confinement geometry on the normalized radial diffusion (D_r) coefficient as a function of dimensionless distance (ξ) from the wall. Geometries: infinitely long cylinder ($\triangle$ red, $R_{cyl} = 9d_p, H = \infty$), closed cylinder ($\square$ black, $R_{cyl} = 9d_p, H = 9d_p$, at midplane $Z_{FP} = 4.5d_p$) and single flat wall (blue, $\bullet$). Inset (a): normalized azimuthal diffusion (D_θ) coefficient vs. ξ for the same cases.Panel (b): Effect of top and bottom flat walls on the normalized radial diffusion (D_r) coefficient as a function of ξ. Symbols represent an infinitely long cylinder ($\triangle$ red, $R_{cyl} = 9d_p, H = \infty$), a finite closed cylinder ($\square$ black, $R_{cyl} = 9d_p, H = 9d_p$, midplane $Z_{FP} = 4.5d_p$) and the last mentioned case with one flat wall removed ($\diamond$ blue, $R_{cyl} = 9d_p, H = 9d_p$, mid-plane $Z_{FP} = 4.5d_p$) Inset (b): Normalized azimuthal diffusion (D_θ) coefficient vs. ξ for the aforementioned cases .Open symbols correspond to D_θ and closed symbols to D_r.

P decreases sharply to zero. Although this range is only 150 nm ($\approx$ 1 camera pixel), the effect is still significant, and the range is 5 times larger than the expected electric double layer thickness (see Sec. 4.3.1).

Anticipating that wall contour fluctuations are at least partly responsible for the effect, we performed two types of quantitative analysis. Firstly we tracked the particle that appeared to be attached to the side wall (Fig. 2b); it turned out that this particle was oscillating with a radial amplitude of $\approx$ 70 nm. Secondly we analyzed the uncertainty in the local radial position of the wall, by comparing for each movie, 2 sets of $R_{max}(\theta)$: the "'*smooth*"' contour obtained

from fitting with Eq. 4.8, and the noisy primary data. The difference Δr_{max} did not show any systematic dependence on θ and its distribution $P(\Delta r_{max})$ had a standard deviation σ of 140 nm. This σ, which includes the contribution of dynamic wall fluctuations, matches very well with the found depletion range. To further illustrate this, we took a step function $P(\xi)$ as expected for hard spheres and walls, and convoluted it with the distribution $P(\Delta r_{max})$. As can be seen in Fig. 4.7, the resulting curve agrees very well with the experimental $P(\xi)$ data. Finally, we also did a computer simulation in which a screened electrostatic repulsion between particles and wall is included. Here it turned out that the additional change in our $P(\xi)$ due to a potential with a contact value of 8 k_BT and a Debye length of 30 nm has a negligible effect.

The implications of these findings for the present study are: i) it is corroborated that the thermodynamic interactions between particles and wall are essentially like that of hard surfaces and ii) fluctuations of the PDMS wall cannot be excluded, but if so, their amplitude does not exceed 150 nm. This latter aspect was already taken into account in the error analysis of $D(\Delta r)$ and appears to have rather small impact on our measurements of the local diffusion coefficient. Interestingly, the case of a fluctuating wall could also be found in systems occurring in nature, e.g. emulsion droplets or living cells. Our method of measuring diffusive behavior in confinements with fluctuating walls might be suitable for studying such cases as well.

4.5 Conclusions and Outlook

In the present study, three novel aspects were combined: the microfluidic trapping of particles into a closed 3D confinement with a designed geometry, application of particle tracking to measure both interactions and diffusion coefficients near walls, and the combination of experiments and numerical modeling to examine effects of 3D confinement on local diffusive behavior. Several conclusions can be drawn: 1. For the first time, spatial dependence of radial and azimuthal diffusion coefficient have been measured for particles in a closed cylinder. 2. Numerical calculations based on the solution

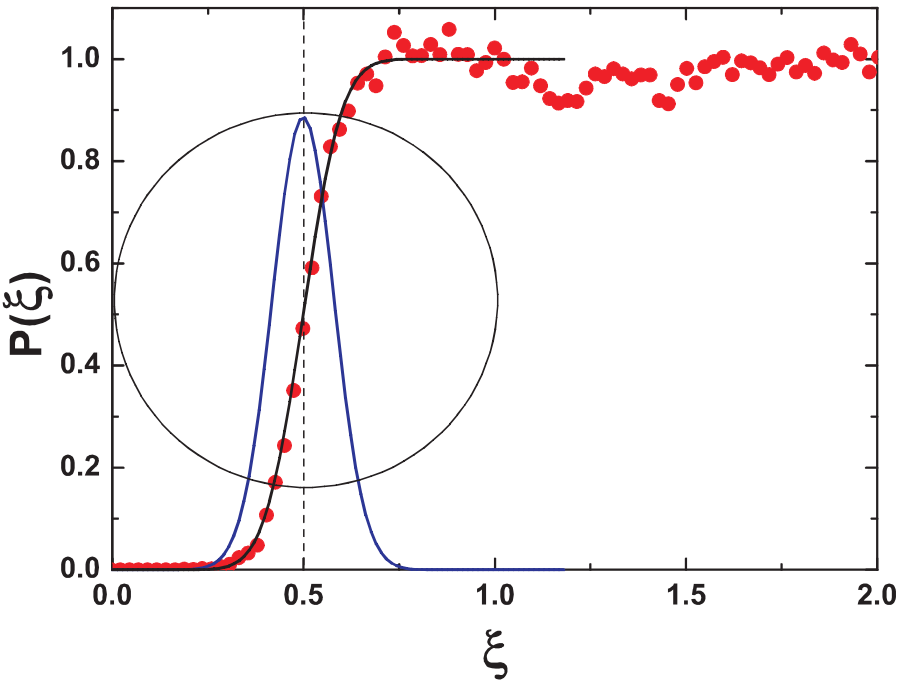

Figure 4.7: Red circles: probability of finding a particle center as a function of dimensionless distance from the cylindrical wall. This measurement was made at the $Z = H/2$ plane, with 16 particles in the cavity. $P(\xi)$ is normalized to the value measured in the central area. The solid black line shows the expected $P(\xi)$ profile taking into account the uncertainty in detecting the cylindrical wall. The error distribution corresponding to the latter uncertainty is given by the solid blue line. The circle indicates the size of the particle.

of the 3D Stokes problem for a single particle correspond remarkably well with the experimental results. For the experiments with 16 particles slight discrepancies from numerics are observed which can be attributed to particle-particle hydrodynamics. 3. Very close the cylindrical wall, the curvature of this wall does not have significant influence on the local diffusion coefficients. 4. Along the central axis of the cylinder, the presence of the top and bottom walls has significant influence on the magnitude of the diffusion coefficient, for all axial positions. Hence to predict the complete spatial dependence of local diffusion coefficient quantitatively, the complete 3D geometry of the confinement needs to be taken into account.

A current limitation of the iSEM-based cavities is that particles could not be trapped in large numbers. The ability to reach higher volume fractions inside 3D cavities would be very interesting, since it would allow studying at which number of particles or volume fraction the effect of particle-particle hydrodynamics becomes manifest, and how these interactions will change the local diffusive behavior. This will be topic of further study.

4.6 Acknowledgments

We thank D. Wijnperle for contributions in iSEM design and manufacturing, D. Mampallil, O. Agbaba and T. Yigit for early experiments, R. Nauta for Labview programming of microfluidic pumps. We are also grateful for discussions with S. Vanapalli on microfluidics and with M. Ekiel-Jezewska on hydrodynamics. This work was financially supported by the Chemical Sciences division of the Netherlands Organization for Scientific Research NWO (ECHO grant).

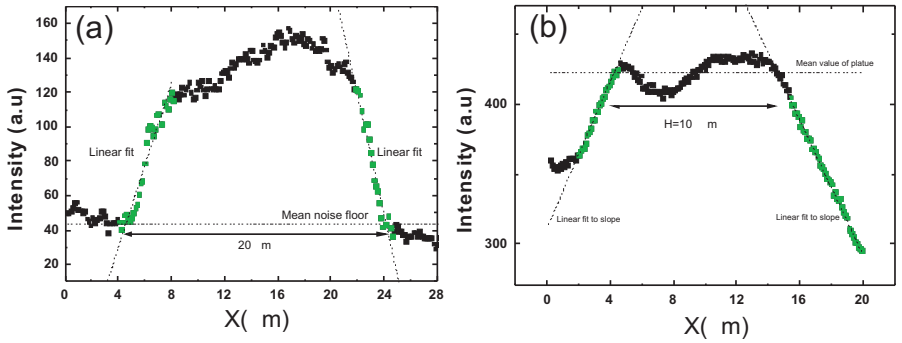

Figure 4.8: Fluorescence intensity along horizontal (A) and vertical (B) lines passing through the center of the object

4.7 Appendix

4.7.1 Size and Shape of the cavity

We confirmed the shape of the cavity with CSLM. Cavity filled with fluorescent liquid is imaged by moving the focal plane (X,Y) in the Z direction. Panel A of Figure 1 shows the intensity measured in the bottom plane (Z=0) by a (4 pixels wide) line that spans the entire Y-range, and scans in the X-direction through the center of the cylinder. From the intersecting lines, a diameter of 10 μm is obtained. Panel B indicates the intensity measured by a 5 pixel by 5 pixel region in the center of cylinder along the Z axis. The Z-range in this plot has been corrected for the refractive index of the water. subsection

4.7.2 Effects of finite shutter time

In our measurements we consistently observed a deviation from the Einstein-Stokes-Sutherland behavior at short lagtimes (for both the cavity and bulk measurements). To understand the cause of this, we performed Brownian Dynamics simulations to explore the effect of a finite shutter-time as suggested by Savin et al.: when averaging over time, trajectories are coarse-grained which results in apparent

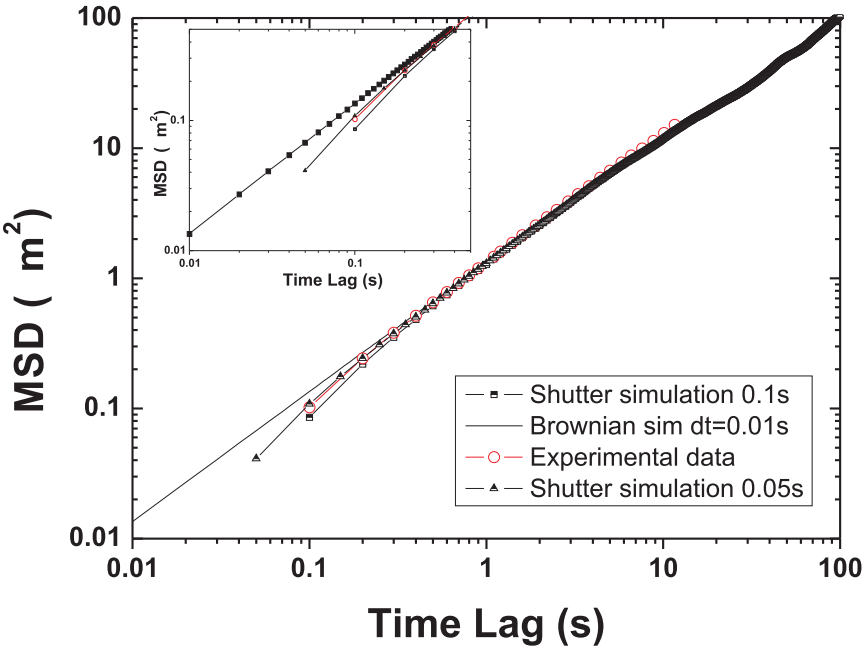

Figure 4.9: MSD vs time lag for Brownian simulations with/without shutter time and experimental data. Inset shows at close up to short lag time behavior.

mean-squared displace-ments that are smaller. We found quantitative agreement between our experimental data and the simulations when taking an effective shutter time of 50 ms (for a time lag of 100 ms). This indicates that the reduction in measured MSDs is very likely to shutter-time effects only, and that it can be corrected by the statistical model of Savin et. al. or the correction factor from Brownian simulations

4.7.3 Effective depth of focus

When the focal plane is set at a certain height (Z_{FP}), also particles that are not exactly in the focal plane will contribute to the MSD measurements. The extent to which this occurs depends on

the tolerance criteria of the particle tracking procedure. To identify the effective depth of this focal plane, we considered a single particle that was fixed to the bottom of the cylinder, and recorded a stack of images along the Z-direction. Imaging conditions and tracking parameters were identical to those in the other experiments. Plotting the brightness (the most effective screening parameter) as a function of Z and applying the threshold produces the shaded region, from which an effective focal depth of $\approx 2\mu m$ is obtained. This indicates that particles that have centers within 1 μm above and below the focal plane will contribute to measurements. When the focal plane is fixed at $Z_{FP} = H/2$ this averaging effect will not dramatically influence the diffusion coefficients measured as the variation of D_r/D_0 and D_θ/D_0 with respect to ZFP is small around the center of cavity (see Figure 4b and 5b). Close to bottom wall a stricter screening is required as the dependence of diffusion coefficients with respect to Z_{FP} is strong (see Figure 4 in main text). For this case the estimated effective focal depth is around 0.2 μm.

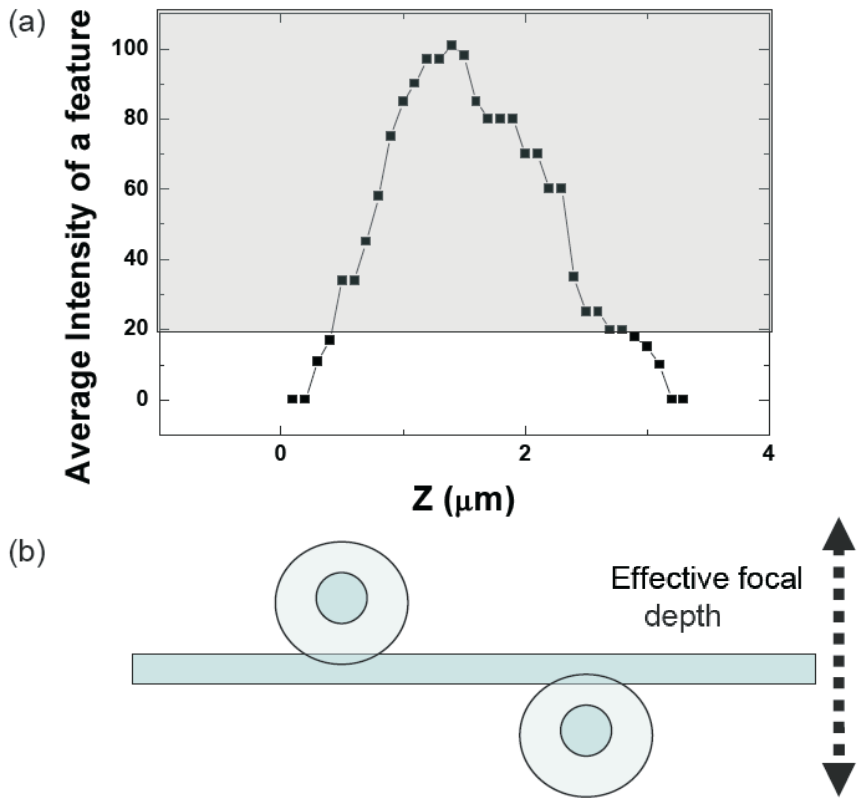

Figure 4.10: Measurement of the effective focal depth.

Bibliography

[1] J. Happel. *Low Reynolds Number Hydrodynamics*. Kluwer Academic Publishers, 1983.

[2] S. Kim. *Microhydrodynamics*. Dover Publications,New York, 2005.

[3] T. M. Squires and S. R. Quake. Microfluidics: Fluid physics at the nanoliter scale. *Rev. Mod. Phys.*, 77(3):977, Oct 2005.

[4] K. van Ommering, C. C. H. Lamers, J. H. Nieuwenhuis, L. J. van IJzendoorn, and M. W. J. Prins. Analysis of individual magnetic particle motion near a chip surface. *J. Appl, Phys.*, 105(10):104905, 2009.

[5] T. M. Squires, R. Messinger, and S. R. Manalis. Making it stick: convection, reaction and diffusion in surface-based biosensors. *Nature Biotechnology*, 26(4):417–426, 2008.

[6] E. Beerdsen, D. Dubbeldam, and B. Smit. Understanding diffusion in nanoporous materials. *Phys. Rev. Lett.*, 96(4):044501, Jan 2006.

[7] I. Shestopalov, J. D. Tice, and R. F. Ismagilov. Multi-step synthesis of nanoparticles performed on millisecond time scale in a microfluidic droplet-based system. *Lab on a Chip*, 4(4):316–321, 2004.

[8] S. G. J. M. Kluijtmans, E. H. A. de Hoog, and A. P. Philipse. Self-diffusion of charged colloidal tracer spheres in transparent porous glass media: Effect of ionic strength and pore size. *J. Chem. Phys.*, 108(17):7469–7477, 1998.

[9] S. G. J. M. Kluijtmans, J. K. G. Dhont, and A. P. Philipse. Dynamics of uncharged colloidal silica spheres confined in bicontinuous porous glass media. *Langmuir*, 13(19):4982–4987, 1997.

[10] I. Golding and E. C. Cox. Physical nature of bacterial cytoplasm. *Phys. Rev. Lett.*, 96(9):098102, Mar 2006.

[11] M. M. A. E. Claessens, R. Tharmann, K. Kroy, and A. R. Bausch. Microstructure and viscoelasticity of confined semiflexible polymer networks. *Nature Physics*, 2(3):186–189, 2006.

[12] P. S. Burada, P. Hanggi, F Marchesoni, G. Schmid, and P. Talkner. Diffusion in confined geometries. *ChemPhysChem*, 10(1):45–54, 2009.

[13] H. Diamant, B. Cui, B. Lin, and S. A. Rice. Correlated particle dynamics in concentrated quasi-two-dimensional suspensions. *J.Phys.: Cond. Matt.*, 17(49):S4047, 2005.

[14] M. D. Carbajal-Tinoco, R. Lopez-Fernandez, and J. L. Arauz-Lara. Asymmetry in colloidal diffusion near a rigid wall. *Phys. Rev. Lett.*, 99(13):138303, Sep 2007.

[15] H. Acuña Campa, M. D. Carbajal-Tinoco, J. L. Arauz-Lara, and M. Medina-Noyola. Collective dynamics in quasibidimensional colloidal suspensions. *Phys. Rev. Lett.*, 80(26):5802–5805, Jun 1998.

[16] R. Pesché and G. Nägele. Stokesian dynamics study of quasi-two-dimensional suspensions confined between two parallel walls. *Phys. Rev. E*, 62(4):5432–5443, Oct 2000.

[17] H. A. Lorentz. A general theory concerning the motion of a viscous fluid. *Abh.Theoretical Phys*, 1(23), 1907.

[18] H. Faxen. The opposition to the motion of a rigid sphere in a viscous liquid that is trapped between two parallel plane walls (translated from german). *Ann. Physics*, 4(89), 1922.

[19] H. Faxen. The motion of a rigid sphere along the axis of a pipes filled with a liquid (translated from german). *Ark.Mat.Astron.Fys*, 1(18), 1924.

[20] H. Brenner. The slow motion of a sphere through a viscous fluid towards a plane surface. *Chem.Engr.Sci*, 16(242), 1961.

[21] A. J. Goldman, R. G. Cox, and H. Brenner. Slow viscous motion of a sphere parallel to a plane wall–i motion through a quiescent fluid. *Chem.Engr.Sci*, 22(637), 1967.

[22] E. S. Pagac, R. D. Tilton, and D. C. Prieve. Hindered mobility of a rigid sphere near a wall. *Chem. Eng. Comm.*, 148(1), 1996.

[23] D. C. Prieve, S. G. Bike, and N. A. Frej. Brownian-motion of a single microscopic sphere in a colloidal force-field. *Faraday Discussions*, 90:209–222, 1990.

[24] T. Benesch, S. Yiacoumi, and C. Tsouris. Brownian motion in confinement. *Phys. Rev. E*, 68(2):021401, Aug 2003.

[25] B. Lin, J. Yu, and S. A. Rice. Direct measurements of constrained brownian motion of an isolated sphere between two walls. *Phys. Rev. E*, 62(3):3909–3919, Sep 2000.

[26] J. Leach, H. Mushfique, S. Keen, R. Di Leonardo, G. Ruocco, J. M. Cooper, and M. J. Padgett. Comparison of faxén's correction for a microsphere translating or rotating near a surface. *Phys. Rev. E*, 79(2):026301, Feb 2009.

[27] P. Huang and K. S. Breuer. Direct measurement of anisotropic near-wall hindered diffusion using total internal reflection velocimetry. *Phys. Rev. E*, 76(4):046307, Oct 2007.

[28] P. Holmqvist, J. K. G. Dhont, and P. Lang. Colloidal dynamics near a wall studied by evanescent wave light scattering: Experimental and theoretical improvements and methodological limitations. *J. Chem. Phys.*, 126(4), 2007.

[29] N. Lecoq, F. Feuillebois, N. Anthore, R. Anthore, F. Bostel, and C. Petipas. Precise measurement of particle–wall hydrodynamic interactions at low reynolds number using laser interferometry. *Phys. of Fluids A*, 5(1):3–12, 1993.

[30] N. Lecoq, K. Masmoudi, R. Anthore, and F. Feuillebois. Creeping motion of a sphere along the axis of a closed axisymmetric container. *J. Fl. Mech.*, 585(-1):127–152, 2007.

[31] B. Cui, H. Diamant, and B. Lin. Screened hydrodynamic interaction in a narrow channel. *Phys. Rev. Lett.*, 89(18):188302, Oct 2002.

[32] X. Xinliang and A. R. Stuart. Influence of hydrodynamic coupling on the density dependence of quasi-one-dimensional diffusion. *J. Chem. Phys.*, 122(2):024907, 2005.

[33] A. Scherer and S. R. Quake. From micro- to nanofabrication with soft materials. *Science.*, 290(5496):1536, 2000.

[34] A. Unger, M., H. Chou, T. Thorsen, A. Scherer, and S. R. Quake. Monolithic microfabricated valves and pumps by multilayer soft lithography. *Science.*, 288(113):5463, 2000.

[35] H. Becker and C. Gartner. Polymer microfabrication technologies for microfluidic systems. *Analy. Bioanaly. Chem.*, 390:89–111, 2008.

[36] S. A. Vanapalli, D. Wijnperle, A. van den Berg, F. Mugele, and M. H. G Duits. Microfluidic valves with integrated structured elastomeric membranes for reversible fluidic entrapment and in situ channel functionalization. *Lab on a chip*, 10:1461–1467, 2009.

[37] A. W. M van Schijndel. Modeling and solving building physics problems with femlab. *Building and Environment*, 38:319–327, 2003.

[38] J. C. Crocker and D. G Grier. Methods of digital video microscopy for colloidal studies. *J. Coll. and Int. Sci.*, 179:298–310, 1996.

[39] E. Weeks. Idl codes for particle tracking.

[40] H. B. Eral, D. Ende van den, F. Mugele, and M. H. G. Duits. Influence of confinement by smooth and rough walls on particle dynamics in dense hard-sphere suspensions. *Phys. Rev. E*, 80(6):061403, 2009.

[41] Y. Li. *Linking particle dynamics to intracellular micromechanics in living cells.* PhD thesis, Enschede, November 2009.

[42] T. Savin and P. S Doyle. Static and dynamic errors in particle tracking microrheology. *Biophys. J.*, 88(1):623–638, 2005.

[43] P. Lanson, G. Batrouni, L. Lobry, and N. Ostrowsky. Drift without flux: Brownian walker with a space-dependent diffusion coefficient. *EPL*, 54(1):28, 2001.

5 Effect of roughness on confined concentrated suspensions

Abstract Diffusion in colloidal hard sphere suspensions near a rough wall as a function of volume fraction is studied by observing a sedimenting suspension on a surface with well-defined roughness using video microscopy and particle tracking. The rough substrate was prepared by sintering a sparse monolayer (area fraction (Θ) ≈ 0.4) of silica particles (diameter:1.2 μm) onto an initially flat glass wall. The suspension consisted of silica spheres (diameter:1.5 μm). The effect of the wall roughness was assessed by comparing the experiment on rough surface to a control experiment carried out on a flat "uncoated" wall. The mean squared displacements (MSDs) at the rough surface had consistently smaller amplitudes (A) and exponents (α) than those at the smooth substrate both as a function of time and volume fraction. At the rough wall, a coexistence of diffusive-like motions ($\alpha \approx 1$) and cage rattling ($\alpha \approx 0$) is observed whereas at the smooth surface an unipolar α distribution is encountered. As the volume fraction increases a gradual transition from diffusive to subdiffusive ($\alpha \approx 0.5$) behavior is observed for the smooth surface. For the rough surface, the bipolar distribution evolves from a predominantly diffusive to predominantly cage rattling ($\alpha \approx 0$). We attribute this different behavior firstly to a combination of static and dynamic caging, and secondly to the different 3D structure of the suspension near the rough wall.

5.1 Introduction

Diffusion of a single particle in the vicinity of a flat solid boundary is a classic, "ideal case" problem first studied by Lorentz [1, 2, 3, 4]. However, conditions in real life are rarely that ideal. Many naturally occurring substrates such as rock surfaces, cell membranes , human skin and hair can be highly irregular at microscopic length scales. Furthermore, also particle suspensions in contact with real life surfaces are often found to be far from dilute, for instance blood, milk, paint or flowing slurries. Hence the case of a suspension at high volume fraction near a rough surface presents a much more complex picture.

From the application perspective, understanding the dynamics of colloidal particles in the vicinity of rough walls could shed light on various processes of industrial relevance such as corrosion, colloidal epitaxy, fouling and clogging at rough walls in (micro) channels. Also from a fundamental point of view the problem is interesting. The influence of wall roughness on diffusion-related physical phenomenon such as friction [5], aggregation [6], adsorption [7, 8], fouling or caking, reaction and transport through porous media [9, 10] has been studied for various soft matter systems such as colloids [11], proteins [12], polymers [13] and biological systems [14]. Recently, roughness has also been utilized for manipulating colloidal interactions [15, 16, 17].

Roughness is a phenomenon, that can occur on different length scales relative to particle size of the suspension. How roughness influences the relevant physical phenomenon, therefore depends on the details and type of roughness. For the case of diffusion in quiescent fluids, several questions can be posed. An important one is: does roughness speed up or slow down the diffusion of nearby particles? From an intuitive point of view, depending on the characteristic size of roughness relative to particle diameter, one could consider a rough layer either as a porous medium that enables solvent to flow through its pores or additional boundaries. This could indeed alter the hydrodynamic forces on particles that move near the wall. On the other hand, the irregularities introduced by the roughness could also increase dissipation. Furthermore, it is known that roughness can also

influence the equilibrium structure of the colloidal fluid near the wall, making it less dense but also less ordered. What will be the net effect hereof on the particles dynamics cannot be said a priori.

Experimental and simulation studies in the last decade have shed some light on these issues, although only few studies were actually aimed at the diffusive behavior near a single rough surface. The diffusion coefficient near a smooth surface has been studied as a function of volume fraction by Light scattering techniques [18]. In the vicinity of a rough wall, diffusion in a dense suspension brings out additional effects such as many-body hydrodynamics and structure due to crowding. Also suspensions that were confined between two surfaces have been studied. Several authors found that the volume fraction dependent dynamics and phase behavior of colloidal hard spheres [19, 20, 21, 22, 23] can change profoundly under the influence of additional confining boundaries [24, 25, 26, 27, 28, 29]. For example, the structure in the vicinity of a wall was found to show layering behavior analogous to confined molecular liquids. Mixed findings were obtained for the effect of rough walls on the dynamics. For a confined (bidisperse) system it was found that particles which stick to a wall, slow down the dynamics of mobile particles in their immediate vicinity [11]. In a previous study from our group, roughness and gravity has been found to play a role on dynamics of concentrated colloidal suspensions yet influence of two effects could not be isolated [27].

Despite this progress, a lot still remains unknown about the influence of the roughness of a single wall on local particle dynamics. In particular it would be important to know, how the influence of roughness on dynamics depends on the concentration of the suspension and the characteristic length scale of the roughness compared to that of the suspended particles.

In the present study we contribute to this field by studying the dependence of the diffusive behavior at a rough wall as a function of the suspension concentration. The latter is varied by letting suspended particles slowly settle to the surface, and meanwhile measuring the dynamic in the vicinity of a rough wall. The time dependence of the corresponding concentration is measured during short interruptions of measurements. Performing a similar experiment with a smooth

substrate allows to asses the effect of the roughness.To define the rough substrate, we have chosen to coat a smooth wall with a monolayer of particles that have a comparable size to those in the suspension. This monolayer has an intermediate density with a significant amount of vacancies. While this is of course a particular case of roughness, it resembles the scenario of fouling. Moreover we also visualized both the immobilized and the suspended particles at the surface. This allowed us to correlate the local dynamics to the local surroundings of the particles.

5.2 Experimental methods

5.2.1 Substrate preparation

The sample chambers are prepared by gluing a glass tube on to 0.170 μm thick glass slides. For the smooth substrate we used a glass coverslip, which was flat down to the nm scale [27]. The rough substrate was prepared by spincoating a colloidal suspension on a glass coverslip and letting the solvent evaporate. The sintered particles were 1.2 μm diameter (d_s) Rhodamin labeled silica spheres with a polydispersity of 8%. After suspending them in a 40:30:30 mixture (by weight) of water, ethanol and ethylene glycol up to a volume fraction of, 15% 1 mL of the suspension was spincoated at a rate of 2000 rpm for a duration of 30 s. Due to the solvent evaporation, the particles stick to the glass. Drying for 30 min in an oven at 200 $\circ C$ served to remove the last traces of solvent, and sinter the particles to the glass (with this recipe the coverage density can be adjusted via the ratio of water to ethylene glycol). The area fraction of colloidal particles is 0.4. The area fraction (Θ = 0.4) is defined as the ratio of total projected area of sintered particles divided by the total area in the field of view. Total projected area of sintered particles is calculated by multiplying the total number of sintered particles by projected area on a sintered particle.

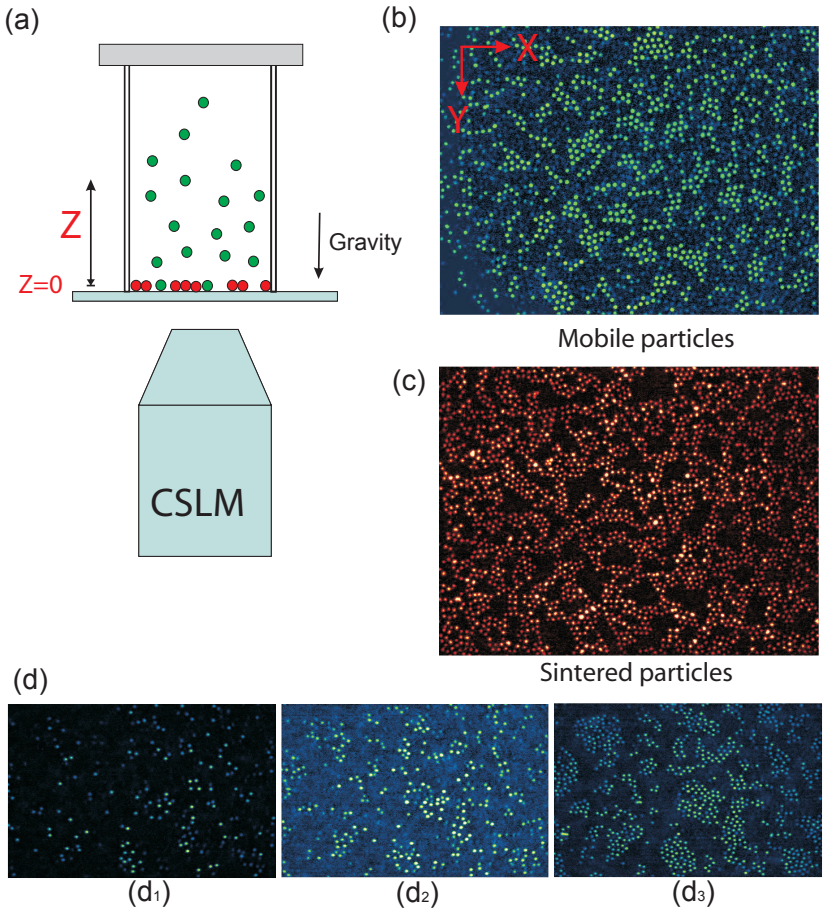

Figure 5.1: Panel (a) is a schematic of the experiment where the mobile (green) and the sintered (red) particles can be seen. The Panel (b) and Panel (c) show complementary confocal images of the mobile and sintered particles that are present in the same layer . Panel (d) illustrates the sedimentation of the sample via confocal images taken at different time frames (t=0s (d_1), 100s (d_2), 2000s (d_3)).

5.2.2 Colloidal suspensions

Fluorescein labeled silica particles of 1.5 μm diameter((d_p)) (MicroMod GmbH) with 5% polydispersity and a mass density of 1.8 g/mL were suspended in mixture, containing either water and glycerol (30:70 by weight) or water and DMSO (19:81 by weight). This allowed particle visualization deep into the suspension. The relatively high viscosity of the glycerol containing mixture helped to slow down gravity settling without diminishing the diffusive displacements too much (see Sec. 5.2.4). This provided a bigger time window to study the evolution of the structure and the dynamics while the local density of the fluid at the surface was increasing. Prior to each experiment, a small amount of stock suspension (volume fraction ϕ = 0.01) was sonicated and subsequently diluted with a relatively large amount of solvent mixture to reach a final ϕ = 0.02. The solvent also contained 100 μM LiCl, corresponding to an electric double layer thickness of 30 nm. This gave interparticle electrostatic repulsions that were strong enough to maintain colloidal stability and with a range that was still very small compared to the particle size.

5.2.3 Confocal Microscopy

Images were recorded with an UltraView LCI10 CSLM system (Perkin Elmer) consisting of a Nikon Eclipse inverted microscope, a Yokogawa (Nipkov disk) confocal unit and a Hamamatsu 12-bit CCD camera. All recordings were done in fluorescence mode using 25 mW lasers with wavelength of either 488 or 561 nm and a 100X/oil objective with NA=1.3. The pixel size corresponding to the images was 0.135 μm. All microscopy experiments were performed at 22± 2^{o}C with suspensions in capped bottles, of which the bottom had been taken out and replaced by the (smooth or rough) substrate (see Fig. 5.1). In case of a rough substrate, first an image was made of the rhodamin labeled spheres that had been sintered to the bottom, using the 561 nm laser line. Hereafter the 488 nm line was selected to image Fluorescein labeled spheres. Immediately after filling the holder with the suspension, Z-stacks and time-series (typically 6 of each) were recorded in alternating fashion, for a total duration of about 1

hour. Z-stacks were recorded up to Z=20 μm in steps of 0.1 μm at 0.2 s per image. Time series were recorded for typically 2000 images at either 1 or 5 frames per second. Here the Z-location was fixed at 0.75 μm above the glass bottom, corresponding to the radius of the suspended particles.

5.2.4 Particle tracking

The image analysis is based on the accurate localization and tracking of particles by the algorithm from Crocker and Grier implemented in IDL. The 'effective focal depth' relevant for particle tracking was estimated to be 2.0 μm from an intensity-vs.-Z scan of a particle that was stuck to the bottom. The images were processed via the available particle tracking codes in 2D and 3D. The accuracy of locating the centroid of particles in 3D was 0.02 μm in X-Y and 0.05 μm in the Z direction. Particle trajectories in the XY-plane were converted into the mean squared displacement $\langle r^2 \rangle$ as a function of lag time τ. Unless mentioned otherwise, the MSDs for the individual particles were lumped together into an average MSD function that was representative for all particles present at the time of interest.

To study the dependence of $\langle r^2(\tau) \rangle$, on the real time t (the time lapse after starting the experiment), image-time series were divided into segments of 100 frames (corresponding to 20 s each), to represent time 'points'. Given that the number of particles per image was O(100-1000), this gave an acceptable trade-off between the time resolution and the statistical accuracy of the MSD. For each time segment t, the first 10 points of the MSD were fitted to a power law: $\langle r^2(\tau) \rangle = A(\frac{\tau}{\tau_0})^\alpha$ with A the amplitude and t_0 the unit exposure time. A and α provide complementary information on respectively the displacement magnitude and the type of motion.

5.3 Results and discussion

As the mobile particles in the container settle due to gravity, we follow the dynamics and the structure of the suspension at the bottom surface as a function of time. The first observation is that the mag-

nitude of the MSD decreases gradually over time and tends towards a plateau, for both surfaces (see Fig. 5.2a). Clearly, this is due to the increased crowding at the surface as the sedimentation proceeds. Similar graphs of MSDs versus time were also found in additional experiments in water-DMSO mixtures (not shown). Importantly, the MSD amplitudes were found to be lower near the rough surface at all times. The slight increase in the MSD for $\tau = 0.2$ s at the rough wall occurring for $t > 1500$ s is ascribed to photobleaching. The latter process was indicated by a slight drop in the number of detected particles after it had reached a plateau (not shown). Typically the particles that have the longest residence time in the focal plane are the ones that have the smallest MSDs. Failure to detect these slow particles then results in an increase of the average MSD.

Also the nature of the diffusion was studied as a function of time by monitoring the exponent (α) obtained from the MSD at short lagtimes (see Sec. 2.4). The initial α of 1.0 at the smooth substrate suggests a diffusive (i.e. Brownian) behavior. Remarkably, for the rough surface the initial exponent is found ≈ 1.0 as well. This is ascribed to the arrival of individual mobile particles at the relatively large open areas of the virginal rough substrate (see Fig. 5.1c); in this case the mobile particles hardly feel the presence of the sintered particles. As the crowding increases, the exponent becomes sub-diffusive for both the rough and smooth surfaces, indicating a trend towards caging. Interestingly, the exponent decreases more quickly at the rough surface and remains lower at all times. Also a different rough substrate having a similar surface coverage by sintered particles, but with a smaller typical length of the open areas was explored. Here the same qualitative trend for α was found, but with an initial $\alpha \approx 0.5$ (result not shown).

Clearly, the changing characteristics of the particle dynamics must be related to the local structure and density of the fluid, which evolve as the sedimentation proceeds. To study this relation in more depth, we recorded (fast) Z-scans in between the MSD measurements and used these scans to localize all suspended particles in 3 dimensions. Anticipating the formation of structures that are layered in the Z-direction, we calculated density-vs-Z profiles by convoluting each particle center with a sphere corresponding to the average particle

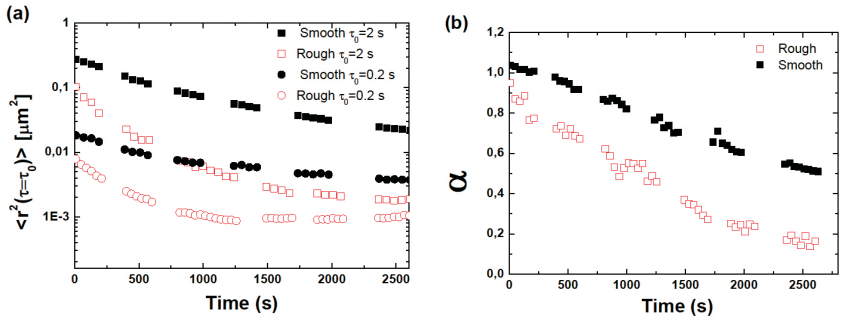

Figure 5.2: Magnitude at two different lag times (Panel(a)) and exponent (Panel (b)) of the Mean Squared Displacement function measured at the smooth and rough walls. All particle motions were measured parallel to the wall while keeping the optical focus fixed at $Z = d_p/2$ throughout the sedimentation process. The noise floor is approximately $1 * 10^{-4} \mu m^2$.

volume of the distribution. Subsequently we calculated in successive thin Z-slices, which fraction of the slice volume was occupied by particles (as in [27]). In case of the rough substrate, also the sintered particles were taken into account. The resulting 'local solid volume fraction (ϕ_l)' profiles are shown in Fig. 5.3.

The first observation is that on both substrates a steadily growing thin layer of mobile particles is formed. This is in qualitative agreement with expectations based on a simple picture, in which all particles sediment independently, and with a steady velocity that is dictated by equilibrium between buoyancy and drag forces. Knowing the particles' radius and mass-density, the solvent viscosity and the initial suspension volume fraction, we calculated the particle arrival rate (per unit area) at the substrate. The data shown in Fig. 5.3 were found to be in reasonable agreement with this calculation. However, a quantitative correspondence was not found, and also the growth rate of the layer above the rough substrate turned out to be somewhat lower as compared to the smooth substrate.

Such a lack of quantitative correspondence was also found in an earlier study [30]. It might suggest that the description of the sedimentation process was too simplistic, and should perhaps not be

applied to the formation of thin layers at an impermeable bottom substrate. Alternatively also the softness of the thin layer may have played a role: since it is held together by weak forces, even small mechanical disturbances could exert an influence on the layer. This issue would require further study, which is beyond the scope of the present paper.

On the other hand, the semi-quantitative agreement with the model also indicates that the thickness and density of the layer, as well as the rate of change thereof, can be controlled by the experimentalist. We remark here that sediments at intermediate densities ($0.2 < \phi_l < 0.5$) are generally difficult to achieve without making thin layers. This follows from the sedimentation equilibrium for hard spheres, in which the (local) value of ϕ_l in a sediment layer is dictated by equality between the gravity force exerted by the layer above, and the osmotic pressure.

A second observation after comparing Figure 5.3a and 5.3b, is that the degree of ordering in the layer is influenced by the roughness. Clearly the well-known layering effect occurring at the smooth substrate [31] is disturbed by the sintered particles. Also the packing of spheres occurs less efficiently as compared to the smooth surface. This is ascribed to frustrated order: in general a bidisperse particle mixture can be packed more efficiently. However in our case the smaller particles are fixed to the surface, which limits the possibilities for optimizing the packing.

These differences in the structure and density of the layer on top of the smooth and rough surfaces indicate that analyzing the particle dynamics at the two surfaces as a function of the time lapsed after starting the experiment, may not provide the most suitable basis for comparison. Alternatively, one could also analyze the particle dynamics at the smooth and rough substrates by comparing MSDs at the same (local) volume fraction. But then the question arises, how to define the effective volume fraction that is felt by the particles. In other words, what would be the best definition of the 'surface layer'?.

In the present study, the roughness features have length scales that are very similar to the size of the mobile particles. This might justify the choice of a layer that is centered at one (mobile-) particle radius above the cover slip. In this scenario, the surface layer of the

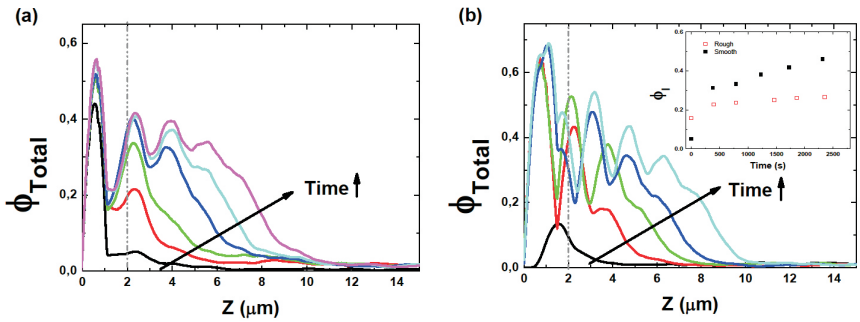

Figure 5.3: Local 'solid volume fraction' profiles as a function of the time lapsed after starting the experiment. The time points where a Z-stack was shot are marked in Fig. 5.2. Panel (a): rough substrate. Panel (b): smooth substrate. The inset shows the time dependence of the calculated volume fraction in the particle layer closest to the wall. See text for further details.

rough substrate is already crowded from the beginning, due to the sintered particles. However the choice of a 'mathematical' location, strictly at $Z = 0.5dp$ would not be suitable for comparison with the experiments. To allow the latter, a finite thickness should be assigned to the surface layer, to take into account both the Z-resolution of the optical detection, and the geometrical aspect that a particle with its center located at $Z = 0.5dp$ can still collide with other mobile particles having their center at $Z < 1.5dp$. These considerations were taken into account (in an approximate manner) by averaging the volume fraction profiles in Fig. 5.3 between Z=0 and 2.0 μm. The resulting values for the 'surface volume fraction' ϕ_l are shown in the inset of Fig. 5.3.

Plotting the MSD amplitude and exponent now as a function of ϕ_l results in Fig. 5.4. Clearly, both the magnitude and the exponent of the MSD show distinct behaviors for the smooth and rough surfaces. In both sub figures, the data at the different substrates do not intersect (or even reach a common point) at any of the accessible ϕ_l values, despite the considerable error bar in ϕ_l (to take into account the particle polydispersity and the uncertainty in the upper

integration boundary of Z). This clearly points out that specifying ϕ_l is not sufficient to capture the differences in dynamics at the two substrates. Apparently, other aspects besides crowding must play a role too.

We note that the closest correspondence between the diffusive exponents at the two substrates is found at high ϕ_l. This is indicated by the data point at $\phi_l \approx 0.5$, which was obtained from an additional experiment with a thick sediment layer. This outcome could be rationalized from a conceptual picture of 'composite confinement'. In this picture, each mobile particle at a surface is confined vertically by bare surface, and in the case of the rough surface also horizontally by the fixed particles. Besides these immobile boundaries, also the other mobile particles can contribute to caging of the central particle. Thus one could speak of a cage which is partially static and partially dynamic. Here the dynamic part of the cage 'opens and closes' due to the motions of the mobile particles (as in the bulk fluid). Then at high particle densities (close to the glass transition) two conditions occur: 1. the vacancies in the rough layer are most efficiently filled by particles from the suspension, making the packing fraction similarly high as near the smooth substrate, and 2. at both substrates the mobile particles are caged from all sides.

A more detailed comparison of the particle dynamics at the smooth and rough substrates was made by analyzing the trajectories of the individual particles for their amplitude (A) and exponent (α) of the MSD at short lag times. Histograms of these quantities were obtained as follows: for each of the 6 time blocks per substrate (see Fig. 5.2), only the first 300 time frames were considered (to define the "time point" more sharply). Dividing these into 3 subblocks of 100 consecutive frames, each particles present within a given sub block for more than 50 frames were analyzed for its A and α. Depending on the substrate and the lapsed time (i.e. progress of the sedimentation), this resulted in 500-2500 contributions to the histogram.

The results shown in Fig. 5.5 show that the exponent distributions look strikingly different for the two substrates. For the smooth substrate, the histogram appears to be Gaussian shaped with an expectation value that shifts from 1.0 to 0.5. In contrast, for the rough substrate a bimodal distribution is found, with peaks at $\alpha \approx 1.0$ and

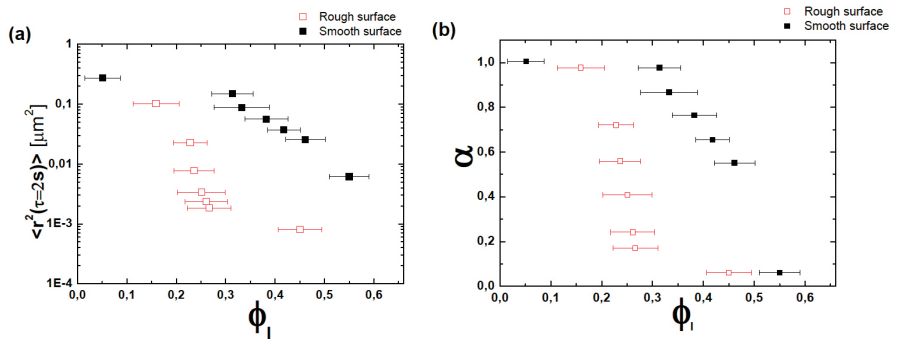

Figure 5.4: Panel (a) MSD at a given time lag of 2 seconds versus calculated local volume fractions (θ_l) for smooth & rough surfaces, Panel (b) α vs (θ_l) for smooth & rough surfaces (also including the thick sediment layer samples; the latter experiment is indicated by triangular symbols)

$\alpha \approx 0.0$. Over the course of time, the distribution between the peaks changes from dominated by $\alpha \approx 1.0$, to one dominated by $\alpha \approx 0.0$. The amplitude A appeared to be correlated to α : lower exponents generally corresponded to lower amplitudes (not shown). This suggests that roughly speaking two types of behavior occur on the rough substrate: free diffusion and caged diffusion. Finally we remark that the occurrence of seemingly unphysical values of α (< 0 or > 1) is due to the finite number (i.e. 50-100) of observations that was used to obtain each individual particle MSD. This has also been found and explained in earlier studies [32, 33].

Now the question is, how to understand that some particles near the rough substrate show a type of motion that is close to 'cage rattling', whereas other particles appear to diffuse freely in the horizontal direction. Therefore we inspected our movies for correlations between the type of dynamics and the geometry of the horizontal cage (formed by the sintered particles). This type of analysis has been described [33] and is here repeated only briefly. First each movie was segmented into units of 100 time steps. Then for each sufficiently long (50-100 steps) particle trajectory in the movie, A and α were calculated by fitting to the equation given in Sec.5.2.4. Based on the distribution of α, a color scale was defined to highlight the different

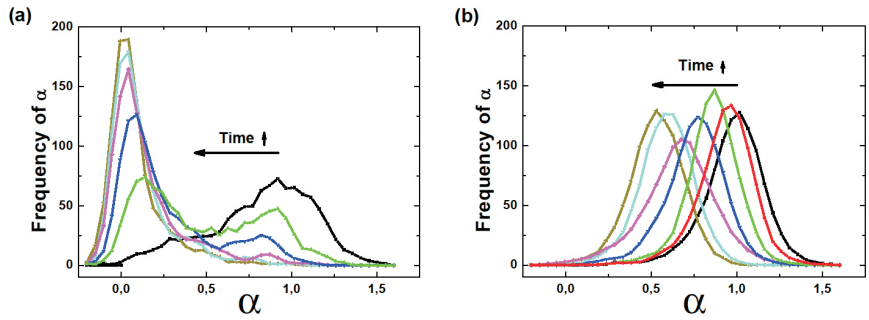

Figure 5.5: Exponent histograms as a function of time for diffusing particles at the rough (Panel (a)) and smooth (Panel (b)) substrates. Times and colors correspond to those in Fig. 5.3.

behaviors. Finally the particles were plotted at the average location of their trajectory (fragment) along with their color. In the present study where crowding is an important element, the analysis was extended by also representing the size of each particle. Fig. 5.6 shows the results of this operation for three different stages of the experiment: a) the very beginning, b) the second time-series, in which the distinctive dynamic behaviors coexisted the most (see Fig. 5.5) and c) the end.

The first observation from Fig. 5.6a, b and c is that there is hardly any overlap between the locations of sintered and mobile particles. This corroborates that the majority of mobile particles was detected directly above the glass coverslip (as intended). Clearly, the few cases of mobile particles that show overlap with sintered particles (and thus must reside on top of them) are not responsible for the rattling dynamics ($\alpha \approx 0.0$) observed in any of the three images.

At the start of the experiment (Fig. 5.6a) the motion of the particles at the surface is minimally influenced by the occurrence of particles in the adjacent layer above, since the concentration in that layer is still rather low (see Fig. 5.3). As expected, most particles show an exponent $\alpha \approx$, especially in the most extensive bare areas. The relatively few cases of subdiffusive behavior are mainly found in

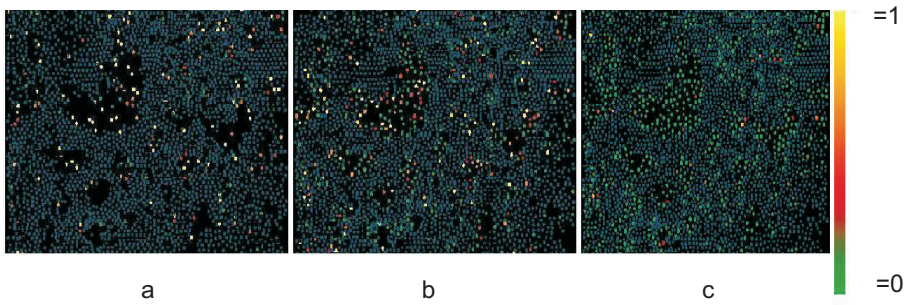

Figure 5.6: Analysis of correlations between the type of dynamics (expressed by the exponent α fitted to the MSD at small lag times) and the geometrical surrounding provided by other particles. Figures a, b and c show reconstructed images of mobile and sintered particles at the rough substrate, taken from the time series 1, 2 and 6 (Fig. 5.2). Sintered particles are indicated in dark blue. Mobile particles are color-coded according to their diffusive exponent (see Fig 5b for the histogram). To further emphasize the different behaviors, all $\alpha < 0.4$ were set to 0 and all $\alpha > 0.8$ to 1. The color bar represents a linear scale from 0.0 (cyan) to 1.0 (yellow)

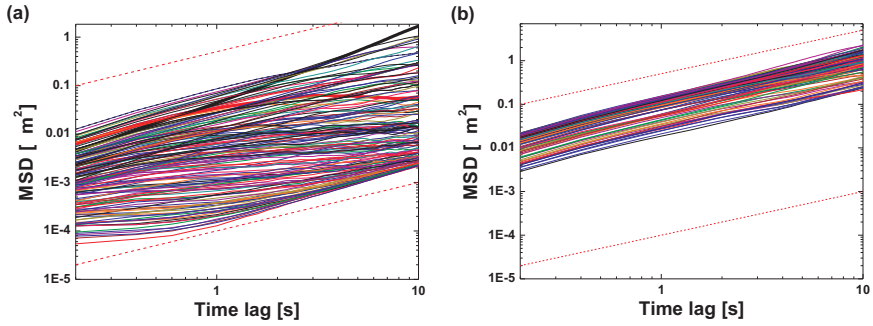

Figure 5.7: Individual MSDs of particles at the rough (Panel (a)) and the smooth substrate (Panel (b)) at the start of the experiment. Most of the MSDs have an initial exponent close to 1.0, indicating diffusive behavior. At longer lag times also some MSDs develop a plateau, indicative of caging. In both graphs the dashed red lines correspond to $\alpha = 1$.

the more narrow confinements. We remark here that the appearance of this map will generally depend on the lag time at which α is measured: the longer the lag time, the more area can be explored by the diffusing particles. Eventually this should reveal the horizontal confinements presented by the sintered particles (at least for a fraction of the mobile particles).

To examine this, we extended the analysis range of the first movie to the first 500 frames thereof, and calculated individual MSDs (iMSDs) up to lag times of 200 time steps. Plotting the iMSD functions in one graph results for rough and smooth surfaces resulted in Fig. 5.7a and Fig. 5.7b respectively. Interestingly, for the rough surface (Fig. 5.7a) some MSDs show initially a diffusive behavior, and evolve to a plateau for longer lag times whereas for smooth surface almost exclusively diffusive behavior is observed. These iMSDs, highlighted in Fig. 5.7a corroborate that horizontal confinement due to the fixed particles does indeed occur. Also the magnitudes of the MSD plateaus appear to be consistent with the available length scales for horizontal confinement. We remark that above a certain length scale, the confinement length can no longer be measured from the MSD, because the typical time for a particle to reach the horizontal boundaries is longer than the typical time needed to move vertically to another focal plane.

In Fig. 5.6b the number of particles with $\alpha \approx 0$ (at short times) has clearly grown. Apparently many particles that appear to have a large area available for diffusion, are in fact already caged. Moreover the magnitude of the MSD (shown in Fig. 5.6) suggests a typical cage length that is smaller than the observable distances between the particles in the focal plane. This implies that horizontal confinement by other particles in the layer just above the focal plane (invisible in Fig. 5.6b) must already play a role in this experiment. In Fig. 5.6c almost all mobile particles at the surface have become caged, and consequently also the correspondence between the type of motion and the local surroundings by either mobile or fixed particles has become lost. This is consistent with a caging by the particles that are present in the (now crowded) layer above the focal plane.

Taking the foregoing observations together, the following mechanistic picture emerges: particles that have arrived at uncovered areas

of the substrate, are mostly kept in the surface layer because of gravity. Hence they will perform essentially a surface diffusion, characterized by a linear time dependence of the MSD. This type of motion changes into sub-diffusive when obstacles are met. These obstacles can be either static (due to fixed particles) or dynamic (due to other mobile particles, occurring either in the surface layer as well, or just above it). As the number of particles arriving at the surface grows, the hydrodynamic interactions with other mobile particles increase strongly, and begin to dominate. However, the effect of the presence of the sintered particles never becomes wiped out completely.

5.4 Conclusions and Outlook

We compared the dynamics of colloidal hard spheres at a smooth and a rough wall as a function of the local suspension volume fraction at the surface. A special case considered in the present study was that the roughness was provided by sintered particles with a similar size as the suspended particles. Our main finding was that the in-plane mean squared displacement function was always smaller at the rough substrate. This difference became apparent through both the amplitude and the initial exponent of the MSD. While this difference occurred for all suspension concentrations, it tended to become smaller in the limit of very dense packing. These findings can be qualitatively understood from the additional caging effect of the sintered particles. As the suspension concentration is increased, the caging becomes dominated by the mobile particles. However even in this scenario the sintered particles remain of importance. This is ascribed their indirect effects on the structure and dynamics of the suspended particles. These outcomes have implications for different types of structure formation at surfaces, varying from the progression of particulate fouling of surfaces, to clogging of flow channels, to template guided colloidal assembly.

5.5 Acknowledgements

We would like to thank Dirk van den Ende for fruitful discussions, Jolet de Ruiter for preparation of particle coated glass slides. Eric Weeks is acknowledged for providing particle tracking software. We thank the Chemical Sciences division of the Netherlands Organization for Scientific Research (NWO-CW) for financial support (ECHO grant).

Bibliography

[1] H. A. Lorentz. A general theory concerning the motion of a viscous fluid. *Abh.Theoretical Phys*, 1(23), 1907.

[2] H. Faxen. The opposition to the motion of a rigid sphere in a viscous liquid that is trapped between two parallel plane walls (translated from german). *Ann. Physics*, 4(89), 1922.

[3] H. Faxen. The motion of a rigid sphere along the axis of a pipes filled with a liquid (translated from german). *Ark.Mat.Astron.Fys*, 1(18), 1924.

[4] H. Brenner. The slow motion of a sphere through a viscous fluid towards a plane surface. *Chem.Engr.Sci*, 16(242), 1961.

[5] O. I. Vinogradova and G. E. Yakubov. Surface roughness and hydrodynamic boundary conditions. *Phys. Rev. E*, 73(4):045302, 2006.

[6] S. Y. Shulepov and G. Frens. Surface roughness and the particle size effect on the rate of slow, perikinetic coagulation. *Journal of Colloid and Interface Science*, 170(1):44 – 49, 1995.

[7] Z. Adamczyk, B. Siwek, and E. Musia,. Kinetics of colloid particle adsorption at heterogeneous surfaces. *Langmuir*, 17(15):4529–4533, 2001.

[8] M. Shimada, K. Okuyama, Y. Kousaka, and J. H. Seinfeld. A model calculation of particle deposition onto a rough wall by brownian and turbulent diffusion. *Journal of Colloid and Interface Science*, 125(1):198 – 211, 1988.

[9] K. Malek and M. Coppens. Effects of surface roughness on self- and transport diffusion in porous media in the knudsen regime. *Phys. Rev. Lett.*, 87(12):125505, Aug 2001.

[10] S. Russ, S. Zschiegner, A. Bunde, and J. Karger. Lambert diffusion in porous media in the knudsen regime: Equivalence of self-diffusion and transport diffusion. *Phys. Rev. E*, 72(3):030101, Sep 2005.

[11] K. V. Edmond, C.R. Nugent, and E. R. Weeks. Influence of Confinement on Dynamical Heterogeneities in Dense Colloidal Samples. *arXiv:1003.0856*, Mar 2010.

[12] K. Rechendorff, M. B. Hovgaard, M. Foss, V. P. Zhdanov, and F. Besenbacher. Enhancement of protein adsorption induced by surface roughness. *Langmuir*, 22(26):10885–10888, 2006.

[13] J. F. Douglas. How does surface roughness affect polymer-surface interactions? *Macromolecules*, 22(9):3707–3716, 1989.

[14] K. Shellenberger and B. E. Logan. Effect of molecular scale roughness of glass beads on colloidal and bacterial deposition. *Environmental Science & Technology*, 36(2):184–189, 2002.

[15] J. Y. Walz. The effect of surface heterogeneities on colloidal forces. *Advances in Colloid and Interface Science*, 74(1-3):119 – 168, 1998.

[16] K. Zhao and T. G. Mason. Directing colloidal self-assembly through roughness-controlled depletion attractions. *Phys. Rev. Lett.*, 99(26):268301, Dec 2007.

[17] M. Kostoglou and A. J. Karabelas. Effect of roughness on energy of repulsion between colloidal surfaces. *Journal of Colloid and Interface Science*, 171(1):187 – 199, 1995.

[18] V. N. Michailidou, G. Petekidis, J. W. Swan, and J. F. Brady. Dynamics of Concentrated Hard-Sphere Colloids Near a Wall. *Phys. Rev. Lett.*, 102(6):068302, 2009.

[19] P.N. Pusey and W. van Megen. Phase behaviour of concentrated suspensions of nearly hard colloidal spheres. *Nature*, 320(27):340–342, 1986.

[20] E. R. Weeks, J. C. Crocker, Andrew C. Levitt, Andrew Schofield, and D. A. Weitz. Three-Dimensional Direct Imaging of Structural Relaxation Near the Colloidal Glass Transition. *Science*, 287(5453):627–631, January 2000.

[21] E. R. Weeks and D. A. Weitz. Properties of Cage Rearrangements Observed near the Colloidal Glass Transition. *Phys. Rev. Lett.*, 89(9):095704, Aug 2002.

[22] E. Zaccarelli, C. Valeriani, E. Sanz, W. C. K. Poon, M. E. Cates, and P. N. Pusey. Crystallization of Hard-Sphere Glasses. *Phys. Rev. Lett.*, 103(13):135704, Sep 2009.

[23] M. Hermes and M. Dijkstra. Thermodynamic signature of the dynamic glass transition in hard spheres. *Journal of Physics: Condensed Matter*, 22(10):104114, 2010.

[24] R. P. A. Dullens and W. K. Kegel. Reentrant Surface Melting of Colloidal Hard Spheres. *Phys. Rev. Lett.*, 92(19):195702+, May 2004.

[25] C. R. Nugent, K. V. Edmond, H. N. Patel, and E. R. Weeks. Colloidal glass transition observed in confinement. *Phys. Rev. Lett.*, 99(2), 2007.

[26] P. S. Sarangapani and Y. Zhu. Impeded structural relaxation of a hard-sphere colloidal suspension under confinement. *Phys. Rev. E*, 77(1), 2008.

[27] H. B. Eral, D. van den Ende, F. Mugele, and M. H. G. Duits. Influence of confinement by smooth and rough walls on particle dynamics in dense hard-sphere suspensions. *Phys. Rev. E*, 80(6):061403, 2009.

[28] M. Hermes and M. Dijkstra. Jamming of polydisperse hard spheres: The effect of kinetic arrest. *EPL (Europhysics Letters)*, 89(3):38005, 2010.

[29] H. B. Eral, J. M. Oh, D. van den Ende, F. Mugele, and M. H. G. Duits. Anisotropic and hindered diffusion of colloidal particles in a closed cylinder. *Langmuir*, 26(22):16722–16729, 2010.

[30] V. I. Uricanu and M. H. G. Duits. Micromechanical behavior of adhesive granular silica layers:? structure deformation. *Langmuir*, 22(18):7783–7792, 2006.

[31] C. Murray. Phases of thin colloidal layers. *MRS Bulletin*, 23(10):33–38, OCT 1998.

[32] Y. Li, S. A. Vanapalli, and M. H. G. Duits. Dynamics of ballistically injected latex particles in living human endothelial cells. *Biorheology*, 46(4):309–321, 2009.

[33] M. H. G. Duits, Y. Li, S. A. Vanapalli, and F. Mugele. Mapping of spatiotemporal heterogeneous particle dynamics in living cells. *Phys. Rev. E*, 79(5):051910, May 2009.

6 Dynamic suppression of Coffee stain effect

Abstract When a drop of a suspension evaporates on a solid surface, a dense, ring-like residue so called "Coffee Stain" (CS) remains along the contact line. Deegan et al. [1] showed in a seminal study that this effect arises from a combination of two phenomenons: the contact line pinning and the radial flow induced by the evaporation of the drop. This scenario suggests that the form of the CS patterns can be controlled by manipulating the internal flows and the extent of the contact line pinning. Using electrowetting (EW), both inhibition of contact line pinning and manipulation the flow patterns are achieved simultaneously leading to suppression of CS effect. The EW induced internal flow patterns counteract the evaporation induced radial flow and also mix the drop contents. We applied our noninvasive method to various suspensions of colloidal particles and DNA solutions. Our findings have immediate bearings on diverse fields ranging from combinatorial analysis of biomolecules to crystallization of colloidal assemblies and inkjet printing of polymeric displays.

6.1 Introduction

Evaporating drops of colloidal suspensions and solutions of non-volatile species leave behind ring-like solid residues along the contact line [1]. This coffee stain effect - named after the most widely known representative of this class of structures - leads to an undesired inhomogeneous distribution of solutes, commonly encountered in coating and printing applications involving volatile solvents. Combinatorial analysis methods such as fluorescent microarrays [2, 3, 4] and MALDI-MS [5, 6, 7] are specific examples where the inhomogeneity of the residual deposits compromises the overall performance of a system. In other applications capillarity-driven assembly of colloidal and macromolecular species upon solvent evaporation can also be desirable to generate surface patterns [8, 9, 10, 11, 12, 13].In a seminal work, Deegan et al. [1] pointed out that the physical origin of the coffee stain effect is due to a combination of pinning of the three-phase contact line and a convective flux driven by the evaporation. In the present communication, we demonstrate that the formation of coffee stains can be suppressed by applying electrowetting (EW) with an alternating (AC) voltage to an evaporating drop. For optimized AC frequencies in the range of a several tens of Hz to a few kHz, the residue of a typical millimeter-sized drop consists of a single, small, homogeneous spot of the solute rather than the irregular coffee stain.

To understand the success of EW in suppressing coffee stains, we first recapitulate the various evaporation scenarios of sessile drops. For perfectly flat surfaces without any contact angle hysteresis drops evaporate at constant contact angle: as solvent evaporates, the surface of the drop (including the three phase contact line) simply recedes according to the amount of mass lost to the vapor phase. In this case non-volatile solutes collect in a single spot, i.e. without leaving behind a coffee stain. In the more frequent situation of finite contact angle hysteresis, however, the contact line is pinned at defects and cannot recede as solvent is lost due to evaporation. Mass conservation therefore requires that additional solvent is transported from the center of the drop towards the contact line. This flux transports more solute towards the contact line. The resulting local increase in solute concentration can lead to an enhanced viscosity and/or to pre-

cipitation of the solute. The precipitated solute further enhances the pinning forces and it ultimately forms the solid residue that constitutes the coffee stain (see Fig. 1). Depending on the initial contact angle hysteresis and the rate at which the pinning forces increase, the contact line either remains stuck during the entire evaporation process or displays a stick-slip motion involving one or more pinning-depinning cycles [14, 15].

The drops considered here, aqueous colloidal suspensions (0.05% vol) of fluorescently labeled polystyrene or other particles of various sizes or solutions of DNA (see experimental section for details) on SU8 substrates, leave behind round coffee stains if left alone to evaporate without EW. A few typical examples are shown in first column of Fig. 2. Due to the moderate hydrophobicity of SU8, the drop belongs to the class of intermediate systems, in which the contact line is initially pinning (up to τ = 0.2 in Fig. 3), then depins and later on, and from $\tau = 0.8$ on remains pinned again. The coffee stain is formed in the late stage for $0.8 < \tau < 1$. (τ is the time normalized by the total evaporation time t_{evap} , which is approximately 10 min.) The typical velocities of the evaporation-driven flow are of order 10-20 $\mu m/s$ during most of the evaporation process (see Fig. 4). According to the above discussion, coffee stains are formed due to the combination of contact line pinning and the resulting flux of solvent and solute towards the contact line. Previous strategies to overcome the coffee stain effect focused either on the elimination of contact line pinning by using low hystersis materials [7, 4] and by mechanical shaking or on the generation of internal flow patterns to counteract the evaporation driven flux with surface tension gradients driven 'Marangoni flows' [16] and with electroosmotic flows [17]. Electrowetting can be particularly efficient at counteracting coffee stain formation because it offers the unique possibility of addressing both aspects simultaneously. It can set pinned contact lines in motion and eliminate contact angle hystersis [18] and it can generate internal flow fields within sessile drops.

Electrowetting [19] is known to be a particularly versatile tool to manipulate drops of conductive liquids such as water as well as variety of other highly polarizable solvents. EW provides a unique way to exert forces directly to the contact line of sessile drops. For the

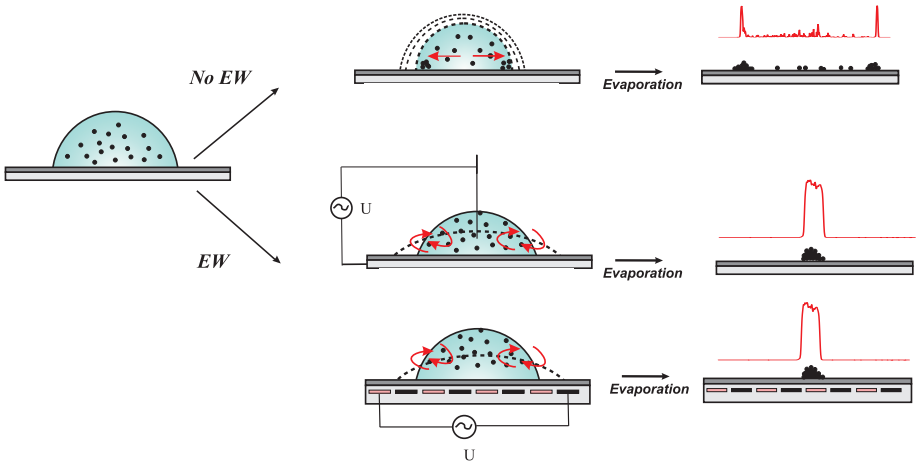

Figure 6.1: Schematic of the drop evaporation process. Top row represents evaporation without electrowetting and with contact line pinning; Middle & bottom panels show the process with electrowetting and mobile contact lines. The middle panel illustrates the conventional EW setup whereas the bottom panel illustrates the alternative wire-free geometry of EW using interdigitated electrodes. Right column: schematic and experimental intensity cross-sections (solid lines) through the residue. Experimental data taken from Fig. 2a and 2c.

generic electrowetting geometry of a drop deposited on a dielectric layer of thickness d and dielectric constant ϵ_d covering an electrode, applying a voltage U between the drop and the electrode gives rise to an electric force per unit length pulling outward on the contact line that can be written as $f_{el} = \frac{\epsilon_d \epsilon_0 U^2}{2d}$(ϵ_0: vacuum permittivity). (In fact, this force is distributed over a range of order d around the contact line. Yet, for a typical drop radius $R >> d$, this effect can be neglected if we consider only the global response of the drop [20]. Inserting f_{el} into the force balance at the three-phase contact line gives rise to the well-known electrowetting equation, which describes the reduction of the contact angle (θ) as a function of the applied voltage

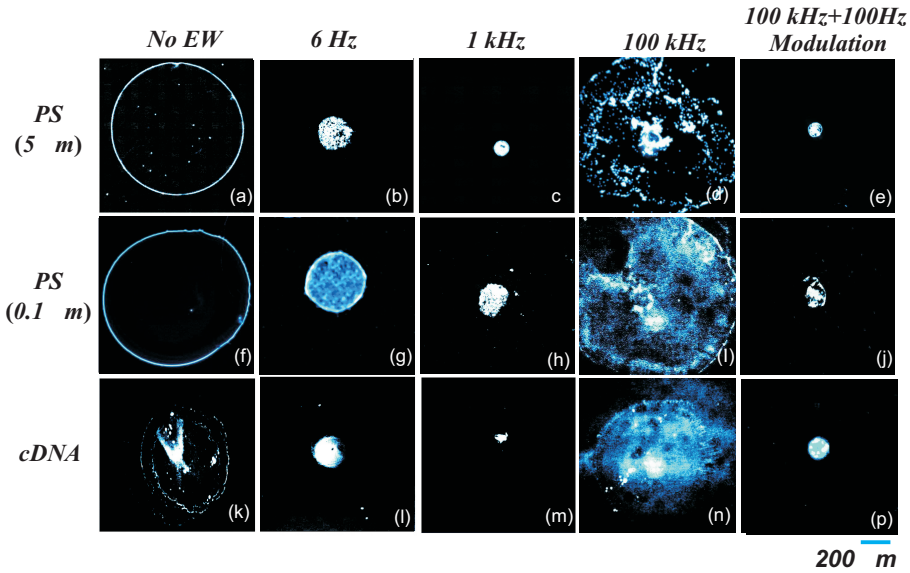

Figure 6.2: Suppression of coffee stain effect illustrated for different materials at three characteristic frequency regimes (6 Hz, 1 kHz, 100 kHz and 100 kHz with 100 Hz amplitude modulation). Panels a-p show the residual patterns for various materials under different frequency regimes. Panels a-e, Panels f-j and Panels k-p demonstrate the suppression of coffee stain for 5 μm and 0.1 μm diameter colloidal particles and fluorescently labeled cDNA respectively.

$$\cos\theta = \cos\theta_Y + \eta \tag{6.1}$$

Here, $\eta = \frac{f_{el}}{\sigma}$ is the dimensionless electrowetting number, σ is the surface tension of the drop and θ_Y is Young's angle. In the presence of contact angle hysteresis, eq. 8.1 has to be complemented by a pinning force of random magnitude $\pm f_p$ that counteracts any contact line motion. The strength of the pinning force is related to the macroscopic contact angle hysteresis by , $f_p = \sigma(cos\theta_a - cos\theta_r)$where θ_a and θ_r are the advancing and the receding contact angle. For the present samples, we have $f_p \approx 0.35\sigma$. Pinned contact lines can be set in motion by applying an electric force that exceeds the maximum

pinning force, i.e. by applying a sufficiently high voltage. In EW devices pinning forces typically lead to a finite threshold voltage to initiate drop motion (see Mugele et al. [19] and references there). As we ramp up and down the applied voltage at frequencies far below the lowest eigen frequency, the contact angle and drop radius follow the driving force quasistatically. Using a maximum voltage of U = 200 V ($\eta = 0.8 > 0.35$), the contact line keeps moving and the contact radius keeps decreasing up to times $\tau > 0.95$ (see triangles in Fig. 3). Yet, the concentration of solute along the contact line keeps increasing. As a result, the precipitation eventually occurs and the contact line remains pinned at $\frac{R}{R_0}$ = 0.3 . The residue is thus much better concentrated in a single spot and the second column of Fig. 2 shows that fluorescence intensity is much more homogeneously distributed than without EW. To improve the situation further, it is necessary to prevent the accumulation of the solute at the contact line. This can only be achieved by overcoming the evaporation-driven flow field within the drops. EW can generate flow fields in two different ways. For driving frequencies in the range of several tens of Hz to a few kHz [21, 22, 23], the excitation of eigenmodes [24]; and/or propagating capillary waves [21] at the drop surface can drive internal flows with maximum flow velocities of several hundred $\mu m/s$. These flows are driven by a purely hydrodynamic mechanism, in which the drop is forced by the time-dependent electric force f_{el} acting on the contact line. Similar flow patterns can also be generated at AC frequencies of order 100 kHz and above for poorly conductive liquids. The physical mechanism driving these high frequency flows is completely different: at these high frequencies and low conductivities, electric fields penetrate into the liquid leading to Ohmic current and local heating of several degrees within the drop. The resulting temperature gradients and along with the electric fields give rise to electrothermal flows [25, 26]. Column 3 in Fig. 2 shows that the hydrodynamic flows are even more efficient in suppressing the coffee stain effect than the quasistatic driving. This is caused by very strong flow fields within the drop. As shown in Fig. 4, the characteristic velocities exceed the ones of the evaporation-driven flow by approximately an order of magnitude throughout almost the entire evaporation process. This strong flow completely prevents any accumulation/jamming of solute

due to confinement [27] along the contact line. The shear forces generated by the flow are even strong enough to erode/unjam preformed precipitates at the contact line, as can be seen if EW is activated only at $\tau = 0.5$.

In contrast, electrothermal excitation (column 4, Fig. 2) does lead to a more homogeneous distribution of the solute than the pure case but does not succeed in reducing the spot size. We attribute the poor performance of the high frequency excitation to a combination of two effects. First of all, Fig. 4 shows that the initially high flow speed rapidly decays as the evaporation proceeds. This decrease is probably due to the inevitable increase of the conductivity of the liquid as the salt concentration increases upon solvent evaporation. It results in better screening of the electric field and hence the electrothermal driving force decreases. Second, at the very high driving frequencies inertia prevents any net motion of the drop. Hence the contact line can be pinned more easily. The latter problem can be eliminated by modulating the amplitude of the high frequency excitation with a low frequency. The fifth column of Fig. 2 shows that a 100 Hz amplitude modulation of a 100 kHz carrier excitation indeed produces very small and concentrated drop residues. Since the high frequency excitation also speeds up the evaporation process (by approximately a factor 2 in the present experiments) this combination may be desirable in applications that are not harmed by temperature increases up to 10 or 20 $^{\circ}C$

6.2 Materials and Methods

Electrowetting setup: The experiments are performed on glass substrates with a transparent Indium Tin Oxide (ITO) layer as electrode. The electrodes are covered with a 5 μm thick layer of SU8, which displays an advancing and receding contact angle of θ_a = and θ_r =, respectively. In the standard electrowetting configuration the electrode on the substrate is electrically grounded and the voltage is applied to the drop by immersing a 50 μm diameter Pt wire all the way to the bottom of the drop. In the wire-free configuration, the ITO is patterned lithographically into sets of interdigitated electrodes

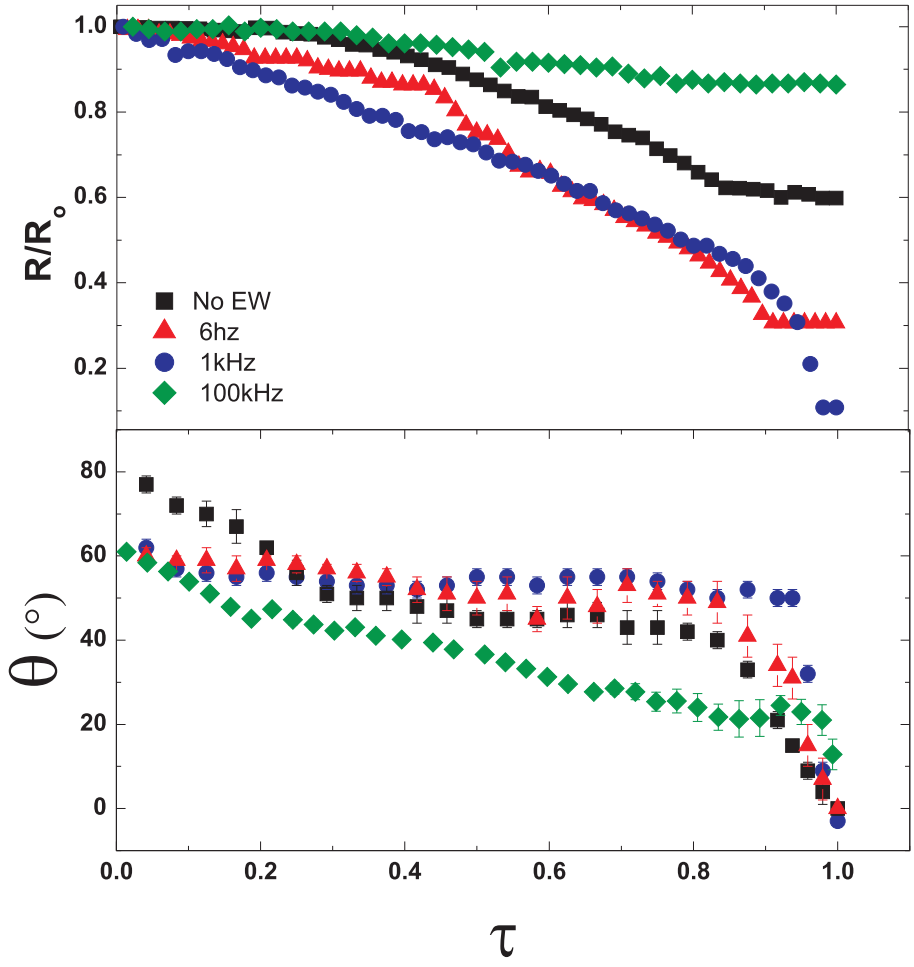

Figure 6.3: Normalized radius ($\frac{R}{R_0}$) of evaporating drop (top panel) and contact angle (θ) in bottom panel as a function of normalized time (τ) for different frequency regimes described in main text. Time is normalized with respect to the time required for complete evaporation (t_{evap}) and radius is normalized with respect to the initial drop radius (R_0). The solute used in this experiment is 5 μm diameter carboxylate terminated Polystrene particles dispersed in Millipore water with 10 mM LiCl.

with a pitch of 30 μm. An applied voltage with a fixed root-mean-square amplitude U_{rms} = 200 V is applied throughout at frequencies varying from 6Hz to 100 kHz. The experiments are carried out at an ambient temperature of 23±2 $^\circ$ C under transparent plastic box (diameter approx. 5 cm) to block air currents. The evaporating drop is monitored from two different directions: bottom and side view. The contact angle measurements were from the side view and the radius, velocity measurements were from the bottom view. The fast movements of the 5 μm particles inside the droplet were recorded using a high speed camera (Photron fastcam SA3). By using particle tracking techniques [28], the trajectories of the particles were analyzed to obtain the average flow speeds in side the drop given in Figure 4.

Materials: Aqueous solutions were prepared using deionized (MilliPore) water. 10 mM of LiCl was added to adjust the conductivity of the solution to 2 mS/cm. Colloidal suspensions of fluorescently labeled carboxyl terminated polystyrene particles (Polysciences Inc.) ranging from 0.1 μm to 5 μm in diameter are prepared with a volume fraction of 0.05%. DNA solutions with a concentration of 2.5 $ng/\mu L$ are prepared by diluting a fluorescently labeled (SYTO 24) stock solution of cDNA with deionized water in a 4:1 ratio

6.3 Results and discussion

All results do not depend very sensitively on the exact value of the AC frequency. The behavior reported refers to three different frequency regimes: (i) the quasistatic regime at frequencies below the lowest eigenfrequency of the drop, i.e. typically up to about 10 Hz for a millimeter-seized drops; (ii) the hydrodynamic regime in the range of the eigenfrequencies of the drop from several tens of Hz to a few kHz; (iii) the electrothermal regime at frequencies allowing for penetration of the electric field into the bulk of the liquid. Achieving the smallest residue spots requires a combination of moving contact lines to prevent pinning and of internal flow fields to avoid solute accumulation along the contact line. This is best achieved in the hydrodynamic regime or by a combination of high frequencies with low frequency amplitude modulation. In applications such as mi-

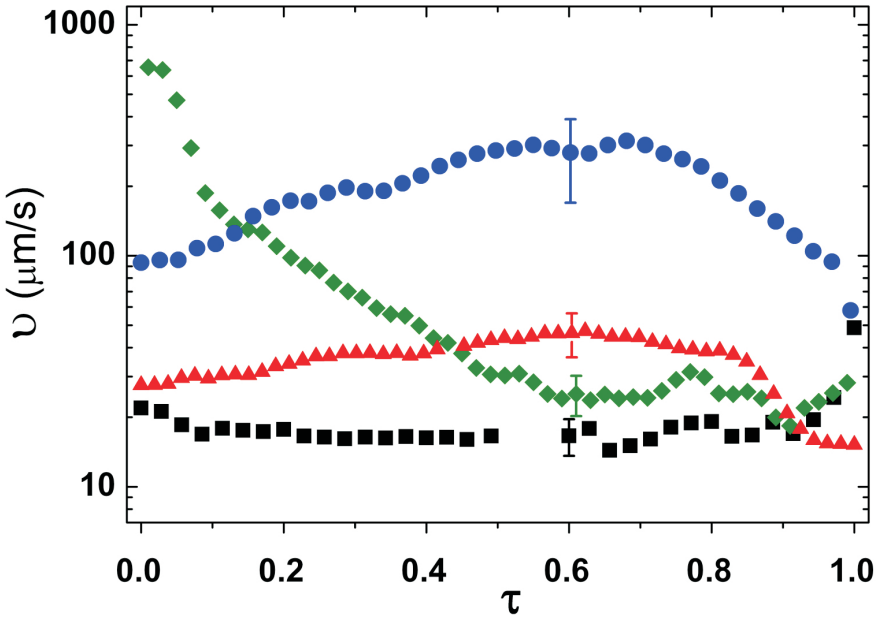

Figure 6.4: Average Particle velocity (v) as a function of normalized time for different frequency regimes and the reference experiment where no EW is applied. The time is normalized with respect to time required for complete evaporation. The solute used in experiment is 5 μm diameter polystrene particle in Millipore water with 10 mM LiCl.

croarrays the presence of the wire which is immersed into the drop in the standard configuration of EW is frequently inconvenient. Yet, this wire can be eliminated by using interdigitated electrodes embedded into the substrate instead (see Fig. 5). Test experiments demonstrate that the coffee stain effect can be perfectly suppressed for arrays of drops evaporating in such a wire-free configuration for driving frequencies in the hydrodynamic regime. Compared to other approaches of suppressing the coffee stain effect [4, 16, 29], EW has the disadvantage that is requires conductive (or highly polarizable) liquids. Yet, the experiments reported here demonstrate that the mechanism works very efficiently even for deionized water, which is

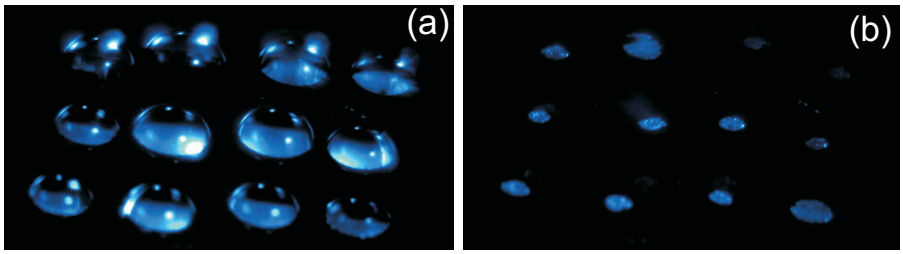

Figure 6.5: Illustration of the interdigitated electrode setup where many drops can be treated in parallel. Panel a and b show the side view and top view of the setup respectively. Panel c and d demonstrate the many drops treated with the method .

the most important solvent certainly for biological applications. EW has the practical advantage that it is noninvasive i.e. it neither requires specific additives to the system such as surfactants nor does it require or generate heating if operated in the most successful hydrodynamic frequency range. Furthermore, the liquid is not in direct contact with electrodes which is a desirable feature while working with biological systems. The extension to other substrate materials is currently being explored. Earlier successes regarding the reduction of contact angle hysteresis for a variety of polymer materials are promising [18, 30].

The possibility of applying arbitrary waveforms for the excitation of the drops such as the high frequency with amplitude modulation demonstrates the flexibility of EW. This suggests that even more flexible control of the solute assembly in evaporating drops can be achieved in the future, e.g. by combining specific waveforms with custom-shaped electrode geometries.

6.4 Conclusions

Our results demonstrate that electrowetting is a very efficient tool for suppressing the coffee stain effect in evaporating drops of complex fluids. AC frequencies in the kHz range that promote strong internal

flows while preserving the perfect conductor character of the liquid turn out to be most efficient. Interdigitated electrodes allow for an easy wire-free implementation of the approach as required for the purpose of many high throughput combinatorial analysis systems .

6.5 Contributions & Acknowledgments

H.B.Eral, D.A.Mampallil performed the experiments, analyzed the experimental data and contributed equally to this work. HBE would like thank to A.G.Marin for fruitful discussions. D. Wijnperle for assistance with interdigitated electrodes.We thank Tom Witten and Laurent Limat for discussions. We acknowledge funding by the Dutch Science Foundation NOW/chemical sciences within the ECHO program and by MicroNed, the Dutch network for microtechnology.

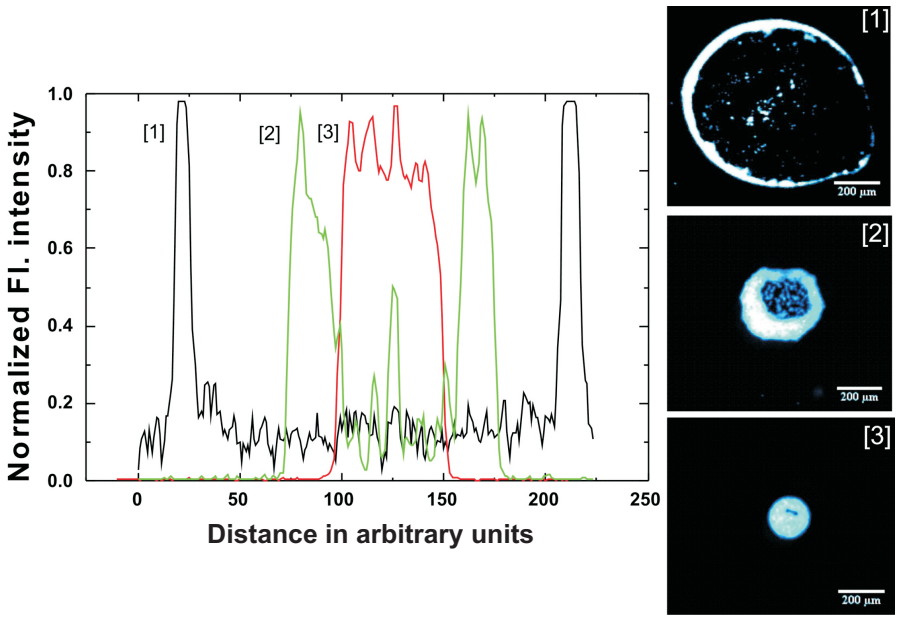

Figure 6.6: Illustration EW control over the size of Coffee stain.

6.6 Appendix

EW does not only provide a mean to suppress coffee stain effect but also provides control over the extent and size of Coffee stains. Figure S1 provides the intensity profiles and pictures of three residues: [1] Control experiment where the drop is allowed to evaporate on the same substrate, [2]: Partially suppressed coffee stain where the applied voltage is turned off prior to complete evaporation and [3] Complete suppression of coffee stain where the drop is treated with EW throughout the course of the evaporation. The drops are prepared with 5 μm Polystrene particles dispersed in 10 mM LiCl dissolved in deionized water.

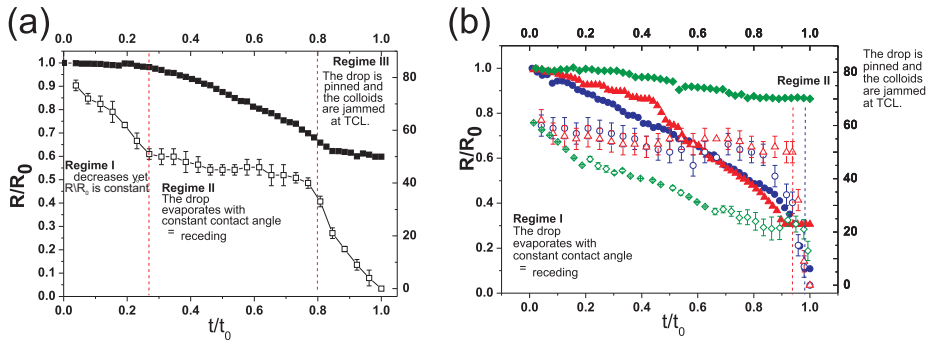

Figure 6.7: Normalized drop radius (Panel (a)) and Contact angle (Panel (b)) of the evaporating drop as a function of the normalized time for different frequency regimes and the reference experiment where no EW is applied. The time is normalized with respect to time required for the complete evaporation. The solute used in experiment is 5 μm diameter carboxylate terminated Polystrene particles in Millipore water with 10 mM LiCl.

An alternative to Fig. 3 where the contact angle and the normalized drop radius are plotted in a single figure for ease of comparison. Fig. 6.7 allows the reader to directly compare the evolution of the contact angle and the drop radius.

Bibliography

[1] R. D. Deegan, O. Bakajin, T. F. Dupont, G. Huber, S. R. Nagel, and T. A. Witten. Capillary flow as the cause for ring stains from dried liquid drops. *Nature*, 389(6653):827, 1997.

[2] G. McHale. Surface free energy and microarray deposition technology. *Analyst*, 132(3):192–195, DEC 2007.

[3] M. Dufva. Fabrication of high quality microarrays. *Biomolecular Engineering*, 22(5-6):173–184, DEC 2005.

[4] R. Blossey and A. Bosio. Contact line deposits on cdna microarrays: A "twin-spot effect". *Langmuir*, 18(7):2952–2954, APR 2 2002.

[5] Y. Kim, G. B. Hurst, M. J. Doktycz, and M. V. Buchanan. Improving spot homogeneity by using polymer substrates in matrix-assisted laser desorption/ionization mass spectrometry of oligonucleotides. *Analytical Chemistry*, 73(11):2617–2624, 2001.

[6] B. Guo. Mass spectrometry in dna analysis. *Analytical Chemistry*, 71(12):333–337, 2001.

[7] K. C. Hung, H. Ding, and B. Guo. Use of poly(tetrafluoroethylene)s as a sample support for the maldi-tof analysis of dna and proteins. *Analytical Chemistry*, 71(2):518–521, 1999.

[8] S. Choi, S. Stassi, A. P. Pisano, and T. I. Zohdi. Coffee-ring effect-based three dimensional patterning of micro/nanoparticle assembly with a single droplet. *Langmuir*, 26(14):11690–11698, JUL 20 2010.

[9] M. Grzelczak, J. Vermant, E. M. Furst, and L. M. Liz-Marzan. Directed self-assembly of nanoparticles. *ACS Nano*, 4(7):3591–3605, 2010.

[10] B. G. Prevo and O. D. Velev. Controlled, rapid deposition of structured coatings from micro- and nanoparticle suspensions. *Langmuir*, 20(6):2099–2107, MAR 16 2004.

[11] H. Bodiguel, F. Doumenc, and B. Guerrier. Stick-slip patterning at low capillary numbers for an evaporating colloidal suspension. *Langmuir*, 26(13):10758–10763, JUL 6 2010.

[12] D. J. Harris, H. Hu, J. C. Conrad, and J. A. Lewis. Patterning colloidal films via evaporative lithography. *Phys. Rev.Lett.*, 98(14), APR 6 2007.

[13] M. Layani, M. Gruchko, O. Milo, D. Balberg, I.and Azulay, and S. Magdassi. Transparent conductive coatings by printing coffee ring arrays obtained at room temperature. *ACS Nano*, 3(11):3537–3542, 2009.

[14] I. I. Smalyukh, O.V. Zribi, J. C. Butler, O. D. Lavrentovich, and G. C. L. Wong. Structure and dynamics of liquid crystalline pattern formation in drying droplets of dna. *Phys. Rev. Lett.*, 96(17):177801, 2006.

[15] L. Shmuylovich, A. Q. Shen, and H. A. Stone. Surface morphology of drying latex films: Multiple ring formation. *Langmuir*, 18(9):3441–3445, 2002.

[16] H. Hu and R. G. Larson. Marangoni effect reverses coffee-ring depositions. *J.Phys. Chem. B*, 110(14):7090–7094, APR 13 2006.

[17] S. J. Kim, K. H. Kang, J. Lee, and B. J. Kang, I. S.and Yoon. Control of particle-deposition pattern in a sessile droplet by using radial electroosmotic flow. *Analytical Chemistry*, 78(14):5192–5197, 2006.

[18] F. Li and F. Mugele. How to make sticky surfaces slippery: Contact angle hysteresis in electrowetting with alternating voltage. *Applied Physics Letters*, 92(24):244108, 2008.

[19] F. Mugele and J.C. Baret. Electrowetting: from basics to applications. *J. Phys.: Condens. Matter*, 17(28):705–744, 2005.

[20] J. Buehrle, S. Herminghaus, and F. Mugele. Interface profiles near three-phase contact lines in electric fields. *Phys. Rev. Lett.*, 91(8):086101, Aug 2003.

[21] F. Mugele, J. C. Baret, and D. Steinhauser. Microfluidic mixing through electrowetting-induced droplet oscillations. *Applied Physics Letters*, 88(20):204106–204106, 2006.

[22] S. H. Ko, H. Lee, and K. H. Kang. Hydrodynamic flows in electrowetting. *Langmuir*, 24(3):1094–1101, 2008.

[23] K. P. Nichols and J. G. E. Gardeniers. A digital microfluidic system for the investigation of pre-steady-state enzyme kinetics using rapid quenching with maldi-tof mass spectrometry. *Analytical Chemistry*, 79(22):8699–8704, 2007.

[24] J. M. Oh, S. H. Ko, and K. H. Kang. Shape oscillation of a drop in ac electrowetting. *Langmuir*, 24(15):8379–8386, 2008.

[25] H. Lee, S. Yun, S. H. Ko, and K. H. Kang. An electrohydrodynamic flow in ac electrowetting. *Biomicrofluidics*, 3(4):044113, 2009.

[26] P. García-Sánchez, A. Ramos, and F. Mugele. Electrothermally driven flows in ac electrowetting. *Phys. Rev. E*, 81(1):015303, Jan 2010.

[27] H. B. Eral, D. van den Ende, F. Mugele, and M. H. G. Duits. Influence of confinement by smooth and rough walls on particle dynamics in dense hard-sphere suspensions. *Phys. Rev. E*, 80(6):061403, 2009.

[28] F. Sbalzarini and P. Koumoutsakos. Feature point tracking and trajectory analysis for video imaging in cell biology. *Journal of Structural Biology*, 151(2):182–195, 2005.

[29] W. D. Ristenpart, P. G. Kim, C. Domingues, J. Wan, and H. A. Stone. Influence of substrate conductivity on circulation reversal in evaporating drops. *Phys. Rev.Lett.*, 99(23), DEC 7 2007.

[30] D. J. C. M. 't Mannetje, C. U. Murade, D. van den Ende, and F. Mugele. Electrically assisted drop sliding on inclined planes. *Applied Physics Letters*, 98(1):014102, 2011.

7 Drops on functional fibers: from barrels to clamshells and back

Abstract Drops on fibers are a familiar sight, for instance in the form of dew drops on spider webs. They can exist in two competing morphologies, a cylindrically symmetric barrel state completely engulfing the fiber and an asymmetric clamshell state, in which the drop touches the fiber only sideways. Despite their omnipresence and their practical relevance, the physical mechanisms governing the stability of the two morphologies remained elusive. Using electrowetting-functionalized fibers we can tune the wettability of fibers and thereby reversibly switch between the two states. This allows to determine the stability limits of both morphologies as a function of the two relevant control parameters, namely the contact angle and the volume. While clamshells are found to prevail for large contact angles and small volumes and barrels prevail for small angles and large volumes, there is also a wide range of intermediate parameter values, for which both morphologies are mechanically stable. From a general perspective, the demonstration of electrowetting-based reversible switching of liquid morphologies on fibers opens up opportunities for designing functional textiles and porous materials for various applications in filtering, and controlled absorption and release of liquids.

7.1 Introduction

Already Plateau noted that liquid films covering a cylindrical fiber are unstable and spontaneously break into cylindrically symmetric pearl like structures, referred to as undoloids or barrel shapes [1]. The driving mechanism behind this instability is the same gain in surface energy that also controls the break-up of liquid jets into drops that was first explained by Rayleigh [2]. Mathematically, barrels belong to the cylindrically symmetric solutions of the Young-Laplace equation known as Delaunay surfaces [3]. Yet, the cylindrically symmetric barrel state resulting from the Rayleigh-Plateau break-up is not the only possible morphology of drops on cylindrical fibers. Rather, it competes with the symmetry-broken "clamshell" morphology, as noted by Adams [4]. Studying detergency, he observed that clamshells become preferred as compared to barrels when the contact angle of oil drops on fibers increases upon adding surfactant to a surrounding aqueous medium. Competing morphologies of drops attracted considerable attention in recent years in the context of microfluidics, in particular drop-based "digital" microfluidics. It was shown that drops can be forced into certain desired morphologies by exposing them to surfaces with custom-designed topographic and wettability patterns, such as superhydrophobic surfaces [5, 6, 7, 8, 9, 10, 11]. Yet, the control is incomplete, since the surface patterns merely provide boundary conditions. The liquid remains free to assume any morphology that is compatible with the imposed constraints. The non-linearity of the underlying equations frequently leads to several mechanically stable solutions, with sometimes rather counterintuitive shapes [6]. By changing the imposed boundary conditions, it is possible to change the shape of a drop both continuously within a given class of morphologies and discontinuously switching from one class of morphologies to another. Techniques to switch the surface wettability, such as electrowetting [12], substantially enhance the flexibility and control for drop manipulation. Notwithstanding all these efforts, our understanding of drops on cylindrical fibers, the oldest and arguably most fundamental example of competing liquid morphologies, has remained remarkably incomplete. Carroll performed experiments with slowly dissolving drops [13]. He analyzed the spontaneous transfor-

mation of barrels into clamshells and proposed an instability mechanism based on a specific variation of the drop shape. McHale et al. [14, 15, 16] performed a series of numerical studies and proposed another mechanism, the so-called inflection point criterion. Yet, neither mechanism agrees very well with the experimental data [15, 17]. Other recent work focused on the relevance of molecular scale interaction in the wetting of nano-fibers [18, 19] and on dynamic aspects of drops on fibers [7, 20, 21] but left the basic problem of the stability limits of the competing drop morphologies unsolved. In this work, we approach this long standing question combining a novel experimental approach and finite element calculations. Fibers with electrowetting functionality are developed to reversibly vary the contact angle of the drop. Our experiments allow to follow the hitherto unobserved reverse clamshell-to-barrel transition and determine the stability limits of both morphologies. Numerical calculations minimizing the total surface energy E confirm the resulting morphology diagram and provide a detailed picture of the energy landscape explaining both similarities and differences between the barrel-to-clamshell and the reverse transition.

7.2 Results

A buoyancy-neutral highly wetting oil drop is placed on an insulator-covered cylindrical metal fiber in ambient water (see Fig. 1A). Owing to the metal core and the insulating coating, the contact angle θ of the oil on the fiber can be increased by applying a voltage between the fiber and the ambient aqueous phase by means of electrowetting [12]. At zero voltage, is small and the oil drop adopts the cylindrically symmetric barrel morphology (upper right panel of Fig. 1B) Upon increasing the contact angle, the drop initially deforms reversibly while retaining cylindrical symmetry. At some volume-dependent critical contact angle θ_{c1}, an abrupt transition to the asymmetric clamshell state takes place (lower left panel of Fig. 1B). The buoyancy-neutral clamshell drop can in principle adhere to any side of the fiber. Yet, for any given drop-fiber combination, minor imperfections on the fiber surface usually lead to some preferred orientation. In the clamshell

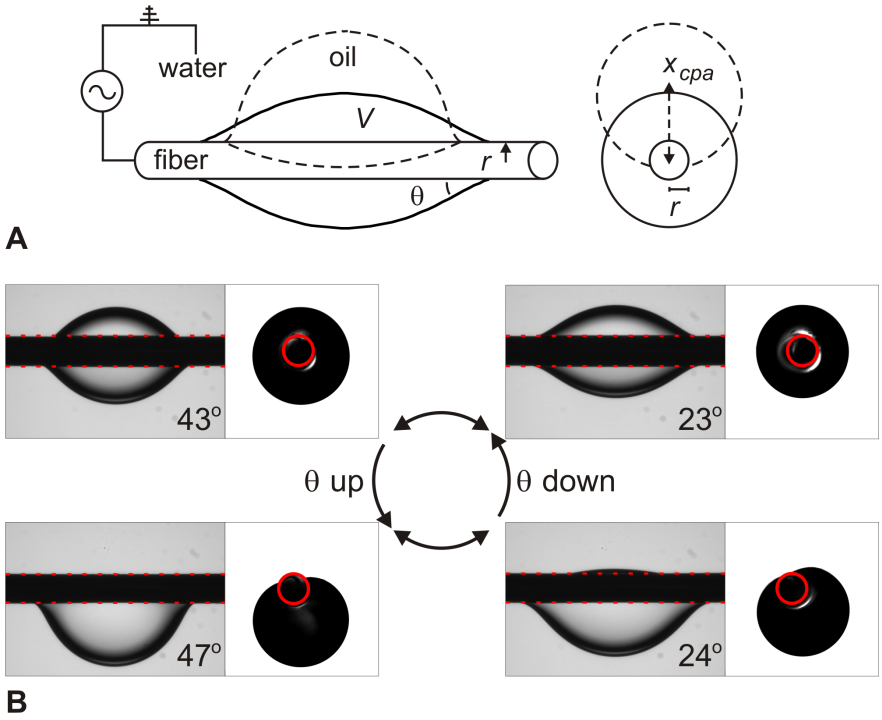

Figure 7.1: (A) Schematic of the buoyancy-neutral electrowetting set-up, showing the side (left) and head-on views (right) of the barrel (solid) and clam-shell (dashed) morphologies. The characteristic parameters are the drop volume V , the fiber radius r_f , the contact angle θ , and the center of mass position x_{CM} . (B) Side view and head-on view of the morphological transitions upon electrowetting-induced contact angle variations. The figure shows the drop just before and just after the barrel-to-clamshell and clamshell-to-barrel transitions. The fiber diameter, as indicated by the red circle, is 0.3 mm.

state the drop shape can again be tuned continuously. Note that the simply connected clamshell morphology is topologically distinct from the multiply connected barrel morphology. Consequently, clamshell drops have a single continuous three-phase contact line with a complex shape that depends on the contact angle, whereas barrel drops have two separated contact lines with a simple circular shape. These aspects distinguish the barrel-to-clamshell transition from other morphology transitions, such as for drops on stripes of variable wettability [6, 22, 23] . Upon decreasing the contact angle in the clamshell state, another abrupt transition back to the barrel state takes place at a second critical contact angle $\theta_{c2} < \theta_{c1}$. It is worth noting that θ_{c1} has a finite value. This is fundamentally different from both a two-dimensional drop wetting a circular disk and from a three-dimensional drop wetting a sphere. In both cases, engulfment of the solid by the liquid only takes place for $\theta \to 0$. In the present case of a drop wetting on a cylindrical fiber, however, two opposing sections of the three phase contact line in the clamshell state approach each other and eventually merge at a finite contact angle $\theta_{c2} > 0$. This process can be observed in detail in the head-on views in the bottom row of Fig. 1B.

To characterize the morphology transition more quantitatively, it is useful to plot the radial position of the center of mass of the liquid as a function of the contact angle. For barrel drops, it should be located on the fiber axis, whereas for clamshell drops it lies off-axis. Since the center of mass is difficult to extract from the experimental data, we plot in Fig. 2 the (normalized) radial position of the center of the projected area $\tilde{x}_{cpa} = x_{cpa}/r$ of the drop, which is readily obtained from the head on views of the drop. As expected, the barrel-to-clamshell transition is characterized by a steep change in $\tilde{x}_{cpa}$ from zero in the barrel state to a volume-dependent finite value at θ_{c1}. Interestingly, the transition is frequently preceded by weak non-axisymmetric perturbations for values of θ just below θ_{c1}, which remain stable on for hours. Thanks to their topology, we can nevertheless identify these states as clearly "barrel-like". Upon increasing θ further within the clamshell morphology, $\tilde{x}_{cpa}$ increases continuously as the drop gradually moves outward and vice versa. As we decrease θ, $\tilde{x}_{cpa}$ jumps back to zero as the clamshell-to-barrel transition takes

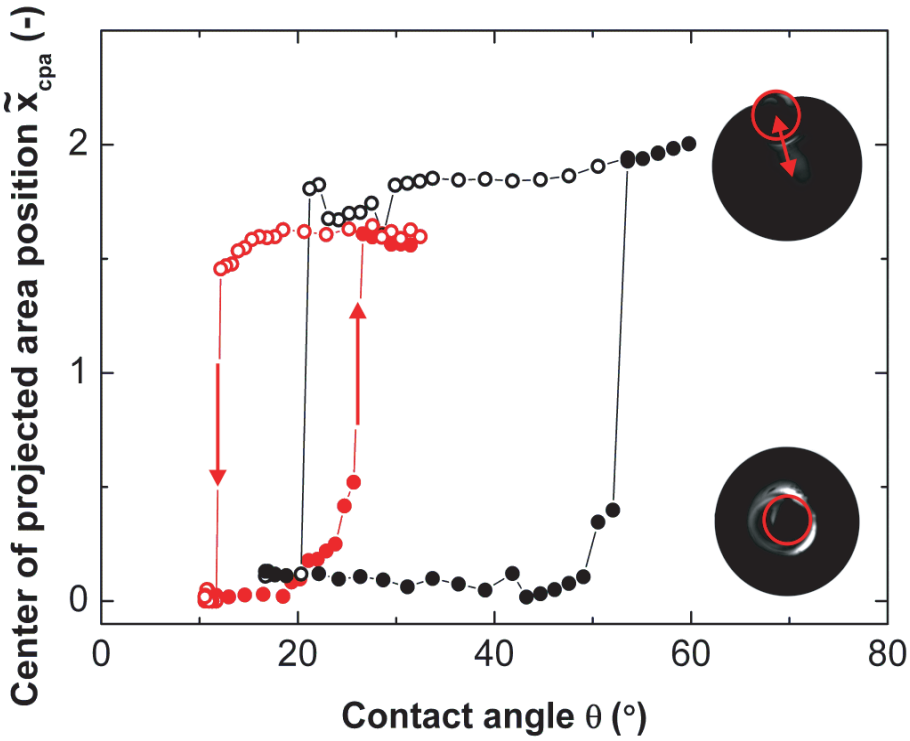

Figure 7.2: Center of projected area position $\tilde{x}_{cpa}$ versus contact angle θ for two drops with reduced volume i.e volume of the drop (V) normalized by radius of the fiber (r)i.e.($\tilde{V} = V/r^3$) $\tilde{V} = 29$ (red) and $\tilde{V} = 165$ (black); the fiber diameter is 0.3 mm. The filled and open symbols indicate increasing and decreasing contact angles, respectively. The lower and upper insets show the drop in the barrel and clam-shell regime, respectively, and the corresponding shift in the position of the center of projected area with respect to the fiber (in red).

place at θ_{c2}. Both critical contact angles θ_{c1} and θ_{c1} as well as the hysteresis interval $\Delta\theta = \theta_{c1}$ - θ_{c2} are found to increase upon repeating the experiments for larger drop volumes V while keeping the fiber radius r constant. Similarly, experiments with smaller r at the same drop volume lead to increases in θ_{c1} , θ_{c2}, and $\Delta\theta$. Plotting θ_{c1} and θ_{c2} as a function of the reduced volume $\tilde{V} = V/r^3$ yields universal stability limits for both morphologies (as long as gravity is negligible) and thus a universal morphology diagram with control parameters θ and $\tilde{V}$ (see Fig. 3). For large θ and small $\tilde{V}$ only the clamshell is mechanically stable, whereas for small θ and large $\tilde{V}$ only barrels are stable. For a wide range of intermediate parameter values both morphologies can exist.

To gain more insight into the stability limits of the drops we consider the free energy of the system, which can be expressed in units of the surface tension γ of the drop (i.e. the oil-water interfacial tension) as

$$\frac{E}{\gamma} = A_{ow} - A_{of} cos\theta(U) \tag{7.1}$$

where A_{ow} and A_{of} are the oil-water and oil-fiber interfacial areas, respectively. The function $\theta(U)$ is the voltage-dependent contact angle following the electrowetting equations (see Materials and Methods).

We consider first the cylindrically symmetric barrels. Owing to the high symmetry of the barrel morphology, their shapes and interfacial energy can be calculated analytically. The profile of the liquid interface, which can be expressed in terms of elliptical integrals [3, 13], fulfills the criterion of a constant mean curvature H, as expressed in the Young-Laplace equation $\Delta p = 2H\gamma$ and, additionally, the condition of Young-Dupré at the contact line. Here, Δp is the pressure difference between drop interior and the ambient liquid. Fulfilling the Young-Laplace equation and condition of Young-Dupré is only a necessary, but not a sufficient criterion for mechanical stability. Mechanical stability is only guaranteed if the second variation of the energy is positive for arbitrary small deformations of the liquid interface. Restricting ourselves to volume-conserving variations around a barrel solution, it can be shown that the discussion of stability

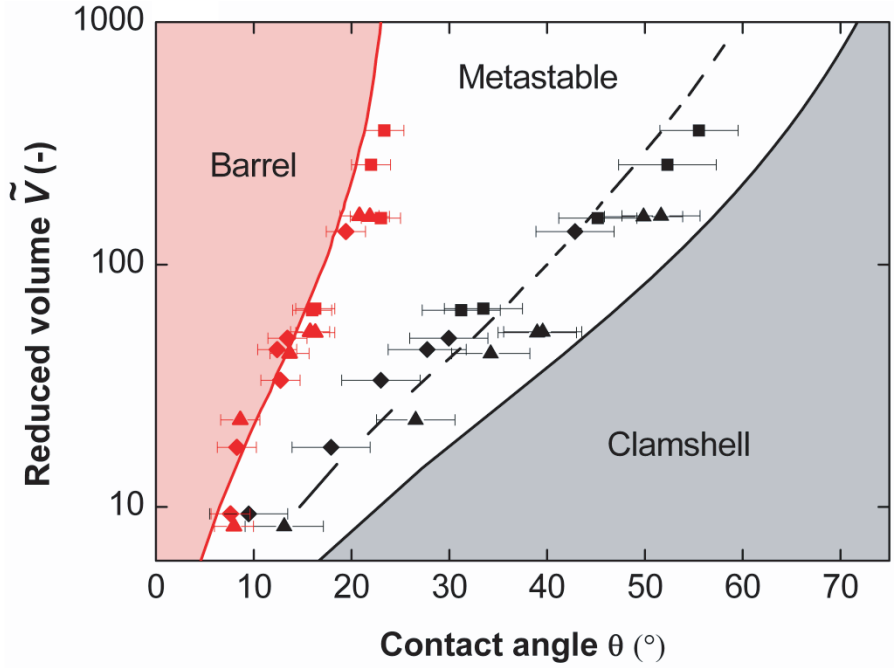

Figure 7.3: Morphology diagram of millimeter-sized drops on fibers as a function of contact angle θ and reduced volume $\tilde{V}$. Black and red symbols indicate the experimentally observed barrel-to-clamshell (θ_{c1}) and clamshell-to-barrel (θ_{c1}) transitions, respectively. Symbol shapes indicate different fiber diameters: (■) 0.2, (▲) 0.3, and (•) 0.5 mm. The solid lines indicate the numerical stability limit of the clamshell (upper red) and the (coinciding) analytical and numerical stability limit of the barrel (lower black). The dashed line indicates the condition of equal absolute energy of both states.

reduces to an eigenvalue problem $-\nabla^2\nu + (2K - 4H^2) = \lambda\nu + \mu$ for an arbitrary normal displacement field ν with boundary conditions $-n.\nabla\nu + ccot(\theta)\nu = 0$ along the contact line [24]. Here, ∇^2 denotes the Laplace-Beltrami operator and K the Gaussian curvature of the drop surface. The boundary condition involves the outward pointing co-normal n of the liquid interface on the contact line and the normal curvature c of the liquid interface into the direction of n. The parameters λ and μ are Lagrange multipliers related to normalization and volume conservation, respectively. Mechanical stability holds if the lowest relevant eigenvalue λ is positive (the zero eigenvalue corresponding to the soft model of translation along the fiber axis will be discarded in the following discussion). Parameterizing the displacement field in suitable coordinates reduces the eigenvalue problem to a one dimensional differential equation which can be solved numerically (see Supporting Information for details). It turns out that the lowest eigenvalue λ^* changes sign at a critical volume $\tilde{V}$, which increases with increasing contact angle. For $\tilde{V} < \tilde{V}_c$, we have $\lambda^* < 0$, i.e. barrel shapes are unstable, whereas for $\tilde{V} > \tilde{V}_c$ stable barrels with $\lambda^* > 0$ can be found. The relevant soft mode, which occurs at $\lambda^* = 0$ breaks the rotational symmetry of the barrel while it keeps its reflection symmetry, just as expected from the symmetries of the clamshell. The corresponding stability limit $\theta_{c1}(\tilde{V})$ based on the spectral analysis is shown as a black solid line in Fig. 3. It is interesting to note that $\theta_{c1}(\tilde{V})$ found here coincides with the inflection point criterion proposed by McHale et al. [15]: according to this heuristic criterion barrel shapes should loose their stability when the inflection point of the drop surface reaches the fiber surface upon varying $\tilde{V}$ and/or θ . For barrel shapes which satisfy the inflection point criterion we can explicitly construct the soft mode. The spectral analysis sketched here thus θ provides a rigorous proof of this conjecture. Yet, the theoretical curve for θ_{c1} lies systematically below the experimental data in Fig. 3.

For symmetry-broken shapes one has to resort to numerical calculations (see Materials and Methods for details). The equilibrium clamshell morphologies (as well as the barrel shapes) and the corresponding energies can obtained by minimizing Eq. 7.1 numerically for any given volume and wettability of the fiber . Starting from a

barrel or clamshell morphology and changing the contact angle θ in small steps for a fixed volume $\tilde{V}$ we determine the numerical boundaries of local stability $\theta_{c1}(\tilde{V})$ and $\theta_{c2}(\tilde{V})$, respectively. The numerical curve $\theta_{c1}(\tilde{V})$ agrees precisely with the theoretical one described above (black solid line in Fig. 3), thereby validating the numerical calculation. The stability limit of the clamshell state, $\theta_{c2}(\tilde{V})$ (red solid line in Fig. 3) perfectly reproduces the experimental data. (It is interesting to note that numerical curve for $\theta_{c2}(\tilde{V})$ displays a maximum of 23.5° at $\tilde{V} \approx 3000$. For even larger volumes, the critical contact angle decreases again and approaches an asymptotic value of 16° for $\tilde{V} \to \infty$. See Figure 7.6 of the Appendix I.)

In order to shed more light on the nature of the two transitions, we analyze the energy landscape connecting the two competing morphologies. To do so, we consider separately two distinct families of morphologies, namely the multiply connected barrel-like morphologies and the simply connected clamshell-like morphologies. For both families we calculate the minimum interfacial energies (including the corresponding shapes) under the constraint of an imposed radial position of the center of mass $\tilde{x_{cm}} = x_{cm}/r$ (in units of r). Plotting these energies as a function of $\tilde{x_{cm}}$ for various values of θ results in two families of curves describing the energy of barrel-like and clamshell-like morphologies, respectively (Fig. 4A). For small contact angles, barrels with an equilibrium value $\tilde{x_{eq}} = 0$ display the lowest energy. Beyond a certain (volume-dependent) contact angle, clamshells with a finite -dependent $\tilde{x_{eq}} > 0$ become energetically more favorable. Within an appreciable range of contact angles, however, two local minima in the energy landscape coexist, corresponding to the topologically distinct barrel and clamshell morphologies, respectively. An energy barrier large compared to thermal energies separates the two local minima and renders the two morphologies mechanically stable. Upon increasing the contact angle beyond a certain critical value, the energy barrier from the barrel to the clamshell morphology disappears. The corresponding critical value, at which the transition takes place spontaneously, coincides with $\tilde{\theta_{c1}}$. Similarly, the barrier for the clamshell-to-barrel transition disappears at the lower critical contact angle $\tilde{\theta_{c2}}$.

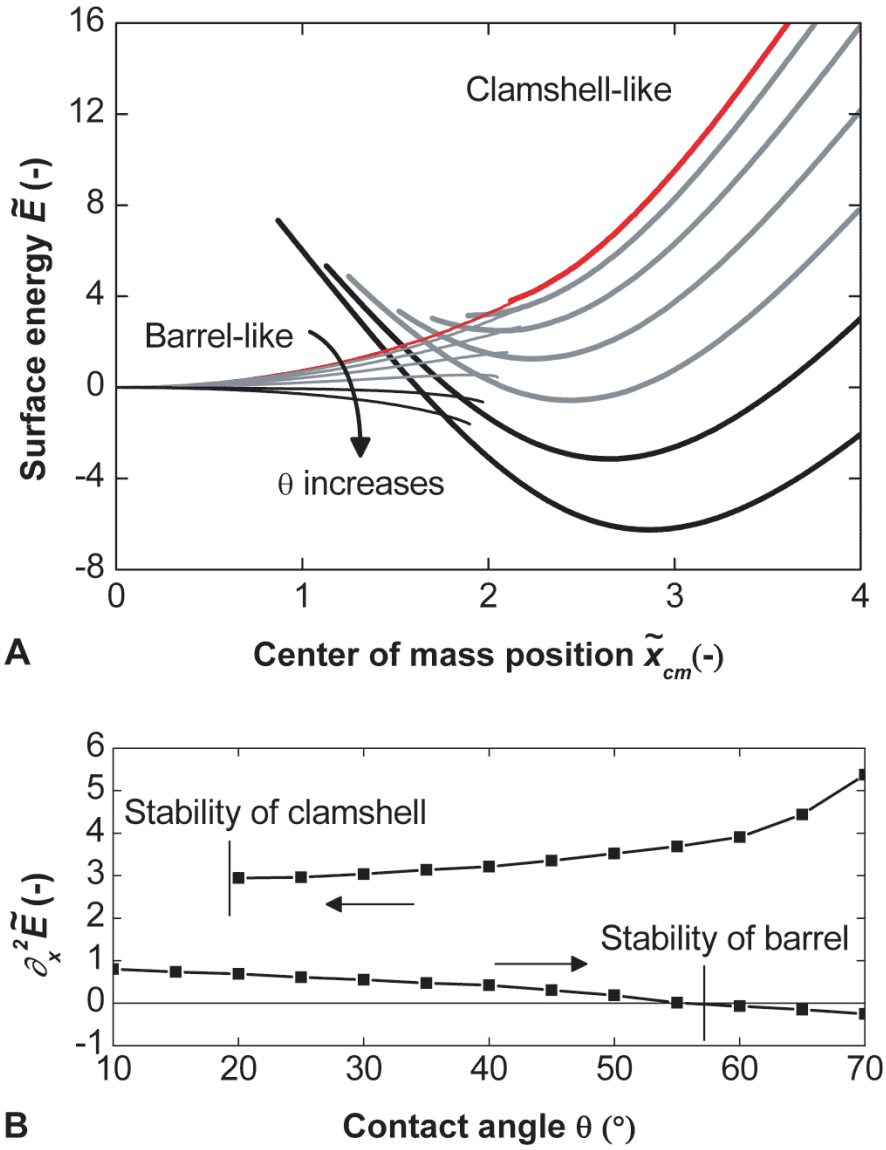

Figure 7.4: Panel (A) Normalized surface free energy of barrel-like (thin line) and clamshell-like (thick line) morphologies versus radial position of the center of mass $\tilde{x}_{cm}$ for various contact angles (10°,..., 70°) at fixed $\tilde{V}$= 200. Panel (B) Second variation of the surface free energy $\partial_x^2 \tilde{E}$ versus contact angle for the same droplet as in Panel (A), calculated in the minimum of the potential for both barrel (advancing contact angle) and clamshell (receding contact angle) energy landscapes.

7.3 Discussion

What is the origin of the systematic deviation between model results and experiments for $\tilde{\theta_{c1}}(\tilde{V})$, while $\tilde{\theta_{c2}}(\tilde{V})$ reproduces the experimental results? A closer look at Fig. 4 illustrates a profound difference between the two transitions and thereby provides a clue to understand these deviations: upon approaching the barrel-to-clamshell transition, the energy landscape around the barrel state becomes very flat and in fact the curvature of the energy curve, $\partial_x^2 \tilde{E}(0)$, changes sign at the transition (see Fig. 4B). Hence, the barrel state becomes arbitrarily soft and susceptible to perturbations similar to a thermodynamic system close to a second order phase transition. This is a direct consequence of the vanishing of the eigenvalue λ upon approaching the barrel-to-clamshell transition. In contrast, the clamshell morphology retains its stiffness right up to the clamshell-to-barrel transition, as shown by the positive curvature of the corresponding energy curve in Fig. 4B. The clamshell-to-barrel transition is thus not caused by an intrinsic instability of the clamshell morphology but by the fact that the intersection point between the energy curves of the barrel and the clamshell state shifts towards the minimum of the latter. In real space, the transition takes place when two opposing sections of the contact line approach each other and coalesce at the opposite side of the fiber with respect to the center of mass of the clamshell.

As a consequence of these differences, unavoidable non-axisymmetric imperfections of the system affect the energy barrier for the barrel-to-clamshell transition more strongly than for the reverse transition (non-axisymmetric fibers would be an extreme example of such imperfections and would more strongly favor clamshells). Thus, we can attribute both the systematic deviations for the barrel-to-clamshell transition in Fig. 3 as well as the observation of slightly distorted barrels close to θ_{c1} (Fig. 2) to the softness of the barrel state. As soon as the absolute energy of both states is the same (black dashed line in Fig. 3), the barrel-to-clamshell transition is likely to happen. The softness also implies that small external forces (e.g. due to viscous drag in oil-water separators) can easily induce a transition to the clamshell state. This facilitates the removal of drops from fibers.

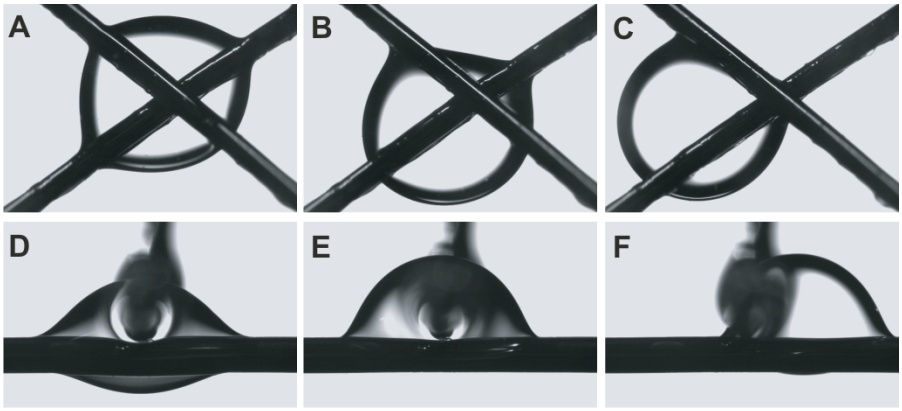

Figure 7.5: Drop between two fibers crossed at a 90° angle. In (A, B, C) a drop is shown with the plane formed by the two fibers tilted under an angle of 45° (with the lower fiber parts pointing towards the camera). In (D, E, F) a drop is shown in a head-on view of one of the fibers. With increasing contact angle, the drop is subsequently (A, D) in the barrel state with respect to both fibers, (B, E) in the barrel state with respect to one fiber while in the clamshell state with respect to the other, and (C, F) in the clamshell state with respect to both fibers.

In hindsight it is clear from the shape of the morphology diagram, why the existence of the clamshell-to-barrel transition was overlooked in the past. Experiments making use of the addition of surfactant to the aqueous phase invariably follow a path from smaller to larger contact angles. The experiments of Carroll [13] followed a path from larger to smaller volumes. In both cases, only the barrel-to-clamshell transition is observable. Clamshell-to-barrel transitions can in principle be observed upon increasing the volume, provided that the contact angle is sufficiently small. Indeed, some images from recent experiments suggest that this transition may indeed take place upon condensation of dew on spider webs [25]. Yet, the influence of gravity in those experiments as well as the complex structure of the silk fibers makes unambiguous conclusions impossible.

Our present experimental approach of EW-functionalized fibers can be easily extended to more complex three-dimensional archi-

tectures such as networks of fibers and even fabrics. Made from electrically insulated metal wires or conductive polymer fibers, such networks could be interesting for controlled retention and release of fluids in two-phase flow applications such as the separation of oil and water in emulsions. For suitable electrical signals (e.g. AC voltage) filtering aerosols, such as capturing water from fog, is also conceivable. The key challenge in this case is to optimize the geometry of the fiber network in such a way that competing drop morphologies provide a very different adhesion of the drops to the fiber network. The most elementary element of a fiber network (in addition to the straight fiber segment) is the fiber crossing. For small contact angles, liquid is found to accumulate at the crossing between almost touching fibers (see Fig. 5). At higher contact angles the droplet adopts the clamshell state with respect to both fibers. Thus, it is expelled from the crossing, and thereby much more exposed e.g. to shear forces of the ambient medium, thereby promoting release. Physically, the complexity arising from the large number of degrees of freedom (geometry, contact angles) as well as the possibility of self-amplifying effects due to capillary forces that deform (sufficiently soft) fiber networks, offers a great degree of parameter optimization of these processes.

7.4 Materials and Methods

Electrowetting set-up. Stainless steel fibers (with radius r = 0.10 – 0.25 mm) are coated with a Teflon layer (6% Teflon amorphous fluoropolymers solution, DuPont) of 2 to 8 μm using a standard dipcoating procedure [26]. A silicone oil drop (AS 100, Fluka) of microliter volume V (viscosity η = 6 mPa s, interfacial tension γ 40 mNm^{-1}) is placed on the fiber, adopting a low contact angle . The fiber is connected to an electrode to which an AC voltage is applied, and the circuit is closed through a grounded electrode in the surrounding aqueous solution of sodium chloride, see Fig. 1(a). The Bond number of the system indicates that capillarity dominates gravity ($Bo = \frac{g\Delta\rho R^2}{\gamma} < 10^{-3}$, with g the gravitational acceleration, $\Delta\rho$ the density difference, and R the typical length scale of the drop).

Contact angle manipulation. Continuous and reversible manipula-

tion of the contact angle is achieved via electrowetting (EW). For the voltage range (0,. . ., 80 V; AC frequency: 1 kHz) in the present experiments, the macroscopic contact angle measured through the oil drop follows the modified electrowetting equation:$cos(\theta) = cos(\theta_y) + \frac{\epsilon_0 \epsilon_d}{2d\gamma} U^2$ [12]. θ_Y is Young's angle (measured through the oil drop), ϵ_0 the electric constant of the vacuum, ϵ_d the dielectric constant of the insulator, and d its layer thickness. Since $d << r$, local EW effects near the contact line can be ignored here [27, 28]. The intrinsic contact angle hysteresis is below 2° , ensuring that the observed hysteresis in the transitions is due to the metastability of the two morphologies. The transitions of each drop are recorded in four subsequent electrowetting cycles to ensure repeatability.

Measurement of characteristic parameters. The drops are observed with two cameras, recording a side view and a head-on view of the fiber. The head-on view enables to unambiguously distinguish the two morphologies, which is not possible from the side view due to the asymmetric nature of the transition. The transition is indicated by a steep change in the position of the center of projected drop area with respect to the fiber, $\tilde{x}_{cpa}$ (see Fig. 1a, non-dimensionalized with fiber radius r). The characteristic parameters are extracted from the side (θ , $\tilde{V}$, r) and head-on ($\tilde{x}_{cpa}$) recordings, using a custom-written Matlab code that determines the system boundaries by thresholding. The reduced drop volume $\tilde{V} = V/r^3 = f(\tilde{n}, \theta)$ is obtained by integrating the cylindrically symmetric barrel profile using its analytical description [13, 14] in terms of the experimentally determined barrel radius $\tilde{n}$ (non-dimensionalized with fiber radius r), and contact angle θ . The contact angle at the fiber is obtained by linear fitting of the cylindrically symmetric barrel profile in the vicinity of the triple contact line. To obtain contact angles for the asymmetric morphologies - which cannot be directly measured - we construct the electrowetting curves for the cylindrically symmetric regime, and extrapolate towards the symmetry-broken regime. This approach is justified by the absence of contact angle saturation, as the electrowetting response curves are linear [12] even for the highest voltage. The error in the critical contact angles is 2° and 4° for the clamshell-to-barrel and barrel-to-clamshell transitions, respectively, and is largely determined by the finite resolution of the contact angle

measurements

Numerical Analysis. The interfacial energies of the barrel and clamshell drops are calculated with the public domain software Surface Evolver [29]. In this program the liquid interface is represented by a triangular mesh of edges. Mechanically stable configurations are determined by minimizing the interfacial energy subject to the global constraint of a fixed volume. In contrast to the volume, the equilibrium contact angle of the liquid is prescribed through the surface energy of the liquid on the fiber. The refinement of the triangulated liquid interface is optimized as a function of the radial distance from the fiber. Along the contact line the maximum ratio between the length of an edge and the fiber radius is 0.015 increasing to 0.3 far away from the fiber. During the energy minimization the liquid interface is allowed to change its topology between a multiply connected barrel configuration and a simply connected clamshell. Owing to the reflection symmetries of the barrel and clamshell states we considered only a quarter of the system.

To determine the stability limit of the barrel morphology we increased the contact angle in small steps of 0.1 degrees starting from a barrel state. During the instability the center of mass of the liquid shifts outward until the topology changes and the interface finally adopts a clamshell state. The same results are obtained by decreasing the volume in steps of 1% for a fixed contact angle. To detect the opposite transition, the drop is initially placed in the clamshell state. The contact angle is decreased in steps of 0.1 degrees, or the volume is increased by 1%, until the drop falls into the barrel state. In a typical run we considered configurations with 600 to 1200 nodes and applied a minimum of 700 complex customized energy minimization steps per step of contact angle or volume. Each minimization step contains refinement and deletion procedures applied to the edges of the mesh in order to guarantee a constant quality of the triangulation. The recorded quantities such as the interfacial energy or the Laplace pressure are obtained with an average of the last 100 steps. The energy minimization procedure for a given contact angle or volume is repeated as long as the energy difference between two subsequent contact angle or volume steps was not smaller than the typical fluctuations caused by re-meshing of the interface. In order to estimate

the error of the stability limits we increased the number of minimization steps or the number of nodes for certain values of volume and contact angle. As the deviations between the points of instability where always less than 0.5 degrees we assume that possible systematic errors are below one degree. To construct the energy landscape of the transition, the additional constraint of a fixed center of mass position $x_{cm}^{\sim}$ (23) is introduced which allows to study intermediate states by varying $x_{cm}^{\sim}$. For each fixed volume and contact angle, the drop is first placed in the barrel state. The drop is then pulled outward beyond the transition to the clamshell state, and subsequently pulled inward beyond the transition to the barrel state. The energy landscape for fixed drop volume is constructed by repeating this procedure for various contact angles.

7.5 Contributions & Acknowledgements

H.B.Eral, R.de Ruiter, J.de Ruiter contributed equally to work presented in this chapter. Simulations were conducted by M.Brinkmann and C.Semprebon. H.B.Eral acknowledges the funding by the Dutch Science Foundation NOW/chemical sciences within the ECHO program.

7.6 Potential applications: Self rejuvenating filter for oil-water separation

The ideas brewed for this chapter of the thesis are fundamental in origin yet they provide inspiration for a new class of materials that might have important applications for industry. In this section, we will elaborate on the idea of using fibers with Electrowetting functionality to design self rejuvenating filters for oil-water separation. In a nut shell, the affinity of oil drops to fibers can be altered by Electrowetting to promote self cleaning. The idea originates from the fundamental difference between two competing morphologies in terms of adhesion. A drop in the symmetric barrel shape adheres strongly to the fiber whereas the same drop in the asymmetric clamshell morphology adheres less strongly. As a consequence,a drop in the clam-shell morphology can be easily detached by an external force such as drag force or gravity. As Electrowetting (EW) provides a mean to reversibly change the morphology of a drop on a fiber, both the affinity of the drop to the fiber and the susceptibility to external driving can be controlled and utilized for novel materials.

In an attempt to provide a rough guideline, we describe the idea for a simplified conceptual application in Fig. 6. An oil-water filter made of a set of fibers aligned in a channel or construct can collect the oil in water as the fibers are hydrophobic in the absence of EW. The collected oil droplets will immediately assume barrel shape due to initially low contact angle (Panel (b) of Fig. 6). As the oil collects on the fibers of the filter, at some point the filter will needs to rejuvenate i.e. get rid of the oil droplets. At that point, applying EW changes the morphology and the affinity of droplets to fibers (Panel (b) to Panel(c) of of Fig. 6) hence promoting detachment of droplets from the fiber . The droplets in clam-shell morphology can be detached from the fibers by an external driving force such as the drag forces induced by an rejuvenating shear flow and the detached oil droplets can be collected in a reservoir outside the regular flow directions. When the rejuvenation process is complete the filter can continue filtering operation (Panel (d) of of Fig. 6).

Self rejuvenating filters can provide interesting applications where

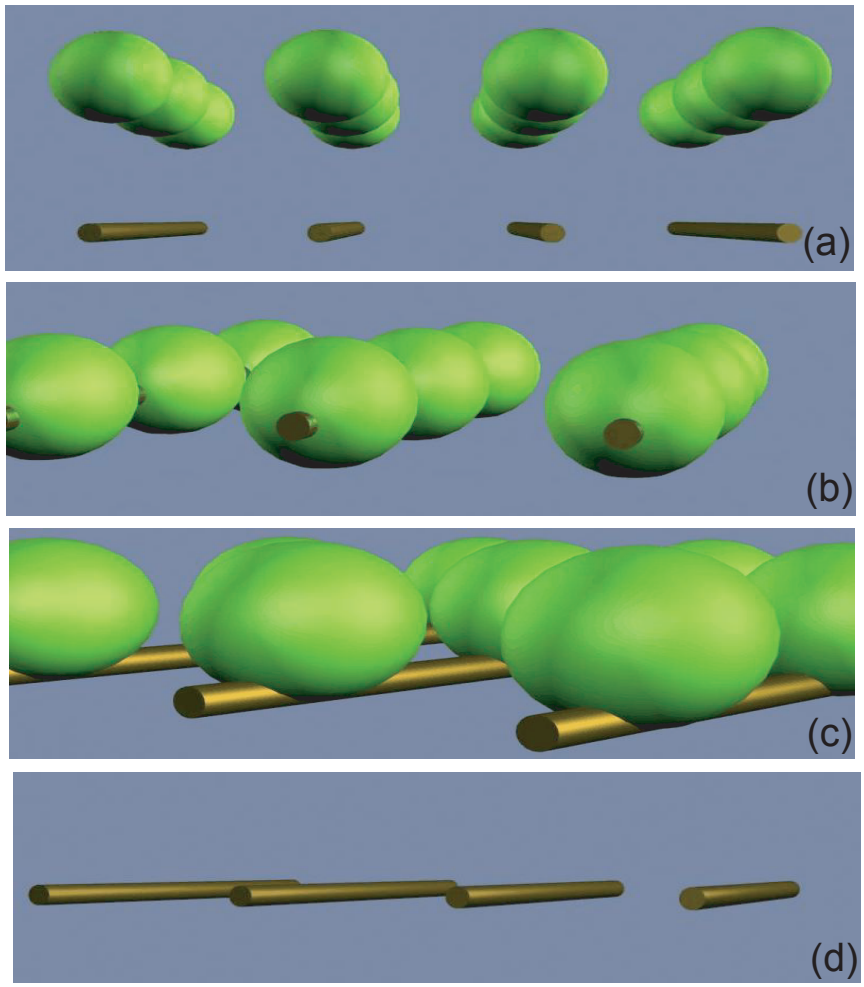

Figure 7.6: Self rejuvenating filters with EW functionality: The oil droplets flow towards the fibers of the filter in Panel (a). The drops immediately assume barrel morphology in Panel (b). Upon application of EW, the droplets change morphology and affinity : from strongly attached barrel morphology illustrated in Panel (b) to weakly attached clam-shell morphology illustrated in Panel (c). With the application of external driving such as rejuvanating shear flows or mechanical shaking the droplets are removed from the fibers (Panel (d)).

batch filtering operations are not feasible, for instance, in cleaning of oil spills where enormous amounts of oil needs to be filtered. In traditional batch filtering, the process is stopped to change or rejuvenate the filter every time the filter is completely filled by oil droplets. The filters with EW functionality can provide alternative continuous filtering where the filter is rejuvenated at regular intervals. The idea presented in this chapter, is not limited to cleaning oil spills but can be evoked to separate any two immiscible liquids often encountered in petrochemical and food industry.

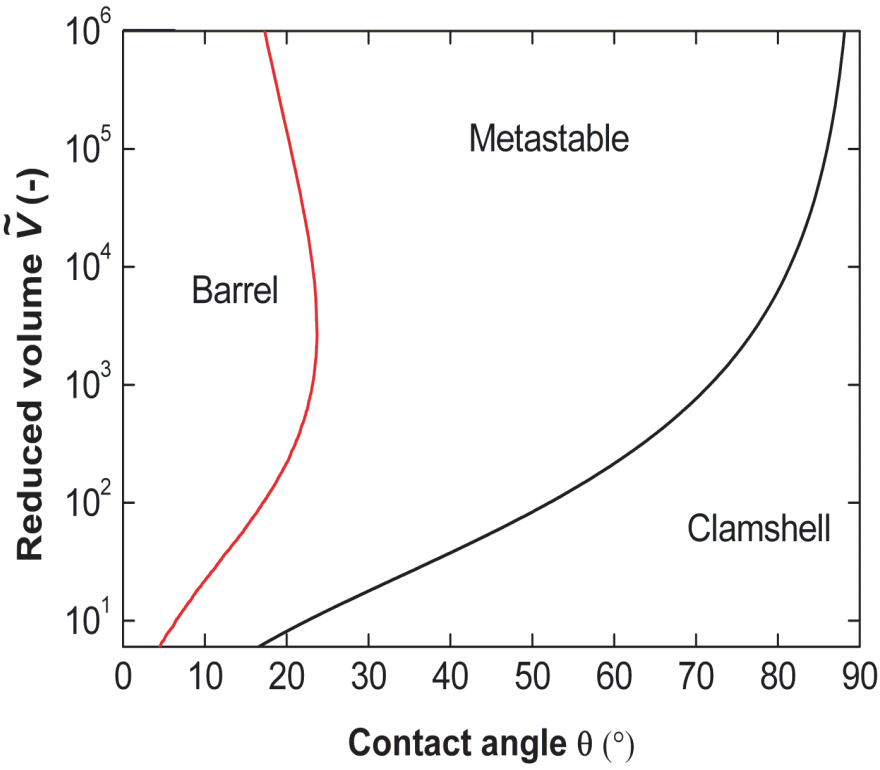

Figure 7.7: Morphology diagram of drops on fibers as a function of contact angle θ and reduced volume $\tilde{V}$, extended to large volumes (up to 10^6). The solid lines indicate the numerical stability limit of the clamshell (upper red) and the (coinciding) analytical and numerical stability limit of the barrel (lower black).

7.7 Appendix: Large drop volume limit

As an additional aspect to Figure 4 in the main text, we have focused on the large drop volume regime in Figure 7.7. The clam-shell to barrel branch of the metastability regime curves towards lower angles. This brings out a interesting feature which we refer as reentrant behavior. At low contact angles and large drop volumes, a drop in

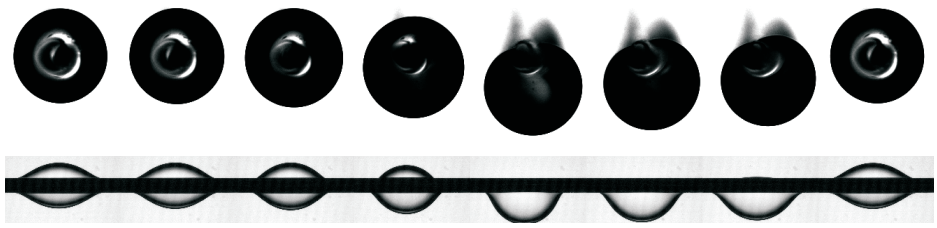

Figure 7.8: Evolution of the drop morphology for one experiment cycle described in Figure 7.2 with pictures taken from side (bottom row) and the head on view (top row) where the contact angle is linearly increased to slightly above the transition contact angle (θ_{c1}) and decreased back to Young angle passing through (θ_{c1}) described in the main text.

clamshell state can enter the barrel morphology region by reducing the drop volume. By reducing the volume further with given contact angle, the drop will enter the metastable regime again and eventually the clam-shell morphology region.

Here we also provide pictures describing the morphological evolution of the drop in one experimental cycle where the voltage is increased in the first four rows and then decreased gradually in the last four linearly in Figure 7.8. Both the morphology evolution is monitored from two different viewing angles: head on (top row) and side (bottom row).

Bibliography

[1] J. Plateau. *Experimental and theoretical statics of liquids subject to molecular forces only. (Translated from French.)*. Gauthier-Villars, Paris, 1873.

[2] L. Rayleigh. On the capillary phenomena of jets. *Proc R. Soc London*, 29:71–97, 1879.

[3] D. Delaunay. On the surface of revolution with constant mean curvature (translated from french.). *J. Mat. Pures et Appl.*, 6:309–320, 1841.

[4] K. Adam. Detergent action and its relation to wetting and emulsification. *JSDC*, 53:121–129, 1937.

[5] P. Lenz and R. Lipowsky. Morphological transitions of wetting layers on structured surfaces. *Phys. Rev. Lett.*, 80(9):1920–1923, Mar 1998.

[6] H. Gau, S. Herminghaus, P. Lenz, and R. Lipowsky. Liquid Morphologies on Structured Surfaces: From Microchannels to Microchips. *Science*, 283(5398):46–49, 1999.

[7] D. Quere. Fluid coating on a fiber. *Annual Review of Fluid Mechanics*, 31(1):347–384, 1999.

[8] R. Seemann, M. Brinkmann, E. J. Kramer, F. F. Lange, and R. Lipowsky. Wetting morphologies at microstructured surfaces. *Proceedings of the National Academy of Sciences of the United States of America*, 102(6):1848–1852, 2005.

[9] A. Lafuma and D. Quere. Superhydrophobic states. *Nature Materials*, 2(7):457–460, 2003.

[10] A. A. Darhuber, S. M. Troian, S. M. Miller, and S. Wagner. Morphology of liquid microstructures on chemically patterned surfaces. *Journal of Applied Physics*, 87(11):7768–7775, 2000.

[11] A. A. Darhuber, S. M. Troian, and W. W. Reisner. Dynamics of capillary spreading along hydrophilic microstripes. *Phys. Rev. E*, 64(3):031603, 2001.

[12] F. Mugele and J. C. Baret. Electrowetting: from basics to applications. *Journal of Physics: Condensed Matter*, 17(28):R705, 2005.

[13] B. J. Carroll. The accurate measurement of contact angle, phase contact areas, drop volume, and laplace excess pressure in drop-on-fiber systems. *J. Coll. Int. Sci.*, 57(3):488 – 495, 1976.

[14] G. McHale, N. A. Kab, M. I. Newton, and S. M. Rowan. Wetting of a high-energy fiber surface. *Journal of Colloid and Interface Science*, 186(2):453 – 461, 1997.

[15] G. McHale and M. I. Newton. Global geometry and the equilibrium shapes of liquid drops on fibers. *Colloids and Surfaces A: Physicochemical and Engineering Aspects*, 206(1-3):79 – 86, 2002.

[16] J. Lyklema, G. Mchale, M. I. Newton, and B. J. Carroll. The shape and stability of small liquid drops on fibers. *Oil Gas Science and Technology - Rev. IFP*, 56(1):47–54, 2001.

[17] B. J. Carroll. Equilibrium conformations of liquid drops on thin cylinders under forces of capillarity. a theory for the roll-up process. *Langmuir*, 2(2):248–250, 1986.

[18] A. Milchev and K. Binder. Polymer nanodroplets adsorbed on nanocylinders: A monte carlo study. *J. Chem. Phys.*, 117(14):6852–6862, 2002.

[19] G. O. Berim and E. Ruckenstein. Cylindrical droplet on nanofibers:? a step toward the clam-shell drop description. *J. Phys. Chem. B*, 109(25):12515–12524, 2005.

[20] E. Lorenceau and D. Quere. Drops on a conical wire. *Journal of Fluid Mechanics*, 510(-1):29–45, 2004.

[21] T. Gilet, D. Terwagne, and N. Vandewalle. Droplets sliding on fibres. *Eur. Phys. J. E*, 31(3):253–262, 2010.

[22] A. Klingner and F. Mugele. Electrowetting-induced morphological transitions of fluid microstructures. *J. Appl. Phys.*, 95(5):2918–2920, 2004.

[23] M. Brinkmann and R. Lipowsky. Wetting morphologies on substrates with striped surface domains. *J. Appl. Phys.*, 92(8):4296–4306, 2002.

[24] M . Brinkmann, J. Kierfeld, and R. Lipowsky. A general stability criterion for droplets on structured substrates. *J. Phys. A: Mathematical and General*, 37(48):11547, 2004.

[25] Y. Zheng, H. Bai, Z. Huang, X. Tian, F. Nie, Y. Zhao, J. Zhai, and L. Jiang. Directional water collection on wetted spider silk. *Nature*, 463(7281):640–643, 2010.

[26] E. Seyrat and R. A. Hayes. Amorphous fluoropolymers as insulators for reversible low-voltage electrowetting. *J. Appl. Phys.*, 90(3):1383–1386, 2001.

[27] J. Buehrle, S. Herminghaus, and F. Mugele. Interface profiles near three-phase contact lines in electric fields. *Phys. Rev. Lett.*, 91(8):086101, 2003.

[28] F. Mugele and J. Buehrle. Equilibrium drop surface profiles in electric fields. *Journal of Physics: Condensed Matter*, 19(37):375112, 2007.

[29] K. A. Brakke. The surface evolver and the stability of liquid surfaces. *Phi Trans R Soc A*, 354:2143–2157, 1996.

8 Wetting of a sphere

Abstract In this chapter, the equilibrium morphology of a drop on a sphere is analyzed as a function of contact angle and drop volume experimentally and with analytic effective interfacial energy calculations. Experimentally, a drop on a sphere geometry is realized in an oil bath by placing a water drop on the sphere coated with a dielectric, of which the radii of curvature are comparable with that of the drop. Electrowetting (EW) is used to change the contact angle of the water drop on the sphere. To validate the applicability of EW and the Lippman-Young equation on non-flat surfaces, we systematically investigated the response of the contact angle to the applied voltage (EW response) for various drop volumes and compared the results with the case of planar surface. The effective interfacial energy of two competing morphologies namely the spherically symmetric "completely engulfing" and the "partially engulfing" morphology are calculated analytically. The analytic calculations are then compared to the experimental results to confirm which morphology is energetically more favored for given contact angle and drop volume. Our findings indicate that the "partially engulfing" morphology is always energetically more favorable morphology.[1]

[1]Experiments presented for this chapter were performed together with G.Manukyan.

8.1 Introduction

Drops on curved surfaces are omnipresent in nature: dew drops on a spider web or a rain drop on a spherical fruit provides the most intriguing display of drop morphologies on curved surfaces (Fig. 8.1). The morphologies that a drop assumes on a curved surfaces are dictated by wettability of the substrate, which is a key parameter for addressing fundamental problems of fluid stability on complex geometries [1, 2]. The wettability of a substrate depends on the interplay between the contact angle and the geometry of the surface. For instance, a drop that partially wets a planar surface can engulf a fiber with same wettability.

The drop on a sphere geometry is not only a classic wetting geometry but also it is often encountered in industrial and fabrication processes. Such processes can benefit from the fundamental understanding of the wettability for the drop on a sphere geometry. Recently, this classic wetting geometry was evoked to synthesize complex colloidal particles by growing a colloidal particle inside a polymer drop. The colloidal particle that is initially in "completely engulfing" morphology later assumes a "partially engulfing morphology" dictated by the wettability. Wettability of the polymer drop on the particle is controlled by the reaction parameters such as monomer concentration and temperature [3, 4]. Various applications in colloidal science [5], microfluidics [6, 7, 8, 9], detergency [10], optofluidic lenses [11], electronic displays utilize spherical and other non-flat geometries [12, 13].

A drop on a sphere can have two topologically distinct morphologies: the "partially engulfing" morphology and the spherically symmetric "completely engulfing" morphology. These two morphologies are fundamentally different in terms of their symmetry and response to external driving such as shear or mechanical agitation. The wettability of a droplet on a spherical surface is addressed in various theoretical studies, [14, 15, 16, 17] yet an experimental setup that allows precise control over parameters that determine the wettability hence the equilibrium morphologies was missing. Previous experimental studies on spherical surfaces [18, 19] utilized different materials to vary the contact angle. These methods do not offer the resolution sufficient accuracy to explore the range of contact angles defining the

morphologies.

For experimental realization of the drop on a sphere geometry, a water drop in an oil bath is placed on a metal sphere coated with a dielectric layer. The wettability of the drop on the sphere is tuned by electrowetting (EW). Electrowetting is an efficient way of controlling the wettability of liquids on surfaces. The effective interfacial tension, or equivalently the apparent contact angle θ of a conducting drop on a dielectric substrate is controlled by applying a potential difference (U) between the conducting liquid and an electrode integrated under the dielectric layer [20]. The difference between the cosine of the apparent contact angle θ and the cosine of the microscopic contact angle θ_Y at the three-phase contact line (TCL) is proportional to the square of the applied potential (U^2) by the Lippmann-Young equation (8.1).

$$\cos\theta = \cos\theta_Y + \eta, \quad \eta \equiv \frac{\varepsilon_0 \varepsilon_r U^2}{2\delta\sigma}, \tag{8.1}$$

where θ_Y is the Young's angle and the electrowetting number η is defined by the vacuum permeability ε_0, the dielectric constant ε_r, the dielectric layer thickness δ, and the interfacial tension σ.

First, we confirm the applicability of the Lippmann-Young equation and EW to study the equilibrium morphology of drops on curved surfaces. For this purpose, the response of the contact angle to the applied voltage (EW response) for a drop on a spherical, a cylindrical and a planar substrate is compared. The drops on planar surfaces follow the Lippmann-Young relation (8.1), the applicability of this relation is confirmed for nonflat surfaces. Furthermore, we investigate EW response on curved surfaces systematically as a function of the drop volume. The volume of the drop is varied to change the relative surface curvature (κ_1/κ_2), where κ_1 and κ_2 are the curvatures of drop and surface, respectively.

The validation of the Lippmann-Young equation for non-flat surfaces is required as the intrinsic curvature of the geometry and dielectric layer thickness influences the electric force distribution in the vicinity of the contact line. In the derivation of 8.1, the force distribution is obtained assuming that the supporting substrate is flat. For a non-flat surface, the electrical force distribution is altered due to

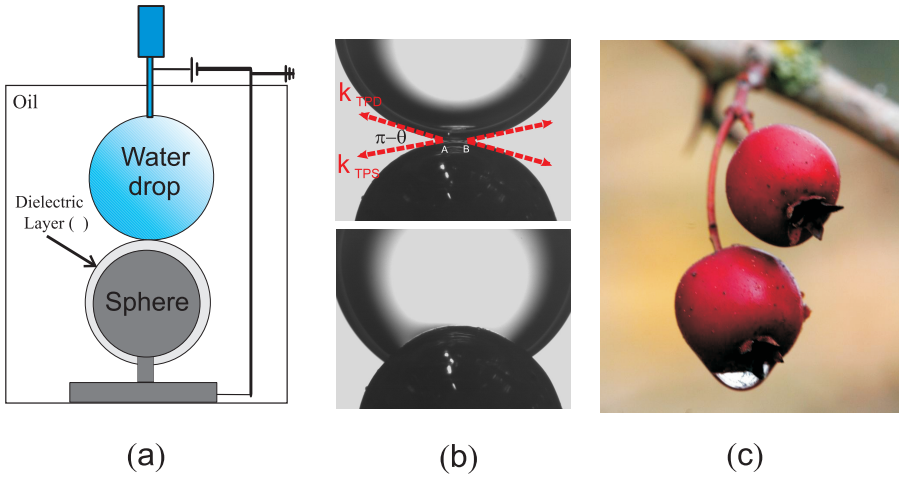

Figure 8.1: Panel (a) shows the experimental setup . The setup consists of a non-flat steel substrate coated with a dielectric layer of thickness (δ) and a water drop placed on the top, immersed in oil. The metal sphere is grounded and the water drop is connected to a power supply in our setup. Panel (b) shows images of the experimental system where the voltage is changed from 0 to 300 V. Panel (c) presents "partially engulfing" morphology from nature, a water drop sitting on a berry courtesy of S.Dreilinger. Note that in nature gravity is ever present as opposed to experiments presented here and it induces additional asymmetry.

the surface curvature and, as a consequence, the wettability change may deviate from the Lippmann-Young relation. Furthermore, this variation might depend on the relative surface curvature and dielectric layer thickness. It has been shown that the electrostatic force in the presence of electrowetting is concentrated near the contact line in a region in the order of the dielectric thickness [21, 22]. From this point, one can hypnotize that the curvature of the sphere will not be dramatically influencing the EW response due to large difference in dimensions considered. We provide experimental confirmation of this hypothesis stating the curvature effects can be ignored in this study.

Secondly, we determine the equilibrium shapes of a drop on a sphere geometry experimentally and analytically relying on the pre-

vious confirmation. The parameter space consisting of contact angle and drop volume is scanned to find the stable morphologies with the experimental setup shown in Fig. 8.1. The effective interfacial energy of the equilibrium morphologies are extracted experimentally by image processing and compared to analytical effective interfacial energy calculations. We believe that our systematic investigation will not only encourage further applications of EW to address fundamental wetting questions [23, 24, 25] where manipulation of contact angle plays an important role for complex geometries [26, 27, 28] but also identify their limitations.

8.1.1 Methods of Analysis

Electrowetting setup

Our buoyancy-neutral experimental setup consists of a stainless steel sphere ($r = 1.5$ mm) coated with a dielectric layer of thickness (spatial variation of δ is between 2 to 4 μm with mean of 3.1 μm) immersed in silicon oil (Fluka AS4 with density $\rho = 1.01$ g/cm^3 and viscosity $\mu = 6$ mPa·s). The experiment is performed in oil to avoid evaporation and to reduce the contact angle hysteresis. The relative importance of gravity over interfacial tension is measured by the Bond number $Bo = \Delta\rho g L^2/\gamma$ where $\Delta\rho$ is the density difference between oil and water phases, L is the characteristic length given by the radius of the drop with maximum drop volume (8 μl). In our density matched experimental setup $Bo \approx 10^{-2}$, in which the gravity effects can be ignored. A function generator (HP33250A) and an amplifier (Trek PZD350) are used to supply the required voltage. A video goniometer (OCA Dataphysics) is used to capture images. We place a water drop on top of the spherical substrates. The volume of the drop is controlled by an automated syringe pump whose needle also acts as an electrode (Fig. 8.1). In these experiments, the volume of the drop (V_{drop}) are varied from 8 to 1 μl, which corresponds to the relative surface curvature κ_1/κ_2 variation from 0.6 to 5.

8.1.2 Substrate preparation

Non-flat substrates are prepared with a cleaning procedure followed by two consecutive dip coating steps. In the first step, the steel spheres are cleaned with ethanol in an ultrasonic bath for 15 minutes and left to dry in a fume hood under ambient conditions. Secondly, the substrates are dip coated with SU-8, then the SU-8 coated substrates are placed on a hot plate for 3 minutes and finally the substrates are UV cured for 30 seconds. In the last step, the SU8 coated spheres are dip coated again with 0.6 wt.% Teflon AF solution. The thickness of the dielectric layer is measured from scratched samples by the Scanning Electron Microscopy (SEM) after the experiments. The SEM images are given in the Supplementary Information.

8.1.3 The free energy calculations

The effective interfacial energies of the two morphologies seen in Fig. 8.2 are analytically calculated as a function of the drop volume and the contact angle. For this purpose, the radius of drop R in the "partially engulfing" morphology can be expressed in terms of a, θ_1, θ_2 with the spherical shape assumption.

$$R = \frac{\sin\theta_1}{\sin\theta_2} a, \tag{8.2}$$

where θ is the contact angle and $\theta_2 = \theta + \theta_1$, the radius of spherical substrate a. Then, the volume V_{drop} of the drop in the "partially engulfing" is expressed as follows:

$$V = \frac{\pi}{3}\left[R^3\left(2 - 3\cos\theta_2 + \cos^3\theta_2\right) - a^3\left(2 - 3\cos\theta_1 + \cos^3\theta_1\right)\right] \tag{8.3}$$

The surface area of the drop (S_1), the drop-substrate contact area (S_2), and the air-substrate contact area (S_3) can be expressed as follows:

$$S_1 = 2\pi R^2\left(1 - \cos\theta_2\right), \tag{8.4}$$

$$S_2 = 2\pi a^2\left(1 - \cos\theta_1\right), \tag{8.5}$$

$$S_3 = 2\pi a^2\left(1 + \cos\theta_1\right). \tag{8.6}$$

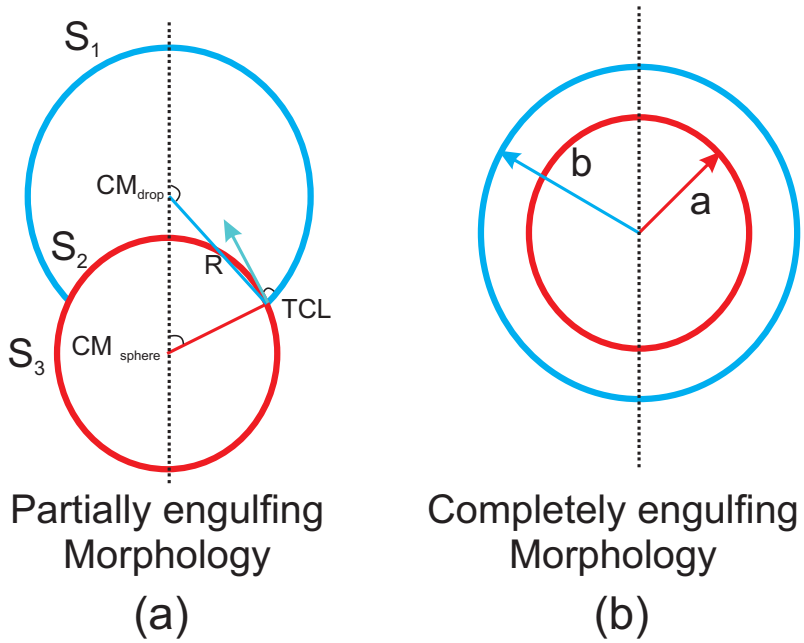

Figure 8.2: Panel (a) shows the "partially engulfing" morphology and (b) the "completely engulfing" geometry. The parameters indicated in the effective interfacial energy calculations are indicated in both panels.

The surface area of the drop (S_4) in contact with oil is given in "completely engulfing" morphology as

$$S_4 = 4\pi b^2, \tag{8.7}$$

where b is the radius of the drop in the "completely engulfing" morphology

$$b = \left(a^3 + \frac{V}{4\pi/3}\right)^{1/3}. \tag{8.8}$$

There is a restriction for θ_1 when determining the equilibrium shape at given drop volume.

$$\frac{\pi}{2} < \theta + \theta_1 < \pi \tag{8.9}$$

The difference $\Delta E = E_1 - E_2$ between the effective interfacial energy of the completely engulfed morphology (E_1) and the partially engulfed

morphology (E_2) is given in 8.10.

$$\Delta E = \left(S_4\gamma + (4\pi a^2)\gamma_{ws}\right) - (S_1\gamma + S_2\gamma_{ws} + S_3\gamma_{so}) \tag{8.10}$$

where γ, γ_{ws} andγ_{so} denote the interfacial tension between water-oil, water-solid and solid-oil phases, respectively. The total effective interfacial energy can be rearranged as follows:

$$\frac{\Delta E}{\gamma} = (S_1 - S_4) + S_3\cos\theta. \tag{8.11}$$

When $\Delta E < 0$, the partially engulfing morphology is the energetically favorable morphology in the parameter space spanned by the droplet V_{drop} and the contact angle θ or else the completely engulfing morphology is the more stable morphology.

8.1.4 Image processing

Contact angle measurements

The images of the drop on spherical substrates are captured with a CCD camera for different voltages hence different contact angles. To measure the (apparent) contact angle θ on non-flat geometries (Fig. 8.1b), a simple thresholding algorithm is used to locate the oil-water-sphere interface. The three-phase contact line (TCL) is detected on this interface. To measure the contact angle θ, two tangent vectors originating from the TCL are needed, one tangential to the drop-oil interface: $\tilde{k}_{TPD}$ and the other tangential to the spherical substrate-oil interface: $\tilde{k}_{TPS}$. Two vectors ($\tilde{k}_{TPD}$, $\tilde{k}_{TPS}$) are defined by the least square fitting method in the vicinity of the TCL (Fig. 8.1b). The angle π-θ between these two vectors gives us θ. The procedure was repeated for the both sides of the TCL (A and B in Fig. 8.1b) and the averaged contact angle is given in this study. The error bound of contact angle measurements is calculated as 3° by varying parameters of the detection algorithm systematically.

Effective interfacial energy calculations from experimental data

The effective interfacial energies of the two morphologies are calculated by extracting the surface areas of each interface from the digital

images indicated in Fig. 8.2. For the "partially engulfing" morphology of three phases in contact: the oil-water drop interface area (S1), the drop-substrate contact area (S2), and the oil-substrate contact area (S3) are considered. For the "completely engulfing" morphology, the sphere is not in contact with the surrounding oil medium so only oil-water drop interface and water-solid contact areas are considered.

Calculation of the effective interfacial energy for the "completely engulfing" morphology (E_1) requires the determination of water drop-solid sphere and water drop-solid contact areas. As these contact areas are not contact angle dependent, provided that the drop volume and the radius of the sphere are known, E_1 can be calculated by multiplying the surface tension of the interfaces with respective contact areas.

For the "partially engulfing" morphology, contact areas S_1, S_2 and S_3 vary with the contact angle θ. E_2 vary with respect to θ and the parameters that vary with respect to θ needs to be identified for calculating E_2. Three parameters are θ_1, θ_2 and R as shown in Fig. 8.2. Provided that with the radius of the solid sphere (a) and the drop volume are known, the parameters θ_1, θ_2 and R are calculated by simple geometric relationship once the three-phase contact line (TCL) and the centers of liquid drop CM_{drop} and sphere CM_{sphere} are known. More specifically, the images allow us to find the CM_{drop} and CM_{sphere} precisely by fitting a circle to the contour of the the drop and the sphere. The θ dependent θ_1, θ_2 can be calculated from inner product of two vectors. The inner product of vector connecting CM_{drop} to CM_{sphere} and vector connecting CM_{drop} to TCL gives θ_2. The inner product of the vector connecting CM_{drop} to CM_{sphere} with the vector connecting CM_{sphere} to TCL gives θ_1. These parameters allow for calculation of contact areas S1, S2, S3 from 8.6. Once the contact areas and the respective surface tension values are known, the effective interfacial energy for the "partially engulfing" geometry (E_2) is calculated.

The effective interfacial energies of two morphologies (E_1, E_2) as a function of θ are later used in 8.11 to calculate the effective interfacial energy difference between the two morphologies. Assuming that the spherical symmetry approximation holds, *i.e.* the drop shape is not disturbed by the wire and gravity.

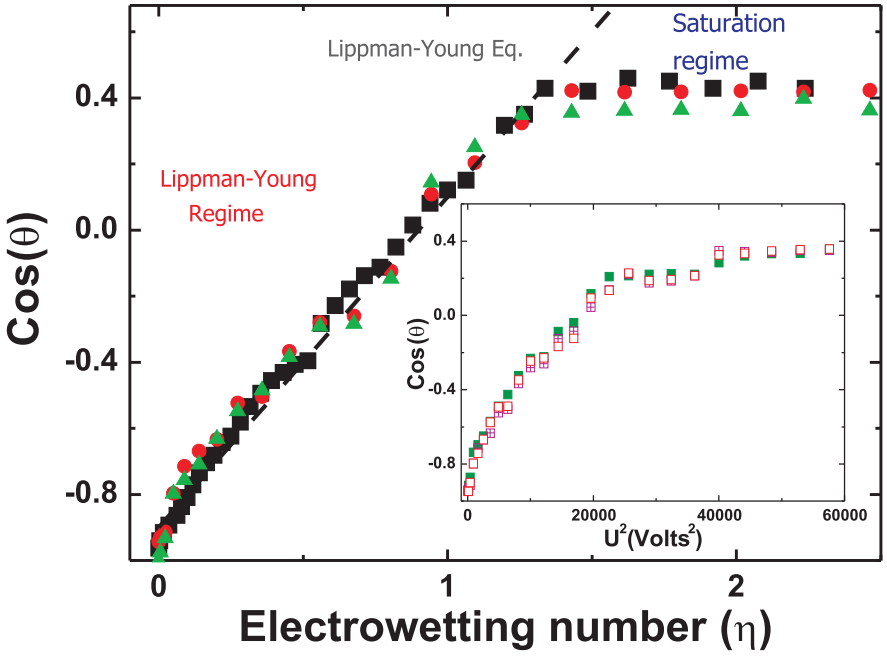

Figure 8.3: Influence of the substrate geometry and the drop volume on the response of contact angle to an applied voltage (EW response). In the main figure, the cosine of the contact angle ($\cos\theta$) is plotted as a function of EW number (η) for different geometries with a given drop volume (V=8 μl). The symbols indicate substrate geometry: cylindrical (triangle), spherical (sphere) and flat (square). The dashed line denotes the Lippmann-Young Equation. In the inset, $\cos\theta$ is plotted as a function of square of U^2 for different drop volumes placed on a spherical geometry. The symbol fill patterns denote different drop volumes V_{drop}: (whole 8 μl, empty 4 μl and crossed 1 μl), respectively.

8.2 Results

To confirm applicability of Lippmann-Young equation for non-flat surfaces, we focus on two parameters a) substrate geometry and the b) drop volume. The responses of contact angle with respect to the applied voltage for different substrate geometries and drop volumes are investigated in Fig. 8.3.

The influence of substrate geometry on EW response is examined for a drop of 8μl volume placed on spherical, cylindrical and planar surfaces. Fig. 8.3 demonstrates how the contact angle changes as a function of the applied voltage and compares the EW response for aforementioned substrate geometries. The cosine of the contact angle ($\cos\theta$) is plotted as a function of the non-dimensionalized EW number to account for variations in δ in Fig. 8.3. The δ is extracted from SEM images (see supplementary information). The curves follow the Lippmann-Young equation in the Lippmann-Young regime followed by the saturation regime where the contact angle does not vary with applied voltage [20].

All the curves in Fig. 8.3 collapse onto the Lippman-Young equation prior to saturation regime, implying that the influence of geometry on EW response is negligible as previously hypnotized. The inset of the Fig. 8.3 displays the influence of the drop volume on the EW response on a spherical substrate. The contact angle ($\cos\theta$) is plotted against square of the applied voltage for different drop volumes in the inset of Fig. 8.3. The collapse of data for different drop volumes (denoted by symbol fill patterns in Fig. 8.3) in the Lippmann-Young regime points out that the drop volume hence relative curvature has no influence on the response of contact angle to the applied voltage for spherical substrates.

After validating the applicability of the Lippmann-Young equation and the reliability of EW on spherical substrates, we investigate the equilibrium morphologies of two morphologies by comparing the effective interfacial energies of the partially engulfing and the completely engulfing morphologies in Fig. 8.2. To assess which morphology is more favorable, we calculate the effective interfacial energy difference between two morphologies (8.10). When $\Delta E \geq 0$, the completely engulfing morphology is the energetically favorable morphology and $\Delta E \leq 0$ the partially engulfing is the favorable morphology.

Evaluation of the drop morphology as a function of contact angle is monitored by plotting the projected distance $d(\theta)$ in two dimensions between the center of mass CM_{sphere} of the solid sphere and the center of mass of the drop $CM_{droplet}$ at a given contact angle in Fig. 8.4a from experimental images (Fig. 8.4c). With increasing contact angle, $d(\theta)$ gradually decreases and the drop partially engulfs more of the sphere

for all drop volumes. To characterize equilibrium shapes for different drop volumes, we defined a symmetry parameter: λ which denotes the relative distance $d(\theta)$ at a given contact angle normalized by the same distance at the Young's angle $d(\theta_Y)$ in 8.12. For a given contact angle, λ is determined from experimental images as follows: the center of mass for the drop: CM_{drop} and sphere:CM_{sphere} are determined by identifying the contour of the drop-sphere via thrash holding and fitting a circle above and below TCL. The distance between CM_{drop} and CM_{sphere} is determined $d(\theta)$ for a given contact angle. The ratio of this distance at a given contact angle to this distance at Young angle:$d(\theta_Y)$ gives the symmetry parameter 8.12. The inset schematic in Fig. 8.4b demonstrates the symmetry parameter.

$$\lambda = \frac{d(\theta)}{d(\theta_Y)} \tag{8.12}$$

For $\lambda \cong 0$ the drop is in "completely engulfing" morphology whereas for $\lambda > 0$ the drop is in "partially engulfing" morphology. Fig. 8.4b demonstrates the variation of λ as a function of contact angle (θ) for aforementioned drop volumes. The curves of different drop volumes collapse onto a single curve and none of the curves reaches the $\lambda \simeq 0$, hence the "partially engulfing" morphology is always the preferred morphology.

The effective interfacial energy difference (ΔE) is calculated analytically and from experimental data as described in detail in the Methods section. Fig. 8.5 shows the effective interfacial energy difference normalized by $4\pi a^2\gamma$ as a function of the contact angle for different drop volumes. The solid lines denote the analytical effective interfacial energy calculations whereas the discrete points indicate the effective interfacial energies calculated from the experimental data.

For all the effective interfacial energy calculations considered here, the effective interfacial energy difference indicates that the favorable morphology is the "partially engulfing" morphology irrespective of the drop volume and the contact angle. These results are in agreement with the effective interfacial energy analysis given in Fig. 8.4. Only when the contact angles approach to zero contact angle, the energy difference converges to zero.

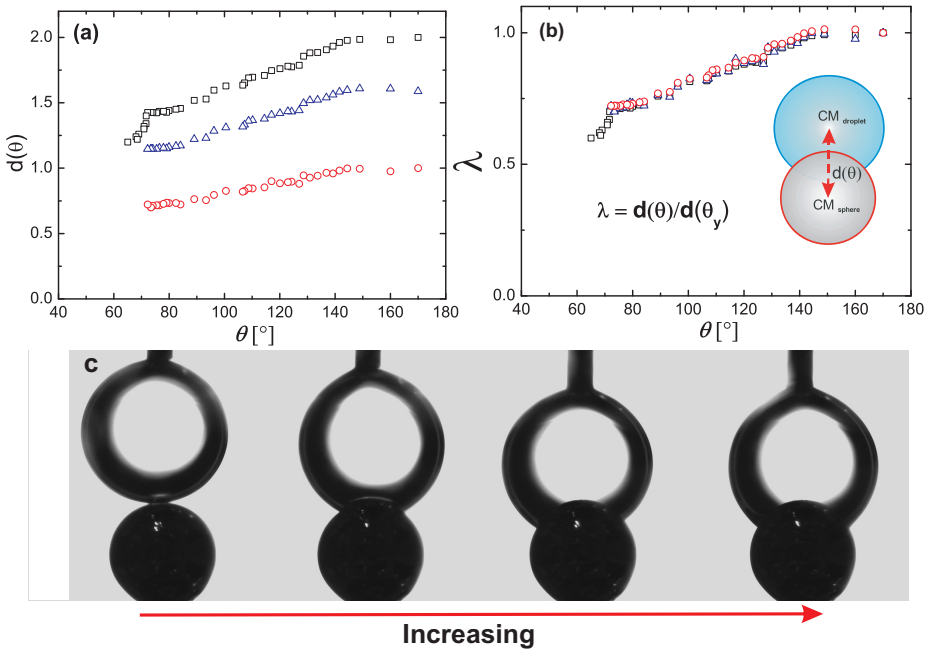

Figure 8.4: Evolution of the drop morphology as a function of drop volume V_{drop} and contact angle θ. Panel (a) provides the distance between the center of mass of drop and the sphere ($\dot{(}\theta$)) as a function of θ for different drop volumes. Panel (b) gives the symmetry parameter (λ) vs. θ . Different symbols correspond to drop volumes (1 μl ($\bigcirc$), 4 μl ($\triangle$), 8 μl ($\square$) respectively. The symmetry parameter (λ) is defined as the distance $\dot{(}\theta$) between the center of mass of the sphere and the drop at a givenθ normalized by$\dot{(}\theta_Y$): the distance when θ is equal to θ_Y . Inset in panel (b) demonstrates the $\dot{(}\theta$) and symmetry parameter. Panel (c) provides an overview of the experimental images for various θ.

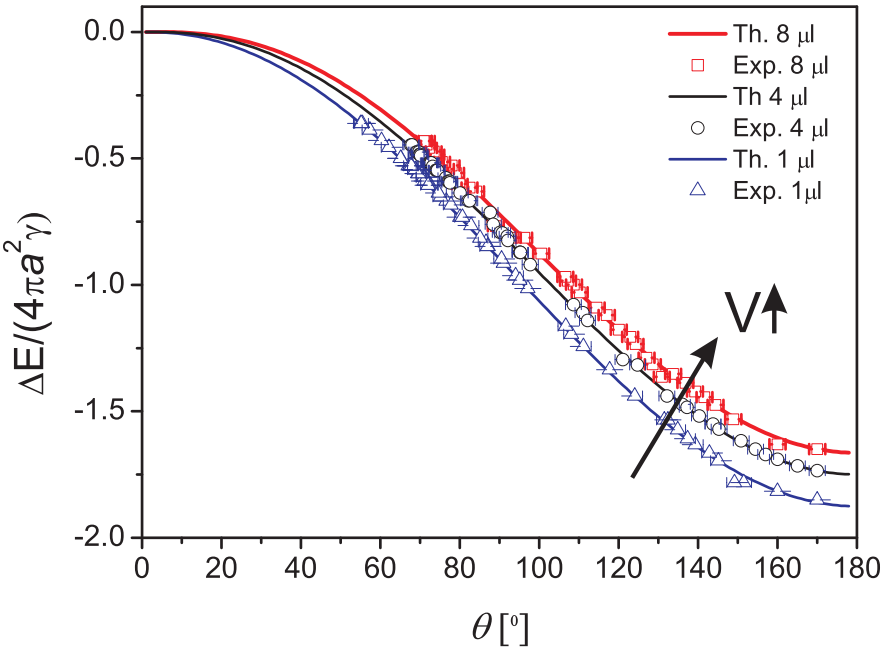

Figure 8.5: Normalized effective interfacial energy is plotted as a function of contact angle for different drop volumes used in experiment. Continuous lines indicate the theoretical and the discrete points of same color indicate experimental effective interfacial energies extracted from image processing. Different symbols correspond to drop volumes (1 μl (◯), 4 μl (△), 8 μl (□) respectively.

8.3 Discussions

In the first part of the paper, we investigated the applicability of Lippmann-Young Equation and the reliability of EW to the purpose of drop morphology analysis on curved surfaces by varying two parameters: substrate geometry and drop volume. Fig. 8.3 confirms the applicability of the Lippmann-Young equation to non-flat geometries as well as flat geometries in the Lippman-Young regime. Hence the effect of the geometry and the relative curvature in our experimental parameter space can be ignored. We have also looked at the influence of drop conductivity on EW response for spherical substrates.

Dependence of EW response on drop conductivity is found to follow similar behavior as in planar surface[29, 30, 31] (see Supplementary Info for details).In 8.3 and its inset, a slight scattering and deviation from the Lippmann-Young Eq. is observed. This is attributed to a spatial variation in dielectric layer thickness of samples used in experiments which we have identified to vary between 2-5 microns.

Ch8Finally, the effective interfacial energy difference (ΔE) between the two morphologies is calculated analytically and from experimental data in 8.5. ΔE always lies in negative region indicating that the "partially engulfing" morphology is the favored morphology irrespective of the drop volume and the contact angle. At zero contact angle, the effective interfacial energy of the two competing morphologies becomes identical, which means that the surface energy of the wetted area is the same with that of non-wetted area ($\gamma + \gamma_{sw} = \gamma_{so}$). Due to contact angle saturation phenomena, very low contact angles cannot be reached experimentally yet the analytical effective interfacial energy calculations show that the two morphologies has equal effective interfacial energies indicating that the two morphologies are equally favorable for zero contact angle. It implies that with large enough drops and zero contact angle a transition from one morphology to the other is theoretically possible.

In this study, the upper and lower bounds of drop volume considered are defined by the limitations of the experimental setup and the associated physics. The smallest volume utilized is bound by the size of wire in conventional EW setup (The drop diameter has to be a lot bigger than the wire). The upper limit is bound by the capillary limit. Provided that we are not limited by the experimental parameters these two extreme limits may provide interesting insights. For the generality of our results, it is relevant to discuss these extreme cases: when (i) the drop volume: V_{drop} is a lot larger then the volume of the sphere V_{sphere} i.e. $V_{drop} >> V_{sphere}$ and (ii) the other extreme $V_{drop} << V_{sphere}$. In case (i), from the the effective interfacial energy calculations, we can deduce that the larger the ratio of V_{drop} to V_{sphere} the smaller the difference ΔE. This points out the effective interfacial energy of two states become comparable at all contact angles. In other words, ΔE vs θ landscape approaches $\Delta E = 0$ line, *i.e.* less energy is required to jump from one morphology to the other upon

application of flow or mechanic agitation. For case (ii), the transition becomes rather difficult and the systems resembles the flat geometry.

The major source of error in the calculation of the effective interfacial energy from experiments is the determination of the contact angle in image processing. The error bound of measurement is within 3°. As the experimental and theoretical values collapse for all the drop volumes effects that deform the drop such as contact angle hysteresis, gravity and wire are not significant.

Utilizing EW to study fundamental wetting problems in complex geometries provides unmatched control over the contact angle. Yet the limitations in EW should not be neglected. The contact angle saturation does not allow reaching contact angles smaller that 35°. This limitation can be avoided by evoking inverse EW scheme where a water drop is immersed in oil yet it has to be identified as a limitation of the method [27]. Conventional and inverse EW schemes can be used in parallel to reach larger contact angle ranges. Special care has to be taken for the conventional EW setup we utilized, as the wire has to be much smaller than the drop to minimize its effect on the symmetry of the system. Interdigitated electrode or inverse EW setups can be evoked to bypass this effect. In our study, we monitored the symmetry of the drop and manually interfered by moving the wire when the symmetry is compromised.

Our results demonstrate the wetting behavior of a liquid drop on a spherical surface. Comparing this behavior to the wettability of a liquid drop on a infinitely long cylindrical fiber points to some interesting differences. Ch8Fibers can be fully engulfed with a nonzero contact angle where the contact angle has to be infinitesimally small for a drop on sphere for complete engulfment [32, 27, 10]. The critical contact angle, at which a drop engulfs a fiber, depends on the drop volume whereas for the drop on a sphere geometry such critical contact angle is not drop volume dependent. From a topological point of view, the "partially engulfing" morphology is a singly connected topology once the drop engulfs the sphere, spherical symmetry is established. For a fiber, asymmetric morphology is singly connected, while the symmetric morphology is multiply connected. This topological difference is one of the underlying physical reasons why the wetting behavior of two geometries are different.

8.4 Conclusions

In the present work, we first validated EW as a tool to study wetting problems of non-flat geometries. Later on, relying of this validity, we confirmed the equilibrium morphologies of a classic wetting geometry: drop on a sphere as a function of governing variables drop volume and contact angle, experimentally and analytically.

For validation purposes, the influence of substrate geometry on the EW response is studied systematically considering the effect of drop volume hence relative curvature. For different drop volumes corresponding to different relative drop to substrate curvatures, EW response stayed same, indicating that in the experimental parameter regime covered curvature effects can be ignored. Comparing the response of contact angle to the EW number (η) for flat, cylindrical and spherical geometries, we conclude substrate geometry has no influence on EW response. Our results indicate that the Lippmann-Young equation holds for spherical substrates as in flat substrates within the experimental parameters examined. Furthermore, we hypothesize that the effect of substrate curvature can be ignored for cases where the dielectric layer thickness is much smaller that characteristic dimension of the geometry such as the radius of curvature of surface ($\delta \ll \kappa_2$).

Relying on applicability of EW on non-flat surfaces, the equilibrium morphologies of two competing geometries is studied by calculating the effective interfacial energy of both morphologies analytically and experimentally. Our results show that the "partially engulfing" morphology is the energetically more favorable and the mechanically stable morphology as the absolute effective interfacial energy of the engulfing morphology is greater that the "partially engulfing" morphology under all conditions. Only for vanishing contact angles, the effective interfacial energy of the "completely engulfing" morphology is comparable to the "partially engulfing" morphology. It is noteworthy to mention that application of EW to wetting problems in complex geometries opens alleys to explore industrially relevant problems such as mechanical stability of liquid bridges between non-flat geometries such spheres or fibers.

8.5 Contributions & Acknowledgements

H.B.Eral and G.Manukyan conducted the experiments together. H.B.Eral acknowledges the funding by the Dutch Science Foundation NOW/chemical sciences within the ECHO program, A.Staicu for early experiments, B.M.Mognetti for fruitful discussions, K.Smit for mechanical assistance and C.Aran & M.Bikel of MTG group at University of Twente for SEM images.

Bibliography

[1] P. G. de Gennes, F. Brochard-Wyart, and D. Quere. *Capillarity and wetting phenomena: Drops, bubbles, pearls, waves*. Springer, New York, 2004.

[2] J. Plateau. *Experimental and theoretical statics of liquids subject to molecular forces only. (Translated from French.)*. Gauthier-Villars, Paris, 1873.

[3] E. B. Mock, H. De Bruyn, B. S. Hawkett, R. G. Gilbert, and C. F. Zukoski. Synthesis of anisotropic nanoparticles by seeded emulsion polymerization. *Langmuir*, 22(9):4037–4043, 2006.

[4] D. J. Kraft, W. S. Vlug, C. M. van Kats, A. van Blaaderen, A. Imhof, and W. K. Kegel. Self-assembly of colloids with liquid protrusions. *Journal of the American Chemical Society*, 131(3):1182–1186, 2009.

[5] H. B. Eral, D. van den Ende, F. Mugele, and M. H. G. Duits. Influence of confinement by smooth and rough walls on particle dynamics in dense hard-sphere suspensions. *Phys. Rev. E*, 80(6):061403, Dec 2009.

[6] D. Psaltis, S.R. Quake, and C. Yang. Developing optofluidic technology through the fusion of microfluidics and optics. *Nature*, 442(7101):381, 2006.

[7] S. K. Cho, H. Moon, and C. J. Kim. Creating, transporting, cutting, and merging liquid droplets by electrowetting-based actuation for digital microfluidic circuits. *JMEMS*, 12(1):70–80, 2003.

[8] B. M. Mognetti and J. M. Yeomans. Capillary filling in microchannels patterned by posts. *Phys. Rev. E*, 80(5):056309, Nov 2009.

[9] B. M. Mognetti and J. M. Yeomans. Using electrowetting to control interface motion in patterned microchannels. *Soft Matter*, 6:2400–2402, 2010.

[10] B. J. Carroll. *Colloids and Surfaces A*, 74(2-3):131 – 167, 1993.

[11] J. Heikenfeld, K. Zhou, E. Kreit, B. Raj, S. Yang, B. Sun, A. Milarcik, L. Clapp, and R. Schwartz. Electrofluidic displays using young-laplace transposition of brilliant pigment dispersions. *Nature Photonics*, 3:292–296, 2009.

[12] K. Zhou and J. Heikenfeld. Arrayed electrowetting microwells. *Applied Physics Letters*, 92(11):113515, 2008.

[13] J. Chen. Electrowetting-actuated zoom lens with spherical-interface liquid lenses. *Journal of the Optical Society of America A*, 25(11):2644, 2008.

[14] R. Hołyst and A. Poniewierski. Wetting on a spherical surface. *Phys. Rev. B*, 36(10):5628–5630, Oct 1987.

[15] P. J. Upton, J. O. Indekeu, and J. M. Yeomans. Wetting on spherical and cylindrical substrates: Global phase diagrams. *Phys. Rev. B*, 40(1):666–679, Jul 1989.

[16] I. A. Hadjiagapiou. Wetting on a spherical-shell substrate. *J. Phys. Chem. B*, 101(44):8990–8996, 1997.

[17] M. C. Stewart and R. Evans. Wetting and drying at a curved substrate: Long-ranged forces. *Phys. Rev. E*, 71(1):011602, Jan 2005.

[18] C. W. Extrand and S. I. Moon. Contact angles on spherical surfaces. *Langmuir*, 24(17):9470, 2008.

[19] G. Mason and W.C. Clark. Liquid bridges between spheres. *Chemical Engineering Science*, 20(10):859 – 866, 1965.

[20] F. Mugele and J. C. Baret. Electrowetting: from basics to applications. *Journal of Physics: Condensed Matter*, 17(28):R705, 2005.

[21] F. Mugele and J. Buehrle. Equilibrium drop surface profiles in electric fields. *Journal of Physics: Condensed Matter*, 19(37):375112, 2007.

[22] J. Buehrle, S. Herminghaus, and F. Mugele. Interface profiles near three-phase contact lines in electric fields. *Phys. Rev. Lett.*, 91(8):086101, Aug 2003.

[23] M. Callies and D. Quere. *Soft Matter*, 1:51–65, 2005.

[24] S. Herminghaus, M. Brinkmann, and R. Seemann. Wetting and dewetting of complex surface geometries. *Annual Review of Materials Research*, 38(1):101–121, 2008.

[25] B. M. Borkent, S. de Beer, F. Mugele, and D. Lohse. On the shape of surface nanobubbles. *Langmuir*, 26(1):260–268, 2010.

[26] M. Brinkmann and R. Lipowsky. Wetting morphologies on substrates with striped surface domains. *Journal of Applied Physics*, 92(8):4296–4306, 2002.

[27] H. B. Eral, J. de Ruitera, R de Ruiter, J. M. Oh, C. Semprebon, M. Brinkmann, and F. Mugele. Drops on functional fibers: from barrels to clamshells and back. *Soft Matter*, 2011.

[28] J.-C. Baret, M. Decra, S. Herminghaus, and R. Seemann. Electroactuation of fluid using topographical wetting transitions. *Langmuir*, 21(26):12218–12221, 2005.

[29] T. B. Jones, Y. S. Fowler, J. D.and Chang, and C.-J. Kim. Frequency-based relationship of electrowetting and dielectrophoretic liquid microactuation. *Langmuir*, 19(18):7646–7651, 2003.

[30] T. B. Jones. On the relationship of dielectrophoresis and electrowetting. *Langmuir*, 18(11):4437–4443, 2002.

[31] K. H. Kang. How electrostatic fields change contact angle in electrowetting. *Langmuir*, 18(26):10318–10322, 2002.

[32] B. J. Carroll. Equilibrium conformations of liquid drops on thin cylinders under forces of capillarity. a theory for the roll-up process. *Langmuir*, 2(2):248–250, 1986.

Summary

In this thesis, we developed ideas to control the structure and the dynamics of colloidal suspensions by manipulating the boundary conditions and applying external fields. The aforementioned manipulations of colloidal fluids not only provide opportunities to improve our understanding of fundamental physical phenomena, but also initiate ideas for developing advanced materials. External control over colloidal suspensions with hard-sphere like interactions -arguably the simplest model system for soft matter studies- can be evoked to tune the interplay between structure and dynamics for both equilibrium and out-of-equilibrium systems. Interplay between structure and dynamics is commonly encountered in Soft Matter systems including but not limited to colloidal suspensions, emulsions, polymers, polyelectrolydes and proteins.

In **Chapter 1** of the thesis, an introduction to colloidal suspensions (in broader terms Soft Matter or Complex Fluids) is presented, going all the way back to the early scientific discussions regarding Brownian motion that lead to our current understanding of colloidal suspensions. In this chapter, a solid basis for understanding the discussions in the upcoming chapters is provided along with a brief account of literature in the field. The experimental methods utilized throughout the thesis are described in detail in **Chapter 2**.

External control over colloidal suspensions can be achieved by manipulation of the interaction potential, the shape of the colloidal particle, spatial boundary conditions and the application of external fields. This thesis focuses external control of spherical particles with hard-sphere like interactions via manipulation of boundary conditions and external fields. The influence of boundary conditions can be visualized starting from a simple picture of colloidal particles in bulk exhibiting Brownian motion. Particles are free to enter and exit an imaginary box while keeping the number of particles constant,

i.e. the boundary conditions are periodic. Introducing confinement can be interpreted as transforming the boundary conditions of one or more sides of the box to 'no-trespass' conditions. This transformation brings out interesting new properties as compared to bulk. In terms of phase behavior, it effectively reduces the possible configurations a particle can explore and introduces layering in the vicinity of boundaries. For monodisperse particles, layering and crystallization are intimately related. For polydisperse particles (as considered in this thesis), crystallization does not occur, and layering solely involves the ordering of particles perpendicular to the boundary. Besides that, the introduction of a solid surface also modifies the dynamics in the vicinity of the boundaries by introducing additional drag forces. All these changes influence the interplay between structure and dynamics. In this thesis, the main focus is to understand how this interplay works and how it can be controlled via boundary conditions of the system and external fields.

Chapter 3 focuses on the effect of spatial confinement, particularly in connection to gravity and roughness. In this study, both the dynamics and the structure of concentrated colloidal suspensions (particle volume fraction ϕ: 0.30-0.45) are probed with Confocal Scanning Laser Microscopy (CSLM) and particle tracking as the dimensions of the imaginary box described before is varied. For varying the dimension of confined colloidal suspensions, a confinement apparatus utilizing a quasi-parallel geometry is designed. Confinement apparatus simultaneously fulfills the spatial control and low drift requirements essential in the confinement experiments for colloidal suspensions. In the experiments, only the top and the bottom boundaries of the imaginary box are transformed into solid planes, particles could freely enter and exit from the other four planes. Two different boundary conditions are utilized: one of the planes is rough and the other one is smooth compared to the particle diameter. As the height of the imaginary box is reduced quasi-statically from 18 to 1 particle diameter, the dynamics slows down while the volume fraction stays essentially constant. Furthermore, an asymmetry is observed in the dynamics and structure of the suspension as measured at the two boundary planes. This is attributed to a combined effect of roughness and gravity.

Apart from the dimensions also the shape of the imaginary box influences the aforementioned dynamics. In **Chapter 4**, we focus on the dynamics of dilute suspensions ($\phi << 0.1$) confined in a well-defined 3D cylindrical geometry. The diffusion of colloidal particles of approximately one micron diameter (d) is studied in a cylinder of comparable size (Radius, Height=9d). A multilayer microfluidic device is used for confining colloidal particles in aforementioned cylinders. Local diffusion coefficients are measured experimentally with particle tracking from video recordings via CSLM. The experimental values are compared to simulation results where the drag force on a particle, and from it the diffusion constant, is calculated as a function of position within the cylinder by solving the Navier-Stokes equation. The experimental results and simulations showed very good agreements. The diffusion inside the cylinder is observed to be asymmetric, hindered compared to the diffusion in bulk and highly dependent on the geometry. Our findings point out that geometry of confinement has to be taken into account precisely while studying diffusion related (bio)physical transport phenomenon in confined environments such as cells or blood vessels.

Motivated by the studies in **Chapter 3**, we focused on the effect of wall roughness on the local dynamics and structure of suspensions in **Chapter 5**. In this study, diffusion as a function of volume fraction in the vicinity of a single boundary with well defined roughness is considered. The roughness is controlled by partially coating a flat wall with slightly smaller colloidal particles than the ones in the suspension. The local volume fraction ($\phi \approx$ 0-0.4) is varied via slow sedimentation. As the volume fraction increases, the dynamics in the vicinity of the boundary slows down, while also the signature of the motion changes: from diffusive motion to 'cage rattling'. Comparing the dynamics in the vicinity of the rough and the smooth walls, a much slower dynamics in the vicinity of the rough boundary as a function of time and effective volume fraction reveals the principal effect of wall roughness.

Regarding external fields, we focus on gravity within the context of confinement in **Chapter 3** & **5** and on shear flows induced by Electrowetting in **Chapter 6**. Gravity is a homogeneous time invariant field whereas shear flows can be both spatially and temporally vari-

ant. The spatial and temporal variance of shear flows can be put to advantage in the manipulation of colloidal assemblies. In **Chapter 6**, we study evaporating colloidal suspensions on a solid surface. Evaporating drops of colloidal suspensions and solutions of non-volatile species often leave behind ring-like solid residues along the contact line. These structures so called "coffee stains" are induced by contact line pinning and capillary flows resulting in an inhomogeneous distribution of solutes. Coffee stains are undesired, self assembled structures commonly encountered in coating and printing applications. Combinatorial analysis methods such as as fluorescent microarrays and MALDI-MS; the workhorses of biomolecular analysis, are specific examples where the inhomogeneity of the residual deposits compromises the overall performance. In an evaporating droplet, colloidal particles are carried to the contact line by capillary flows, and get jammed due to geometric confinement and high volume fractions along the contact line. In this chapter, a method to eliminate the undesired coffee stains is described. The method utilizes the motion of the contact line and shear flows induced by Electrowetting to eliminate the coffee stain effect. Shear flows erode/unjam particles in the vicinity of the contact line and counteract capillary flows whereas the motion of the contact line avoids pinning. We demonstrated the applicability of the suggested method for various solutes including suspensions of colloidal particles with various sizes, materials and DNA. Combined with smart electrode design, this method provides a remedy for the coffee stain effect that hampered the efficiency of various industrial processes. We believe the suggested method can have immense impact especially in improving the efficiency of the combinatorial analysis methods.

In broad terms, the wetting behavior of a Soft Matter system can be considered as a boundary condition. The manipulation of wettability is essentially altering the contact angle boundary condition in the governing equations that define the morphology of the system: a liquid drop on a surface will assume the morphology that minimizes the effective interfacial energy with given boundary conditions. Along these lines, Electrowetting provides a crucial tool to manipulate Soft Matter. Using Electrowetting, we alter the apparent contact angle hence the boundary condition for a liquid drop and observe the

macroscopic morphology that minimizes the effective interfacial energy. In **Chapter 7** & **8**, we investigated the classic wetting problem of a drop on a fiber and later the wetting of a drop on a sphere.

For the drop on a fiber geometry discussed in **Chapter 7**, we confirm that the drop can assume two competing morphologies dictated by the contact angle and drop volume relative to fiber diameter cubed. For small contact angles and large relative drop volumes, the drop engulfs the fiber and assumes the "barrel morphology"; whereas for large contact angles and small relative volumes, the drop sits on the side of the fiber assuming the "clam-shell morphology". By scanning the morphology phase diagram spanned by contact angle and relative drop volume, we discover a previously unexplored bistability regime and reveal the complete nature of transition between two competing morphologies. Furthermore, ideas incubated in this study, point to a potential application of 'self rejunavating fibers' with Electrowetting functionality that could be used to separate oil from water. For the sphere on drop geometry in **Chapter 8**, we study the equilibrium morphologies as a function of contact angle and drop volume. We confirm the predictions from free energy calculations with experimental results and determine under which conditions the drop will engulf the sphere. We believe that our results may open up possibilities to further extend the notion of utilizing wettability to synthesize complex colloidal systems.

Samenvatting

In dit proefschrift hebben we ideeën ontwikkeld om de structuur en de dynamica van colloïdale suspensies te controleren door het manipuleren van de randvoorwaarden en de toepassing van externe velden. De bovengenoemde manipulaties van colloïdale vloeistoffen bieden niet alleen mogelijkheden om ons begrip van de fundamentele fysische verschijnselen te verbeteren, maar leiden ook tot ideeën voor het ontwikkelen van geavanceerde materialen. Externe controle over de colloïdale suspensies met 'harde-bol' achtige interacties -misschien wel het eenvoudigste model systeem voor zachte materie studies- kan worden opgeroepen om de wisselwerking tussen structuur en dynamica voor zowel evenwicht en uit-evenwicht systemen af te stemmen. Wisselwerking tussen structuur en dynamica komt vaak voor in Soft Matter systemen zoals o.a. colloïdale suspensies, druppels, polymeren, polyelectrolyten en eiwitten.

In Hoofdstuk 1 van het proefschrift wordt een inleiding gegeven in de colloïdale suspensies (in bredere termen Soft Matter of Complex Fluids), die teruggaat naar het begin van de wetenschappelijke discussies over Brownse beweging die leidden tot ons huidige begrip van colloïdale suspensies. In dit hoofdstuk wordt een solide basis gegeven voor het begrijpen van de discussies in de daarop volgende hoofdstukken, samen met een korte uiteenzetting van de literatuur op dit vlak. De experimentele methoden gebruikt voor dit proefschrift worden in detail beschreven in Hoofdstuk 2.

Externe controle over colloïdale suspensies kan worden bereikt door manipulatie van de interactie potentiaal, de vorm van de colloïdale deeltjes, ruimtelijke randvoorwaarden en de toepassing van externe krachten. Dit proefschrift richt zich op externe controle van deeltjes met een 'harde bol' potentiaal via manipulatie van de randvoorwaarden en externe velden. De invloed van de rand-voorwaarden kan gevisualiseerd worden met conceptueel plaatje van colloïdale deeltjes

in de bulk die een Brownse beweging vertonen. De deeltjes zijn vrij om een denkbeeldige doos te betreden en te verlaten terwijl het totaal aantal deeltjes constant blijft. De randvoorwaarden zijn periodiek. Het opleggen van randvoorwaarden brengt interessante nieuwe eigenschappen in vergelijking met bulk. In termen van fase gedrag, vermindert het aantal mogelijke configuraties dat een deeltje kan verkennen en dit zorgt voor een gelaagde vloeistofstructuur in de nabijheid van vaste wanden. Voor deeltjes met exact dezelfde afmetingen, zijn gelaagdheid en kristallisatie nauw verwant. Bij deeltjes waarbij de afmeting een verdeling vertoont (zoals in dit proefschrift), heb je geen kristallisatie, en heeft laagvorming uitsluitend betrekking op de ordening van deeltjes loodrecht op de wand. Naast de invoering van een stevige ondergrond wijzigt ook de deeltjes dynamica in de nabijheid van de grenzen door de invoering van extra 'drag forces'. Al deze veranderingen hebben invloed op de wisselwerking tussen de structuur en de dynamica. In dit proefschrift gaat het erom, te begrijpen hoe dit samenspel werkt en hoe het kan worden beïnvloed via de randvoorwaarden van het systeem en externe velden.

Hoofdstuk 3 richt zich op het effect van ruimtelijke opsluiting van de deeltjes, met name in combinatie met de zwaartekracht en de ruwheid van de wand. In deze studie worden zowel de dynamica als de structuur van geconcentreerde colloïdale suspensies (deeltje volumefractie ϕ: 0.30 tot 0.45) bestudeerd met confocale scanning laser microscopie (CSLM) en particle tracking voor verschillende afmetingen van de eerder beschreven denkbeeldige doos. Om deze afmeting te variëren is een apparaat ontworpen dat gebruik maakt van twee quasi parallelle horizontale oppervlakken, waarvan er een aangestuurd wordt door een piezo element. Dit geeft een zeer nauwkeurige controle over de afstand tussen de beide oppervlakken en een geringe drift. In termen van de eerder genoemde denkbeeldige doos, zijn de onderste en bovenste oppervlakken afgesloten terwijl de andere vier open blijven. Het bovenste oppervlak is ruw en het onderste oppervlak is glad op de lengteschaal van de deeltjes. Als de hoogte van de doos quasistatisch wordt teruggebracht van 18 tot 1 deeltje diameter, blijft de volume fractie in wezen constant maar vertragen de bewegingen van de deeltjes drastisch. Ook wordt een asymmetrie waargenomen in de dynamiek en de structuur van de suspensie, geme-

ten bij de twee oppervlakken. Dit verschil wordt toegeschreven aan een gecombineerd effect van de wandruwheid en de zwaartekracht.

Afgezien van de afmetingen is ook de vorm van de begrenzende doos van invloed op de deeltjes dynamica. In hoofdstuk 4 richten we ons op de dynamica van verdunde suspensies ($\phi << 0.1$) opgesloten in een cilindrische geometrie. De diffusie van colloïdale deeltjes van ongeveer een micron in diameter wordt bestudeerd in een cilinder van een vergelijkbare omvang (radius en hoogte bedragen 9 deeltjesdiameters). Een microfluïdische chip welke is opgebouwd uit verschillende laagjes wordt gebruikt voor het invangen en opsluiten van de deeltjes. Lokale diffusiecoëfficiënten worden gemeten met CSLM door veranderingen in deeltjesposities op te meten uit de video-opnames. De experimentele diffusiecoëfficiënten worden vergeleken met resultaten van numerieke simulaties waarin de locale visceuze weerstandskracht op een deeltje, en daarmee ook de diffusieconstante, wordt berekend door het oplossen van de Navier-Stokes vergelijking. De experimenten en simulaties toonden zeer goede overeenkomst. De diffusiecoëfficiënt in de cilinder blijkt dichtbij de wand richtings-afhankelijk te zijn, en kleiner dan de waarde in bulk vloeistof. Alle aspecten van de cilinder geometrie dienen in rekening te worden gebracht om een kwantitatieve voorspelling te kunnen doen. Dit is van belang voor het begrijpen van diffusie en (bio)fysische transport verschijnselen in begrensde omgevingen zoals cellen of bloedvaten.

Gemotiveerd door de resultaten van hoofdstuk 3, hebben we ons andermaal gericht op het effect van wand-ruwheid op de lokale dynamica en structuur van de suspensies in hoofdstuk 5. In deze studie wordt diffusie als functie van de volume fractie in de nabijheid van een wand met goed gedefinieerde ruwheid beschouwd. De ruwheid wordt gecontroleerd door het gedeeltelijk bedekken van een vlakke wand met iets kleinere colloïdale deeltjes dan die in de suspensie. De lokale volumefractie ($\phi \approx 0 - 0.4$) wordt gevarieerd via langzame sedimentatie. Als de volumefractie van gesuspendeerde deeltjes toeneemt bij de wand, wordt de deeltjes dynamica trager, terwijl daarnaast ook de signatuur van de beweging verandert: van diffusieve beweging tot 'rammelen in een kooi'.

Met betrekking tot externe velden, richten we ons op de zwaartekracht en ruimtelijke begrenzing in hoofdstuk 3 en 5 en op afschuif stromin-

gen geïnduceerd door Electrowetting in hoofdstuk 6. Daar waar de zwaartekracht een homogeen en tijdsinvariant veld is, variëren afschuifstromen zowel ruimtelijk als in de tijd. Beide variaties van afschuifstromingen kunnen worden benut bij de manipulatie van colloïdale assemblages. In hoofdstuk 6 bestuderen we het verdampen van druppels van colloïdale suspensies op een vaste ondergrond. Het verdampen van druppels van colloïdale suspensies en oplossingen van niet-vluchtige stoffen leidt vaak tot opdroogringen. Deze zogenaamde "koffievlekken" worden geïnduceerd door contactlijn pinning en oppervlaktespanning gedreven stromingen. De uiteindelijk resulterende niet-homogene verdeling van de opgeloste stoffen is in veel toepassingen, bijvoorbeeld in coating en printing technologieën. Combinatorische analyse methoden, zoals als fluorescente microarrays en MALDI-MS, de werkpaarden van de biomoleculaire analyse zijn concrete voorbeelden hiervan.

In een verdampende druppel worden colloïdale deeltjes naar de rand getransporteerd door capillaire stromingen, alwaar ze vastlopen als gevolg van geometrische opsluiting en het bereiken van een hoge volumefracties langs de contactlijn. In dit hoofdstuk wordt een methode ontwikkeld om de ongewenste koffievlekken te elimineren. De methode maakt gebruik van oscillatie van de contactlijn en afschuifstromingen geïnduceerd door electrowetting, om het koffievlek effect te elimineren. De afschuif-stromingen maken de deeltjes weer los in de nabijheid van de contactlijn, terwijl de beweging van de contactlijn het optreden van pinning voorkomt. Dit effect wordt geïllustreerd voor verschillende vloeistoffen, met inbegrip van suspensies van colloïdale deeltjes van verschillende groottes en materialen en DNA oplossingen. In combinatie met een goed ontwerp van microelektrodes, biedt deze methode biedt een effectieve remedie. Wij geloven dat onze methode van groot belang kan zijn voor het verbeteren van de efficiëntie van combinatoriële analysemethoden.

In grote lijnen kan het bevochtigingsgedrag van een 'Soft Matter systeem worden beschouwd als een randvoorwaarde. De manipulatie van bevochtigbaarheid is in wezen het veranderen van de contacthoek randvoorwaarde in de vergelijkingen die de morfologie van het systeem bepalen: een vloeistof druppel op een oppervlak zal juist die morfologie aannemen welke de effectieve grensvlak energie min-

imaliseert binnen de gegeven randvoorwaarden. Langs deze lijnen voorziet Electrowetting in een cruciaal instrument om Soft Matter te manipuleren. In hoofdstuk 7 & 8, onderzochten we het klassieke probleem van de bevochtiging een druppel op een vezel en later de bevochtiging van een druppel op een bol.

Voor de 'druppel op een vezel' geometrie besproken in hoofdstuk 7, bevestigen wij dat het voorkomen van twee concurrerende morfologieën wordt bepaald door de contacthoek en het relatieve volume van de druppel (genormeerd met de vezeldiameter). Bij kleine contacthoeken en relatief grote volumes overspoelt de druppel de vezel, in de zogenaamde "vat morfologie", terwijl voor grote contacthoeken en kleine relatieve volumes, de zogenaamde "clam-shell" morfologie ontstaat, met de druppel aan de zijkant van de fiber. Door het scannen van het morfologisch fasediagram opgespannen door de contact hoek en het relatieve druppelvolume, ontdekken we een eerder onontgonnen bistabiliteit regime en onthullen we de volledige aard van de overgang tussen twee concurrerende morfo-logiën. Bovendien wijzen de ideeën gegenereerd door deze studie, op een mogelijke toepassing van 'zelf verjongende vezels' met electrowetting functionaliteit, voor het scheiden van olie en water. Voor de 'druppel op een bol' geometrie beschreven in hoofdstuk 8 bestuderen we eveneens evenwichts morfologieën als functie van contact hoek en druppel volume. Wij bevestigen de voorspellingen van vrije energie berekeningen met onze experimentele resultaten en bepalen onder welke voorwaarden de druppel de bol zal verzwelgen. Wij geloven dat onze resultaten mogelijkheden kunnen bieden om via manipulatie van de bevochtigbaarheid, complexe colloïdale systemen te synthetiseren.

Acknowledgements

Perhaps the hardest part of any endeavor is the final touch, moments before end. In this case, I want to extend my gratitude to all that took part in the thesis so to say the cooking part.

I would like to start from Frieder Mugele. He supported my blue frenzy of crazy ideas and gave me freedom to transform them from back of the envelope calculations to measurable outcome. Without his encouragement these ideas would dissolve into thin air. The presence of Dirk van den Ende provided me an all around solid scientist to discuss just about anything. He simply taught me how to approach a problem calmly, analytically with a scientific constitution. Michel Duits was an excellent listener, always kind and considerate. He listened my blabla throughout my PhD and still kept his stance as a model colleague.

I would like to thank first of all the current and past members of Physics of Complex Fluids group for providing the perfect working environment. When I first arrived to Enschede; Helmut, Adrian, Sissi, Gor, Renske along with people from Physics of Fluids group (Bandito, Valeria, Marlies, Enrico, Gabriel, Yasmin, Benjamin, Mauro, Amy) make me feel welcomed. Sissi has always been a great roommate and a positive force of encouragement with her expressive comments. Helmut thought me the true force of will and how challenges can be addressed despite all sorts of disturbances. Daniel E. was always pleasant person to chat with.

As the waves of time eroded and reshaped the sand castles of space. Many more people entered the small stage I call my life. I would like to thank to all habitants of PCF for a pleasant working environment including but not limited to Hao, Adrian, Diendra, Omkar, Tarun, Dileep, Riëlle, Jolet, Dieter, Huub, Agata, Chandra, Jun, Daniel, E. and W., Cock, Mariska, Arun, Annelies, my summer interns: Ozgul, Tugce, Soykan. Special thanks goes to Florian Sterl for his help with

the animation programs. With some of my colleagues in PCF, I had the opportunity to work in the same projects. It was a pleasure to work with Jolet and Riëlle over the long weekends. We formed a harmonious, autonomous research team that produced high quality results. Without your hard, dedicated work the fiber story would not have emerged. I also enjoyed our game nights with Dieter, Huub, Jolet and Riëlle. With Dileep, we formed a hard working partnership. I will always remember the good Indian food and Polish cakes I openly stole from Dileep during lunch breaks. Working with Jun was a pleasure, I always enjoyed learning about his way of thinking not only in terms of science and but also life.

Special praise goes to Bandito a.k.a Paolo Oresta who spoiled me with his true friendship and exquisite Italian food. With Bandito, we formed an everlasting friendship and grew up together away from home. When I met Bandito he was a "first time out of mama's house" Italian man. when he left Enschede he was a tango dancing Dr.Oresta. Also special thanks go to Gor who has been by far my best flat mate ever and a good friend with a pure gold hearth.

Klaas Smit I have never seen a person that can provide so high quality mechanical work with so little input on my side. What can I say he gets done what you need. Daniel, Mariska and Cock were always ready to give a hand to my crazy ideas. Daniel was especially a creative, calming influence towards to my blue frenzy of ideas since the time we worked together on multilayer chips. Mariska and Cock provided the electrical and optical required in building just about anything I built or broke including but not limited to AFM.

Outside the group, I enjoyed talking science to especially to Eric Weeks and Micheal Hermes. Their insights and help in understanding confinement is rather appreciated. I specially thank Eric for sharing his library of particle tracking codes with everyone on Internet. Collaborating with Ciro Semprebon and Martin Brinkmann taught me fundamentals of wetting. I will always cherish their enthusiasm and friendly approach. Towards the end of my PhD I started collaborating with Anil Agiral, Han Gardeniers and Rob Lammertink. Han and Rob were always helpful and understanding every time I barged to their office with a bucket of ideas.

Outside work, I did not have much time yet whatever time I had left

I invested in sports especially Basketball and dancing. UT basketball club Arriba gave me the opportunity to meet people while playing my favorite game. I had many good friends in Arriba yet one stands out above all is Martin Kosters with whom we had always something to talk about. In the international community in UT, I enjoyed relaxing yet active dinners with David, Julian, Daniella, Oscar, Gabriel, Yasmin, Amy, Daniel (Somalian Mexican), Daniel (Oviedo), Alvero, Jun, Chiliean ginea pig a.k.a Sebo, Chao, Janet, Bilge, Anil. Turkish student association (TUSAT) helped me in my adaptation with their everlasting support. Special thanks goes to ADHAAR members for accepting Annemirl and myself as one of their own.

From my days at UCSB, two of my professors stick out with their characters and approach to teaching Science: Jacob Israelachvili and Micheal Doherty. Jacob was my academic advisor and introduced me to physics of interfaces with his lectures. I will always remember how careful, rigorous and patient he was towards my relatively meaningless problems and questions. He simply defined my idea of a scientist and a mentor. Micheal Doherty taught me Thermodynamics and Non-Linearity, he was a real calming and inspiring influence with his huge smile. I will always cherish how he made abstract concepts understandable for everyone. During my stay at Bogazici University, I was inspired by the enthusiasm of Turkan Haliloglu. She was always upbeat and motivated about her research, I guess the enthusiasm is contagious.

My family supported my endless pursuit to explore and challenge myself. In other words, in my endless search to find a witness to my existence. Since I left home for college, I had my share of ups and downs. It was of utmost importance that I knew they were there for me when I needed them. Insan zaman gectikce anliyor ailenin onemini, biraz yillanmak gerekiyor kanimca kalin kafamdan iceri girmesi icin o kardesimin bana yazdigi ”abicim” diye baslayan mektuplarin, annemin ”bana baklari” , babamin ”bak ben bunu aldim sana uyarmilari”, anneannemin mendile sardigi harcliklari ve boynuma doladigi her durma uygun ac-uygula ogutleri, dedemin uzaktan melun ”yine gel emileri”, susurluk’ta amcamlarla gecirdigimiz zamanlari, babaannemin sevgi dolu tatar bakislari, Huseyin dedemin alper ile beni tum yaptigimiz yaramazliklara ragmen bizi sakinmasi, adini hatirla-

madigim ama boynuma cilginca sarilan akrabalarin sicakliklari. When it comes to family special praise also goes to Leus family, for accepting me to their circle and teaching me Dutch customs with utmost sincerity. At last but not least, I want to thank to my girlfriend Annemirl for tolerating me and my stubborn thick headed nature. Without your endless love and support, none of the work I have done will be meaningful.

Output

Publications

- "Influence of rough and smooth walls on dynamics of concentrated colloidal suspensions in confinement", **H.B.Eral**, D.van den Ende, F.Mugele, M.H.G.Duits *Phys.Rev.E*, Vol.16, No.4, 319-322, 2009.
- "Anisotropic and hindered diffusion of colloidal particles in a cylinder", **H.B.Eral**, J.M.Oh, D.van den Ende, F.Mugele, M.H.G.Duits *Langmuir*, 2010, 26 (22), pp 16722-16729.
- "Reversible morphological transitions of a drop on a fiber", **H.B.Eral***, R.Ruiter*, J.Ruiter*, J.M.Oh, C.Semprebon, M.Brinkmann, F.Mugele to appear in *Soft Matter, 2011, DOI:10.1039/C0SM01403F*.
- "Wetting of a drop on a sphere", **H.B.Eral**, G.Manukyan, J.M.Oh accepted to *Langmuir*.
- "Suppressing the coffee stain effect: how to control colloidal self-assembly in evaporating drops using electrowetting", **H.B.Eral***, D.Agustine-Mampallil*, M.H.G.Duits, F.Mugele submitted to *Soft Matter*.
- "Electron injection through a nonpolar liquid", A.Agiral*, **H.B.Eral***, D.van den Ende, H.Gardeniers submitted.
- "Influence of wall roughness on confined concentrated suspensions", **H.B.Eral**, F.Mugele, M.H.G.Duits, in preparation.
- "Oscillations in a sandwich drop" D.Mampallil*, **H.B.Eral***, D.van den Ende, F.Mugele in preparation.

* indicate equal contribution

Patent(s)

- "A method for treating a liquid drop ",H.B.Eral, D.A.Mampallil, F.Mugele, PTC patent application, pending 2010

  We developed an Electrowetting based nonintrusive method to suppress coffee stain effect. This technology has various applications in improving combinatorial analysis, production of colloidal crystals and directed self assembly.

Invited Talks

- "Confinement effects of Hard Sphere like colloidal suspensions", Liquids and Interphases,2008, Lunteren, NL.
- "Dynamics of concentrated colloidal suspensions in confinement", FOM days, 2009, Veldhoven, NL
- "Dynamics of concentrated colloidal suspensions in confinement", Soft Matter colloquium, 2009, Utrecht, NL
- "Confinement effects on colloidal suspension: Microfluidic Methods for confinement", STR6 colloquium, 2010, Mainz, Germany
- "Manipulation of Soft Matter using Microfluidics, Confinement and Electrowetting", Christ College, 2010, Oxford, UK
- "Electrowetting functionalized fibers: morphologies of a drop on a fiber", Rock on a chip BP annual meeting, 2010, Enschede, NL
- "Electrowetting functionalized filters for Oil-Water separation", Norit Membrane Technologies, 2010, Enschede, NL
- "Dynamic suppression of coffee stain effect", Burgersdag, 2011, TU Delft, NL

Conference abstracts, poster presentations

- "Confinement effects of Hard Sphere like colloidal suspensions", Liquids and Interphases, 2008, Lunteren, NL (poster award)

- ”Confinement effects of Hard Sphere like colloidal suspensions: Gravity and Roughness”, Burgersdag, 2008, Delft, NL (poster)
- ”Confinement in Hard sphere suspensions”, in Colloidal Dispersions in External Fields, CODEF II, Bonn ,Germany (poster, abstract)
- ”Confinement effects of Hard Sphere like colloidal suspensions”, Gordon Conference, 2009, Venture, CA, USA (poster, abstract)
- ”Microfluidic manipulation of Soft Matter”, Liquids and Interphases, 2009, Lunteren, NL (poster)
- ”Diffusion inside 3D microfluidic confinement”, Burgersdag, 2009, Lunteren, NL (poster)
- ”Multilayer microfludic chips for confinement studies of Soft Matter”, International Soft Matter Conference , 2010, Granada, Spain (poster)
- ”Destiny of a drop on a fiber”, International Soft Matter Conference, 2010, Granada, Spain (poster)
- ”Microfluidic manipulation of Soft Matter”, Cargese Summer school of Soft Matter, 2010, Corsica, France (poster)
- ”Morphological Transitions of a drop on a fiber”, Cargese Summer school of Soft Matter, 2010, Corsica, France (poster)
- ”Dynamic suppression of Coffee stain effect”, Fermat-Impact meeting, 2010, Sevilla, Spain (abstract)

Biography

H.Burak Eral was born in Pearl of Aegean, Izmir, Turkiye on a beautiful spring morning 7th of April, 1980. He was raised in a small coastal town, Ayvalik, sandwiched between the blue of the Aegean sea and green of the olive trees. He studied in ITK high school of Natural sciences where he first developed an interest towards Science. Later he attended Chemical Engineering department in Bogazici University, Istanbul where he worked with Prof.Dr.Turkan Haliloglu in his bachelor project on coarse grained Molecular Dynamics simulations. He received his Master degree in Chemical Engineering department in University of California Santa Barbara in 2005. At UCSB, he was introduced to physics of interfaces and hydrodynamics with lectures from J. Israelachvili, G. Leal, M. Doherty. After a year of working experience in industry, he started his Ph.D. studies in University of Twente, Physics of Complex Fluids group where he worked on manipulation soft matter via altering the boundary conditions, applying external fields by means of microfluidics, confinement and wetting phenomena. His work at University of Twente is presented in several international conferences, resulted in publications in various journals, evoked interest in industry and lead to a patent application.

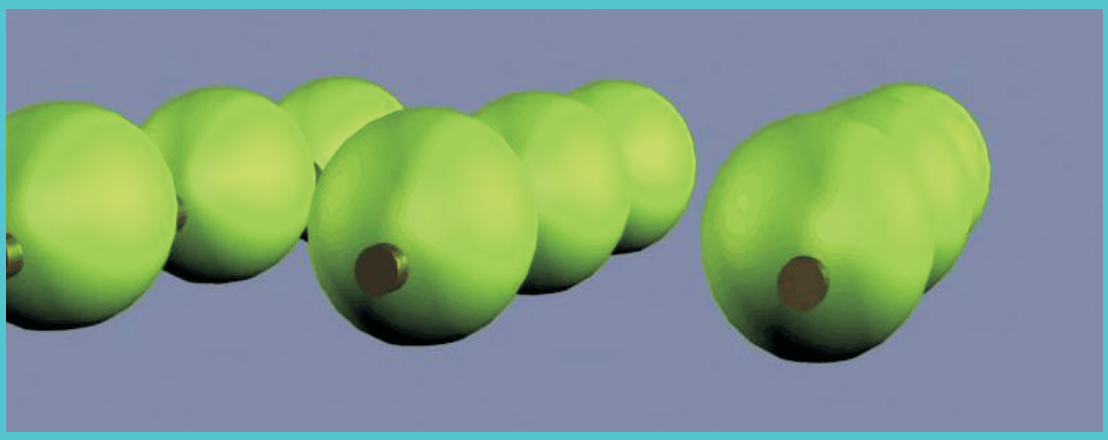

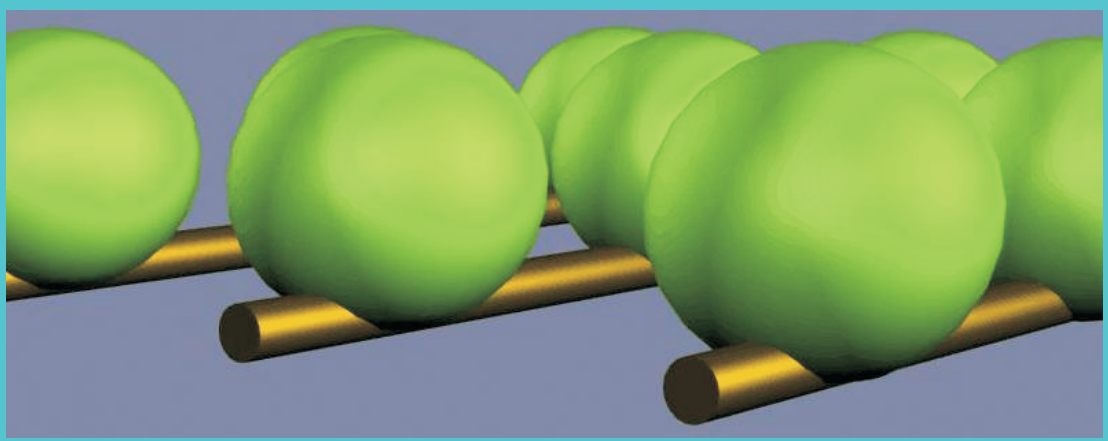

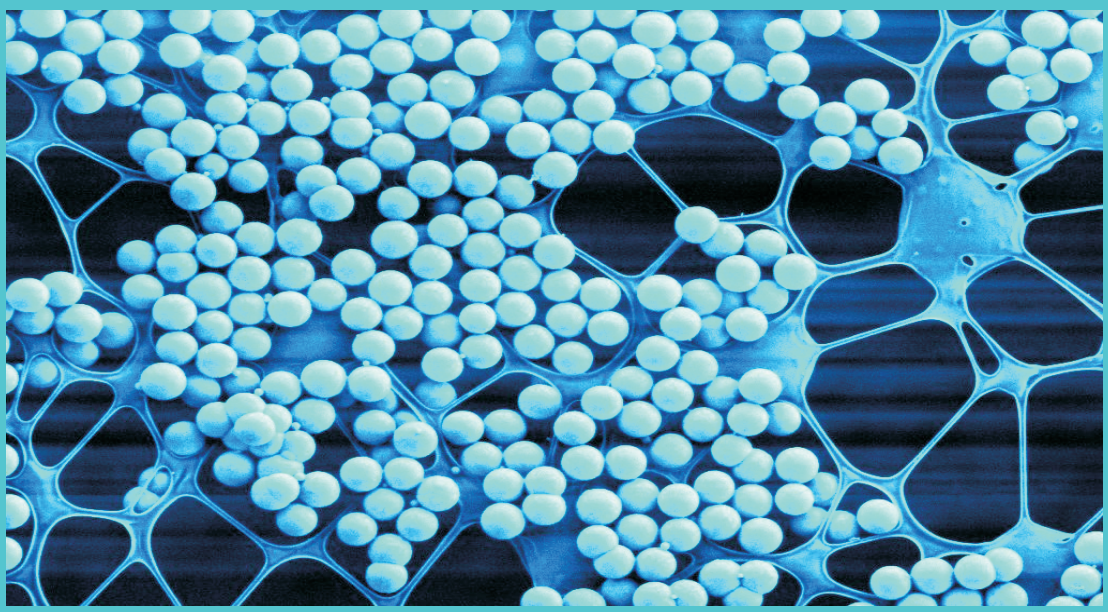

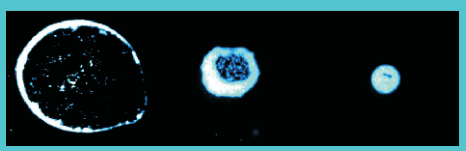

ISBN: 978-90-365-3167-2